UNIVERSITY OF CALIFORNIA
RIVERSIDE

Molecular Theories of Gas Adsorption in Nanoporous Materials

A Dissertation submitted in partial satisfaction
of the requirements for the degree of

Doctor of Philosophy

in

Chemical and Environmental Engineering

by

Yun Tian

June 2017

Dissertation Committee:
Dr. Jianzhong Wu, Chairperson
Dr. Bryan Wong
Dr. Deen Jiang

The Dissertation of Yun Tian is approved:

_____

_____

_____

Committee Chairperson

University of California, Riverside

Acknowledgements

It has been a long way, and I feel grateful to reach this point. First of all, I would like to thank my supervisor Prof. Jianzhong Wu for his continuous support and guidance of my Ph.D. study. His inspiration, motivation and immense knowledge helped me go through the whole journey. I could not have imagined having a better mentor for my Ph.D. study.

Besides my supervisor, I would like to express my sincere gratitude to the members of my PhD committee, Prof. Bryan Wong and Prof. Deen Jiang, for their help in my qualifying exam and final defense. My special thanks go to Dr. Jia Fu, Prof. Yu Liu and Dr. Jehoon Kim for their great support during my Ph.D. study. I also thank all my fellow lab mates for stimulating discussions and my friends in UCR for their warmly supporting in my life.

Last but not the least, I appreciate the life-time support from my family: my parents and my brother for their encouragements in these years.

This dissertation contains certain materials that have already been published in the AIChE Journal (Volume 61, Issue 9, Page 3012-3021), Langmuir (Volume 33, Issue 4, Page 996-1003, 2017). This Ph.D. work was financially sponsored by the National Science Foundation (NSF-CBET-1404046). Most computation was based on supercomputer allocations from the National Energy Research Scientific Computing Center (NERSC).

ABSTRACT OF THE DISSERTATION

Molecular Theories of Gas Adsorption in Nanoporous Materials

by

Yun Tian

Doctor of Philosophy, Graduate Program in Chemical and Environmental Engineering
University of California, Riverside, June 2017
Dr. Jianzhong Wu, Chairperson

With ever-increasing computer power and rapid developments in molecular theories, high-throughput computation will be instrumental to future materials design and discovery. This Ph.D. thesis explores the potential applications of the classical density functional theory (DFT) for fast screening of nanostructured porous materials for gas storage and separation. In addition to developing the computational methods, major efforts have been devoted to clarifying two fundamental yet long debated issues in the adsorption field, i.e., accurate prediction of the heat effect from adsorption isotherm and the connection between the BET and geometric surface areas of porous materials.

First we have investigated methane adsorption in a large library of metal-organic frameworks (MOFs) using four versions of classical DFT. The molecular thermodynamic model has been used to identify promising MOF materials and possible variations of operation parameters to meet the ARPA-E target set by the U.S. Department of Energy for natural gas storage.

The BET surface area is highly sensitive to the selected pressure region to perform the liner fitting and also the definition of the probe molecule used to determine the surface area. In this thesis, we provide a comprehensive analysis of the BET method. Based on extensive simulation data for over 1000 materials with complex structures and heterogeneous interactions, we find that the surface area obtained by standard BET method is not necessarily correlated with its geometrical accessible surface area.

Another aspect of this thesis is concerned with heat of adsorption, which is of both fundamental and practical importance. Here we present a rigorous theoretical procedure to predict isosteric heat. Quantitative relations between the differential heat and various isosteres have been established with the grand canonical Monte Carlo (GCMC) simulation for gas adsorption in amorphous and crystalline porous materials. The inconsistencies with conventional methods for the analysis of heat effect have been clarified in the context of the exact results for model systems.

By developing new computational methods for rapid prediction of gas adsorption and diffusivity and by resolving a number of controversial issues related to materials characterization and heat analysis, we hope that the theoretical work will have broad impacts on both materials design and industrial applications of gas adsorption and separation processes.

Table of Contents

List of Figures

List of Tables

Chapter 1. Introduction

1.1 Gas Storage and Separation in MOFs

Metal-organic frameworks (MOFs) are a new class of highly porous crystalline materials comprising metal ions or metal containing clusters (generally termed as secondary building blocks or SBUs) linked by organic ligands. The hybrid materials can be synthesized with tunable pore dimensions, surface areas, and framework topologies[1].

The open porous structures of MOFs result in very high void fraction and surface areas. Because of their enormous variety in chemical composition, tunable pore dimensions, accessibility and low densities, MOFs have been proposed as promising candidates for gas adsorption and separations. Although early research was mainly focused on the identification of novel MOFs for H_2 storage [2-5], recent years have seen growing attention to their applications to adsorption of other gases including methane and carbon dioxide[6,7]. These gas molecules interact much stronger with the surface of MOFs than hydrogen. It has been reported that methane storage in MOFs exceeds that in the best activated carbons[8]. More importantly, MOFs have predicable crystalline structures based on modular building blocks. Like activated carbons, MOFs can be synthesized in large scale for specific industrial applications.

A number of MOFs materials have been proposed for CH_4 gas storage. These include a few "top performers" such as NU-111[9], NU-125[10], UTSA-20[11], PCN-14[12], NiMOF-74[13], HKUST-1[14]. Because of the difficulties in material characterization and the low efficiency of experimental measurement of the gas adsorption amount, inconsistencies often exist in reporting adsorption results [8]. Besides, experimental exploration is limited to

a relatively small number of realistic MOFs that can be synthesized. The *in silico* search for optimal MOFs can benefit greatly from computational approach to generate a huge number of hypothetical MOF structures using a virtual library of building blocks. For example, Snurr's group used grand canonical Monte Carlo (GCMC) simulation to screen 100,000 hypothetical MOFs[15]. Despite their widespread usage, molecular simulations such as the GCMC method are rather computationally expensive and time-consuming for large-scale calculations. From a practical perspective, we need computationally more efficient methods with comparably accuracy to simulations to handle the screening of a huge library of possible MOFs[15].

MOFs are also potentially useful for gas separations. Membranes are broadly used in gas separations because of their low cost, high-energy efficiency, ease of process, excellent reliability, and usually smaller footprints compared with alternative technologies[16,17]. Important examples include CO_2 capture from flue gas (CO_2/N_2) or pre-combustion removal of CO_2 ($CH_4/H_2/CO_2$), and H_2 recovery from fuel gas or natural gas streams (H_2/CH_4). The pore size distribution plays a key role in the performance of nanoporous membranes for gas separation. Because MOFs have well-defined pore sizes and shapes, they show greater potential as advanced membrane materials in comparison with zeolites, which have relatively limited structure types.

Two parameters are particularly important for the evaluation of the performance of a membrane for gas separation: permeance (or flux) and selectivity[18]. The former estimates the transport rate of a given species through the membrane; it is often obtained by experimental measurement. And the later evaluates the ability of the membrane to separate

different components of a gas mixture, which could be predicted semi-quantitatively by modeling and computational methods. At this moment, a major direction of MOF research has been driven toward identification and development of membranes with higher selectivity and permeability. Despite impressive progresses in recent years, it remains difficult to design and characterize new MOF membranes for targeted applications.

Due to the huge number of existing structures of MOFs and the underlying potential for their versatile applications in gas storage and separation, it is urgent to develop efficient computation methods to predict and compare the adsorptive and diffusive properties of MOFs. The theoretical tool will help identify the best performing materials and their structure-properties relationships to guide rational design and synthesis of novel MOFs.

1.2 Theoretical Background

The classical density functional theory (DFT) has been widely used as a versatile tool for theoretical interpretation of adsorption behaviors[19,20], pore characterization and optimizations[21] in simple one-dimensional geometries like slit pores or cylindrical pores for several decades. With its high efficiency in predicting inhomogeneous fluid structures in confined geometry, we have successfully applied DFT to realistic three-dimensional MOF systems for CH_4 adsorption. In particular, the theoretical predictions have been benchmarked with 6 experimentally synthesized structures that had been claimed as the most promising materials for CH_4 storage[22]. We have also screened a large hypothetical MOF database after calibrated with simple slit-pore geometry.

Although the adsorption in MOFs has been intensively studied by both experiments and simulations, little is known about molecular diffusion in these materials, even though

it is closely related to gas permeability and selectivity for gas separation. Most of what is known about molecular diffusion in MOFs is from atomistic MD simulations [23-25], with only very limited MOFs tested experimentally. However, the considerable computational resources and time required by MD simulations have limited their usage in large-scale screening. Besides, diffusion rates on the order of $10^{-12} m^2 / s$ or smaller cannot be captured by conventional MD methods because of the large-time scales. From the implementation of DFT calculations, we have applied Rosenfeld's excess entropy scaling rule[26,27] to predict the self-diffusivity of CH_4 in MOF materials and analyzed their kinetic features.

Despite of its artificial nature, Brunauer-Emmett-Teller (BET) method is still being extensively used to characterize and compare the surface area of different porous materials both experimentally and computationally. Unlike the non-ordered porous materials, due to its crystalline structure, the geometrical area of MOFs can be independently calculated by rolling the specific probe (mostly N_2) over the atoms of the crystal structure of interest[28-30], which is usually named as nitrogen accessible surface area (NASA). It provides a unique opportunity in contrast to the non-ordered porous material to determine all the ideal textural parameters from crystal structure and compare with standard BET surface area.

Heat of adsorption is one of the most fundamental thermodynamic quantities to describe surface phenomena [31]. It is directly related to adsorbate-adsorbent interactions that are essential for assessment and screening of porous materials useful for gas storage and separation [32-34] and for thermal managements of industrial processes including various forms of pressure swing adsorption [35,36]. Despite a long history of theoretical studies and a vast experimental literature, controversies often arise in the thermodynamic analysis of

heat effects due to various assumptions used to describe gas adsorption and inconsistencies between direct calorimetric measurements and isosteric heat obtained from various adsorption isotherms. A rigorous thermodynamic framework is highly demanded to relate the differential heat of adsorption with the isostere consistently regardless of the operating conditions.

1.3 Molecular Model and Theory

1.3.1 Slit Pore Model

In molecular models of adsorption in porous carbon materials, the pores are usually assumed to be a wide range of slits with graphite walls. The wall-fluid interactions are described by the Steele's 10-4-3 potential[37]

$$V_{sf}(z) = \varepsilon_w \left[\frac{2}{5}\left(\frac{\sigma_w}{z}\right)^{10} - \left(\frac{\sigma_w}{z}\right)^{4} - \frac{\sigma_w^4}{3\Delta(0.61\Delta + z)^3} \right] \tag{1}$$

where ρ_s is the graphite carbon number density and Δ is the graphite interlayer spacing. σ_{sf} and ε_{sf} are size and energy parameters of the wall-fluid Lennard-Jones potential which are obtained from the Lorentz-Berthelot rules:

$$\sigma_{sf} = 0.5(\sigma_{ss} + \sigma_{ff}) \tag{2}$$

$$\varepsilon_{sf} = \sqrt{\varepsilon_{ss}\varepsilon_{ff}} \tag{3}$$

1.3.2 3D MOF materials

Rigid molecular model is used for the nanoporous materials, and the LJ parameters for all the MOFs are from universal force field (UFF)[38], and these crystalline structures stored in crystal information file (CIF) are used for all the theoretical

calculation[7,10,11,13,39,40]. Flexibility of the MOF materials are not considered here in both GCMC/MD simulations and DFT calculations. Charge effect is not considered in both DFT and GCMC/MD calculations, i.e., we consider only LJ interactions between framework atoms of MOFs and gas molecules.

1.3.3 GCMC simulation

To compare our DFT results for predicting adsorption isotherms, GCMC simulations for both slit-pore and MOFs are performed. We used 2x2x2 unit cells of adsorbents under 3D periodic boundary conditions. A cutoff of 12.9Å is used for the van der waals (VDW) interactions with shifted potential style. Three kinds of trial moves are used in GCMC sampling, viz., particle insertion, deletion and displacement in the box. After 10^6 moves for equilibrium, another 10^6 moves are performed as production run for data collection. The bulk chemical potential as the input parameter of each simulation is calculated from MBWR equation of state[41] under given temperature and bulk density. The data of each simulation trajectory is divided into 10 blocks to estimate the numerical uncertainties. MC simulations are performed with Towhee 7.0.4 package[42].

1.3.4 Molecular Dynamic simulation

We also did MD simulation to calculate the self-diffusion coefficients of CH_4/H_2 in the 6 MOFs mentioned above. The NVT ensemble was used with Nose-Hoover thermostat for temperature control, and after 1 ns of equilibration, 4 ns production run to collect information to calculate self-diffusivity from Einstein equation:

$$D_S = \lim_{t\to\infty} \frac{1}{6t} \left\langle | r(t) - r(0) |^2 \right\rangle \tag{4}$$

The time step is 1 fs, and the diffusion coefficients are all averaged after 5 times of independent simulations. We used LAMMPS package for all the MD simulations[43].

1.3.5 DFT calculations

In our molecular model, gas molecules can be depicted as spherical particles. Inside the MOF materials, each gas molecule is subject to an external field $V^{ext}(\mathbf{r})$, arising from its interaction with all the fixed framework atoms

$$V^{\text{ext}}(\mathbf{r}) = \sum_{i \in \text{MOF}} u_{\text{if}}(\mathbf{r} - \mathbf{r}_i) \tag{5}$$

where i represents the ith atom of the framework, which located at position $\mathbf{r}_i$, and $u(\mathbf{r} - \mathbf{r}_i)$ represents its interaction potential with the gas molecule at position $\mathbf{r}$. The Lennard-Jones (LJ) model is used to describe both interaction potentials between MOF-gas and gas-gas:

$$u_{ij}(r) = 4\varepsilon_{ij}\left[\left(\frac{\sigma_{ij}}{r}\right)^{12} - \left(\frac{\sigma_{ij}}{r}\right)^{6}\right] \tag{6}$$

where parameter σ_{ij} and ε_{ij} are obtained from standard semi-empirical force field and Lorentz-Berthelot (LB) mixing rule is employed for different atomic types.

The DFT calculations are based on the minimization of the grand potential functional:

$$\Omega\left[\rho(\mathbf{r})\right] = F\left[\rho(\mathbf{r})\right] + \int\left[V^{ext}(\mathbf{r}) - \mu\right]\rho(\mathbf{r})d\mathbf{r} \tag{7}$$

where μ is the bulk gas chemical potential, $F\left[\rho(\mathbf{r})\right]$ is the Helmholtz energy functional, and $\rho(\mathbf{r})$ is the density profile of gas molecules. The chemical can be obtained by the equation of state for the corresponding bulk fluid

$$\mu = \mu_{bulk}\left(P,T\right) \tag{8}$$

P and T represent pressure and temperature, respectively. For all DFT calculations in this work, the bulk chemical potentials are calculated from MBWR equation of state[41].

The Helmholtz energy functional includes an ideal-gas contribution F^{id} and excess contribution $F^{\mathrm{ex:}}$

$$F[\rho(\mathbf{r})] = F^{\mathrm{id}}[\rho(\mathbf{r})] + F^{\mathrm{ex}}[\rho(\mathbf{r})] \tag{9}$$

The ideal-gas contribution is exactly known:

$$F^{\mathrm{id}}[\rho(\mathbf{r})] = k_B T \int \rho(\mathbf{r})\{\ln \rho(\mathbf{r})\Lambda^3 - 1\}\mathrm{d}\mathbf{r} \tag{10}$$

k_B is the Boltzmann constant, and Λ is the thermal wavelength of gas molecules. As in virtually all DFT calculations, no exact expressions are available for the excess Helmholtz energy functional. Nevertheless, many approximations have been developed that are sufficiently accurate for practical applications. For simple fluids, F^{ex} is usually formulated in terms of a hard-sphere contribution, F^{hs} , to account for molecular excluded volume effects, and a perturbation arising from intermolecular attractions, F^{attr} [44-46]

$$F^{\mathrm{ex}}[\rho(\mathbf{r})] = F^{\mathrm{hs}}[\rho(\mathbf{r})] + F^{\mathrm{attr}}[\rho(\mathbf{r})] \tag{11}$$

In writing the above equation, we divide the LJ potential according to Barker-Henderson (BH) theory of bulk fluids[47]

$$u^{\mathrm{LJ}}(r) = u^{\mathrm{hs}}(r) + u^{\mathrm{attr}}(r) \tag{12}$$

$$u^{\mathrm{hs}}(r) = \begin{cases} \infty & r < d \\ 0 & r > d \end{cases} \tag{13}$$

$$u^{\mathrm{attr}}(r) = \begin{cases} 0 & r < \sigma \\ 4\varepsilon\left[\left(\frac{\sigma}{r}\right)^{12} - \left(\frac{\sigma}{r}\right)^{6}\right] & r > \sigma \end{cases} \tag{14}$$

where d is the hard-sphere diameter [48]:

$$d = \sigma\left(\frac{1 + 0.2977T^*}{1 + 0.33163T^* + 0.0010477T^{*2}}\right) \tag{15}$$

where $T^* = k_B T / \varepsilon$ is the reduced temperature.

The four representative versions of DFT applied in the calculations give different formulism in attractive part of excess Helmholtz free energy F^{attr} including two versions of weighted density approximations (WDA)[49], quadratic functional expansion and mean field approximation, while they all use modified fundamental measure theory (MFMT)[50] for the hard sphere repulsive interactions.

$$F^{\mathrm{hs}} = k_B T \int \Phi^{\mathrm{hs}}[n_\alpha(\mathbf{r})]\mathrm{d}\mathbf{r} \tag{16}$$

$\Phi^{hs}(\mathbf{r})$ is the excess free energy density contributed by the excluded volume effect.

$$\Phi^{\mathrm{hs}} = -n_0 \ln(1-n_3) + \frac{n_1 n_2 - \mathbf{n}_{\mathrm{V1}} \cdot \mathbf{n}_{\mathrm{V2}}}{1-n_3} + \frac{n_3 + (1-n_3)^2 \ln(1-n_3)}{36\pi n_3^2 (1-n_3)^2}(n_2^3 - 3n_2 \mathbf{n}_{\mathrm{V2}} \cdot \mathbf{n}_{\mathrm{V2}}) \tag{17}$$

$$n_\alpha(\mathbf{r}) = \int \rho(\mathbf{r}') w^{(\alpha)}(|\mathbf{r} - \mathbf{r}'|)\mathrm{d}\mathbf{r}' \quad \alpha \in \{0, 1, 2, 3, \mathrm{V1}, \mathrm{V2}\} \tag{18}$$

and $w^{(\alpha)}$ are the weighting functions related to the hard-sphere geometry[51]

$$\begin{cases} w^{(2)}(r) = \pi d^2 w^{(0)}(r) = 2\pi d w^{(1)}(r) = \delta(d/2 - r) \\ w^{(3)}(r) = \theta(d/2 - r) \\ \mathbf{w}^{(V2)}(\mathbf{r}) = 2\pi d \mathbf{w}^{(V1)}(\mathbf{r}) = w^{(2)}(r)\dfrac{\mathbf{r}}{r} \end{cases} \tag{19}$$

where $\delta(r)$ represents the Dirac delta function, and $\theta(r)$ is the Heaviside step function. In comparison with simulation results, MFMT is extremely accurate for describing the structural and thermodynamic properties of inhomogeneous hard-sphere systems[52].

For the attractive part of the Helmholtz energy functional, we consider the following four different approximations. These functionals have been commonly used in gas adsorption studies and are promising for large-scale DFT calculations.

I. Mean-Field Approximation (MFA)

The attractive component of the excess Helmholtz energy functional is given by

$$F^{MFA}[\rho(\mathbf{r})] = \frac{1}{2}\iint \rho(\mathbf{r})\rho(\mathbf{r}')u^{attr}(\mathbf{r}-\mathbf{r}')d\mathbf{r}d\mathbf{r}' \tag{20}$$

Like the van der Waals equation of state, MFA ignores correlated distribution of gas molecules inside the material. It has been used since the early application of DFT[53] and remains relevant in recent DFT calculations, in particular for materials characterization. With an accurate equation of state for bulk fluids, the mean-field approximation performs surprisingly well under many circumstances.

II. Weight-Density Approximations

In the version of DFT proposed by Yu[49], here designated as WDA-Yu, the attraction part of excess Helmholtz energy includes a mean-field contribution and an additional term due to correlation effects:

$$F^{\text{attr}}[\rho(\mathbf{r})] = F^{MFA}[\rho(\mathbf{r})] + F^{\text{cor}}[\rho(\mathbf{r})] \tag{21}$$

The mean-field contribution F^{MFA} is the same with equation, and F^{cor} is defined in terms of a local correlation free energy at an empirical weighted density:

$$F^{\text{cor}} = k_{\text{B}}T\int \Phi^{\text{cor}}[\bar{\rho}(\mathbf{r})]\text{d}\mathbf{r} \tag{22}$$

Φ^{cor} is the free energy per volume for the bulk system due to the correlation effect, and it can be obtained by

$$\Phi^{\text{cor}}(\rho) = \frac{F_{\text{bulk}}^{\text{LJ}}(\rho) - F_{\text{bulk}}^{\text{hs}}(\rho) - F_{\text{bulk}}^{\text{MFA}}(\rho)}{V} \tag{23}$$

where V is the volume, $F_{\text{bulk}}^{\text{LJ}}(\rho)$ is the excess free energy for the bulk LJ fluid at system temperature T and density ρ, $F_{\text{bulk}}^{\text{hs}}(\rho)$ is the excess free energy for bulk hard-sphere fluid, and $F_{\text{bulk}}^{\text{MFA}}(\rho)$ is the mean-field energy of the bulk system

$$\frac{F_{\text{bulk}}^{\text{MFA}}(\rho)}{V} = -\frac{16}{9}\pi\beta\varepsilon\rho^2\sigma^3 \tag{24}$$

$\frac{F_{\text{bulk}}^{\text{MFA}}(\rho)}{V} = -\frac{16}{9}\pi\beta\varepsilon\rho^2\sigma^3$ For $F_{\text{bulk}}^{\text{LJ}}(\rho)$ in this work, we used modified Benedict-Webb-Rubin (MBWR) equation of state, which is very accurate for a LJ fluid near the critical conditions, and $F_{\text{bulk}}^{\text{hs}}(\rho)$ is calculated from the Carnahan-Starling equation of state[54].

We also applied WDA to the correlation part of excess Helmholtz energy functional per molecule, different from WDA-Yu, which free energy per volume

$$F^{cor} = k_B T \int \rho(\mathbf{r}) f^{cor}[\bar{\rho}(\mathbf{r})] d\mathbf{r} \tag{25}$$

This version of DFT is designated as WDA-L, and later we will show that the two versions of WDA give virtually identical results.

III. Density Expansion method

In this method, we still separate the excess free energy into two parts, F_{hs} and F^{attr}. The functional expansion is applied only to the attractive part

$$\begin{aligned} \beta F_{attr}^{ex}[\rho(\mathbf{r})] = \beta F_{attr}^{ex}[\rho_b] - \int d\mathbf{r} C_{attr}^{(1)}(\rho(\mathbf{r}) - \rho_b) \\ - \frac{1}{2}\int\int d\mathbf{r} d\mathbf{r}' C_{attr}^{(2)}(|\mathbf{r} - \mathbf{r}'|)(\rho(\mathbf{r}) - \rho_b)(\rho(\mathbf{r}') - \rho_b) \end{aligned} \tag{26}$$

where the direct correlation functions (DCF) for the bulk systems are defined as

$$C_{attr}^{(1)} = -\delta\beta F_{attr}^{ex} / \delta\rho(\mathbf{r})|_b \tag{27}$$

$$C_{attr}^{(2)}(|\mathbf{r} - \mathbf{r}'|) = -\delta^2 \beta F_{attr}^{ex} / \delta\rho(\mathbf{r})\delta\rho(\mathbf{r}')|_b \tag{28}$$

It has been proved that the LJ potential can be accurately reproduced by a two-Yukawa function[55], which leads to an analytical expression for $C_{attr}^{(1)}$ and $C_{attr}^{(2)}(r)$ based on the first-order mean-spherical approximation (FMSA)[56]. For convenience, this version of DFT is referred as FMSA.

We minimize the grand potential functional with respect to the 3-dimensional density profiles of gas molecules by using the conjugate-gradient method (CG Descent)57.

From the equilibrium density profile $\rho(\mathbf{r})$, we calculate the adsorption amount based on the number of gas molecules in the MOF material and system volume:

$$\Gamma = \frac{k_B T_0}{P_0 V} \int \rho(\mathbf{r}) \mathrm{d}\mathbf{r} \tag{29}$$

where $P_0 = 1\,\mathrm{atm}$ and $T_0 = 25\,^{\circ}\mathrm{C}$ stand for the standard state (STP). As usual, the adsorption amount is expressed as the volume of gas adsorbed at the standard-state condition in unit volume of material.

Given the equilibrium density profile, we also calculated the excess entropy from thermodynamic relation:

$$S^{ex} = -\left(\frac{\delta F^{ex}}{\delta T} \right)_{\rho(\mathbf{r})} \tag{30}$$

Then we can calculate self-diffusivity, which is a combination of entropy scaling rule accounting for the gas-gas interaction with Knudsen model for the gas-surface interaction[27]:

$$\ln D_S = \left(1 - \frac{\lambda}{v_{free}} \right) \ln D_K + \frac{\lambda}{v_{free}} \ln D_E \tag{31}$$

where λ is the weighting factor to determine the contribution of gas-surface interaction and gas-gas interaction, v_{free} is the fraction of free volume that are accessible to gas molecules, D_K is the Knudsen diffusivity at infinite dilution limit, and D_E is the contribution from gas-gas interaction.

1.4 Dissertation organization

Chapter 2 focuses on utilizing classical density functional theory for high-throughput screening of nanoporous materials for natural gas storage. We used four versions of classical density functional theory (DFT) and calibrate the theoretical predictions with extensive simulation data for total gas uptake and delivery capacity.

Chapter 3 is concerned with the standard BET method to characterize surface area by comparison of more than 1000 MOFs with wide variety of structures and interactions with their geometrical accessible surface areas.

Chapter 4 clarifies the controversial issue in relating differential heat of adsorption with different isosteres and introduces a rigorous thermodynamic procedure for heat analysis which is free of inconsistency and convenient for practical applications.

Chapter 5 applies classical density functional theory to predicting differential heat of adsorption for both carbon slit pore and MOFs from the thermodynamic relations between grand potential and differential heat of adsorption.

Chapter 6 studies self-diffusivity of gas in porous material through classical transitional state theory combined with the string method to achieve much faster and more accurate prediction compared with conventional molecular dynamic simulations.

Chapter 7 summarizes main conclusions from this dissertation and plans for future work.

References:

1. Yang Q, Liu D, Zhong C, Li J-R. Development of Computational Methodologies for Metal–Organic Frameworks and Their Application in Gas Separations. *Chemical Reviews.* 2013/10/09 2013;113(10):8261-8323.

2. Dincă M, Long JR. Hydrogen Storage in Microporous Metal–Organic Frameworks with Exposed Metal Sites. *Angewandte Chemie International Edition.* 2008;47(36):6766-6779.

3. Furukawa H, Miller MA, Yaghi OM. Independent verification of the saturation hydrogen uptake in MOF-177 and establishment of a benchmark for hydrogen adsorption in metal-organic frameworks. *Journal of Materials Chemistry.* 2007;17(30):3197-3204.

4. Murray LJ, Dinca M, Long JR. Hydrogen storage in metal-organic frameworks. *Chemical Society Reviews.* 2009;38(5):1294-1314.

5. Suh MP, Park HJ, Prasad TK, Lim D-W. Hydrogen Storage in Metal–Organic Frameworks. *Chemical Reviews.* 2012/02/08 2011;112(2):782-835.

6. Kondo M, Yoshitomi T, Matsuzaka H, Kitagawa S, Seki K. Three-Dimensional Framework with Channeling Cavities for Small Molecules: {[M2(4, 4′-bpy)3(NO3)4]·xH2O}n (M Co, Ni, Zn). *Angewandte Chemie International Edition in English.* 1997;36(16):1725-1727.

7. Eddaoudi M, Kim J, Rosi N, et al. Systematic Design of Pore Size and Functionality in Isoreticular MOFs and Their Application in Methane Storage. *Science.* 2002;295(5554):469-472.

8. Mason JA, Veenstra M, Long JR. Evaluating metal-organic frameworks for natural gas storage. *Chemical Science.* 2014;5(1):32-51.

9. Peng Y, Srinivas G, Wilmer CE, et al. Simultaneously high gravimetric and volumetric methane uptake characteristics of the metal-organic framework NU-111. *Chemical Communications.* 2013;49(29):2992-2994.

10. Wilmer CE, Farha OK, Yildirim T, et al. Gram-scale, high-yield synthesis of a robust metal-organic framework for storing methane and other gases. *Energy & Environmental Science.* 2013;6(4):1158-1163.

11. Guo Z, Wu H, Srinivas G, et al. A Metal–Organic Framework with Optimized Open Metal Sites and Pore Spaces for High Methane Storage at Room Temperature. *Angewandte Chemie International Edition.* 2011;50(14):3178-3181.

12. Ma S, Sun D, Simmons JM, Collier CD, Yuan D, Zhou H-C. Metal-Organic Framework from an Anthracene Derivative Containing Nanoscopic Cages Exhibiting High Methane Uptake. *Journal of the American Chemical Society.* 2008/01/01 2007;130(3):1012-1016.

13. Wu H, Zhou W, Yildirim T. High-Capacity Methane Storage in Metal−Organic Frameworks M2(dhtp): The Important Role of Open Metal Sites. *Journal of the American Chemical Society.* 2009/04/08 2009;131(13):4995-5000.

14. Chui SS-Y, Lo SM-F, Charmant JPH, Orpen AG, Williams ID. A Chemically Functionalizable Nanoporous Material [Cu3(TMA)2(H2O)3]n. *Science.* February 19, 1999 1999;283(5405):1148-1150.

15. Wilmer CE, Leaf M, Lee CY, et al. Large-scale screening of hypothetical metal–organic frameworks. *Nat Chem.* 2012;4(2):83-89.

16. Merkel TC, Freeman BD, Spontak RJ, et al. Ultrapermeable, Reverse-Selective Nanocomposite Membranes. *Science.* April 19, 2002 2002;296(5567):519-522.

17. Kamakoti P, Morreale BD, Ciocco MV, et al. Prediction of Hydrogen Flux Through Sulfur-Tolerant Binary Alloy Membranes. *Science.* January 28, 2005 2005;307(5709):569-573.

18. Li J-R, Sculley J, Zhou H-C. Metal–Organic Frameworks for Separations. *Chemical Reviews.* 2012/02/08 2011;112(2):869-932.

19. Balbuena PB, Gubbins KE. Theoretical interpretation of adsorption behavior of simple fluids in slit pores. *Langmuir.* 1993/07/01 1993;9(7):1801-1814.

20. Lastoskie C, Gubbins KE, Quirke N. Pore size heterogeneity and the carbon slit pore: a density functional theory model. *Langmuir.* 1993/10/01 1993;9(10):2693-2702.

21. Cracknell RF, Gordon P, Gubbins KE. Influence of pore geometry on the design of microporous materials for methane storage. *The Journal of Physical Chemistry.* 1993/01/01 1993;97(2):494-499.

22. Peng Y, Krungleviciute V, Eryazici I, Hupp JT, Farha OK, Yildirim T. Methane Storage in Metal–Organic Frameworks: Current Records, Surprise Findings, and Challenges. *Journal of the American Chemical Society.* 2013/08/14 2013;135(32):11887-11894.

23. Skoulidas AI. Molecular Dynamics Simulations of Gas Diffusion in Metal−Organic Frameworks: Argon in CuBTC. *Journal of the American Chemical Society.* 2004/02/01 2004;126(5):1356-1357.

24. Skoulidas AI, Sholl DS. Self-Diffusion and Transport Diffusion of Light Gases in Metal-Organic Framework Materials Assessed Using Molecular Dynamics Simulations. *The Journal of Physical Chemistry B.* 2005/08/01 2005;109(33):15760-15768.

25. Keskin S, Liu J, Rankin RB, Johnson JK, Sholl DS. Progress, Opportunities, and Challenges for Applying Atomically Detailed Modeling to Molecular Adsorption and Transport in Metal−Organic Framework Materials. *Industrial & Engineering Chemistry Research.* 2009/03/04 2008;48(5):2355-2371.

26. Rosenfeld Y. Relation between the transport coefficients and the internal entropy of simple systems. *Physical Review A.* 1977;15(6):2545-2549.

27. Liu Y, Fu J, Wu J. Excess-Entropy Scaling for Gas Diffusivity in Nanoporous Materials. *Langmuir.* 2013/10/22 2013;29(42):12997-13002.

28. Düren T, Millange F, Férey G, Walton KS, Snurr RQ. Calculating Geometric Surface Areas as a Characterization Tool for Metal−Organic Frameworks. *The Journal of Physical Chemistry C.* 2007/10/01 2007;111(42):15350-15356.

29. Bae Y-S, Yazaydın AÖ, Snurr RQ. Evaluation of the BET Method for Determining Surface Areas of MOFs and Zeolites that Contain Ultra-Micropores. *Langmuir.* 2010/04/20 2010;26(8):5475-5483.

30. Frost H, Düren T, Snurr RQ. Effects of Surface Area, Free Volume, and Heat of Adsorption on Hydrogen Uptake in Metal−Organic Frameworks. *The Journal of Physical Chemistry B.* 2006/05/01 2006;110(19):9565-9570.

31. Myers AL. Thermodynamics of adsorption in porous materials. *AIChE Journal.* 2002;48(1):145-160.

32. Bhatia SK, Myers AL. Optimum Conditions for Adsorptive Storage. *Langmuir.* 2006/02/01 2006;22(4):1688-1700.

33. Lee S-J, Bae Y-S. Can Metal–Organic Frameworks Attain New DOE Targets for On-Board Methane Storage by Increasing Methane Heat of Adsorption? *The Journal of Physical Chemistry C.* 2014/08/28 2014;118(34):19833-19841.

34. Amrouche H, Creton B, Siperstein F, Nieto-Draghi C. Prediction of thermodynamic properties of adsorbed gases in zeolitic imidazolate frameworks. *RSC Advances.* 2012;2(14):6028-6035.

35. Sircar S. Basic Research Needs for Design of Adsorptive Gas Separation Processes. *Industrial & Engineering Chemistry Research.* 2006/08/01 2006;45(16):5435-5448.

36. Hartzog DG, Sircar S. Sensitivity of PSA process performance to input variables. *Adsorption.*1(2):133-151.

37. Steele WA. The physical interaction of gases with crystalline solids: I. Gas-solid energies and properties of isolated adsorbed atoms. *Surface Science.* 1973;36(1):317-352.

38. Rappe AK, Casewit CJ, Colwell KS, Goddard WA, Skiff WM. UFF, a full periodic table force field for molecular mechanics and molecular dynamics simulations. *Journal of the American Chemical Society.* 1992/12/01 1992;114(25):10024-10035.

39. Ma S, Sun D, Simmons JM, Collier CD, Yuan D, Zhou H-C. Metal-Organic Framework from an Anthracene Derivative Containing Nanoscopic Cages Exhibiting High Methane Uptake. *Journal of the American Chemical Society.* 2008/01/01 2008;130(3):1012-1016.

40. Chui SS-Y, Lo SM-F, Charmant JPH, Orpen AG, Williams ID. A Chemically Functionalizable Nanoporous Material [Cu₃(TMA)₂(H₂O)₃]_n. *Science.* 1999;283(5405):1148-1150.

41. Johnson JK, Zollweg JA, Gubbins KE. The Lennard-Jones equation of state revisited. *Molecular Physics.* 1993/02/20 1993;78(3):591-618.

42. Martin MG. 2013; http://towhee.sourceforge.net.

43. Plimpton S. Fast Parallel Algorithms for Short-Range Molecular Dynamics. *Journal of Computational Physics.* 1995;117(1):1-19.

44. Siderius DW, Gelb LD. Predicting Gas Adsorption in Complex Microporous and Mesoporous Materials Using a New Density Functional Theory of Finely Discretized Lattice Fluids. *Langmuir.* 2009/02/03 2009;25(3):1296-1299.

45. Li Z, Cao D, Wu J. Density-functional theory and Monte Carlo simulation for the surface structure and correlation functions of freely jointed Lennard-Jones polymeric fluids. *The Journal of Chemical Physics.* 2005;122(17):-.

46. Ye Z, Chen H, Cai J, Liu H, Hu Y. Density functional theory of homopolymer mixtures confined in a slit. *The Journal of Chemical Physics.* 2006;125(12):-.

47. Barker JA, Henderson D. Perturbation Theory and Equation of State for Fluids. II. A Successful Theory of Liquids. *The Journal of Chemical Physics.* 1967;47(11):4714-4721.

48. Cotterman RL, Schwarz BJ, Prausnitz JM. Molecular thermodynamics for fluids at low and high densities. Part I: Pure fluids containing small or large molecules. *AIChE Journal.* 1986;32(11):1787-1798.

49. Yu Y-X. A novel weighted density functional theory for adsorption, fluid-solid interfacial tension, and disjoining properties of simple liquid films on planar solid surfaces. *The Journal of Chemical Physics.* 2009;131(2):-.

50. Yu Y-X, Wu J. Structures of hard-sphere fluids from a modified fundamental-measure theory. *The Journal of Chemical Physics.* 2002;117(22):10156-10164.

51. Rosenfeld Y. Free-energy model for the inhomogeneous hard-sphere fluid mixture and density-functional theory of freezing. *Physical Review Letters.* 1989;63(9):980-983.

52. Roland R. Fundamental measure theory for hard-sphere mixtures: a review. *Journal of Physics: Condensed Matter.* 2010;22(6):063102.

53. Tarazona P, Evans R. A simple density functional theory for inhomogeneous liquids. *Molecular Physics.* 1984/07/01 1984;52(4):847-857.

54. Carnahan NF, Starling KE. Equation of State for Nonattracting Rigid Spheres. *The Journal of Chemical Physics.* 1969;51(2):635-636.

55. Tang Y, Tong Z, Lu BCY. Analytical equation of state based on the Ornstein-Zernike equation. *Fluid Phase Equilibria.* 1997;134(1–2):21-42.

56. Tang Y. On the first-order mean spherical approximation. *The Journal of Chemical Physics.* 2003;118(9):4140-4148.

57. Hager W, Zhang H. A New Conjugate Gradient Method with Guaranteed Descent and an Efficient Line Search. *SIAM Journal on Optimization.* 2005;16(1):170-192.

Chapter 2. Classical Density Functional Theory for Methane Adsorption in Metal-Organic Frameworks

Abstract

Natural gas is considered as a promising alternative to petroleum as the next generation of primary transportation fuel owing to relatively smaller carbon footprint and lower SO_x/NO_x emissions and to fast developments of shale gas in recent years. Since the volumetric energy density of methane amounts to only about 1% of that of gasoline at ambient conditions, natural gas storage represents one of the key challenges for prevalent deployment of natural gas vehicles (NGVs). In this work, we present a molecular thermodynamic model that is potentially useful for high-throughput screening of nanoporous materials for natural gas storage. We investigate methane adsorption in a large library of metal-organic frameworks (MOFs) using four versions of classical density functional theory (DFT) and calibrate the theoretical predictions with extensive simulation data for total gas uptake and delivery capacity. In combination with an extended excess entropy scaling method, the classical DFT is also used to predict the self-diffusion coefficients of the confined gas in several top-ranked MOFs. The molecular thermodynamic model has been used to identify promising MOF materials and possible variations of operation parameters to meet the ARPA-E target set by the U.S. Department of Energy for natural gas storage.

2.1. Introduction

Adsorption thermodynamics plays a pivotal role in traditional as well as modern chemical engineering ranging from separation processes and heterogeneous catalysis to various tools for chemical analyses such as chromatography[58,59]. From a practical point of view, one of the most useful thermodynamic models for gas adsorption was established by Myers and Prausnitz, published in the *AIChE Journal* about 50 years ago[60]. We are pleased to dedicate this article to the special issue honoring Professor John Prausnitz.

According to conventional wisdom, adsorption is a surface phenomenon related to adhesion of molecules, atoms or ions at an interface. Whereas in classical thermodynamics concepts such as surface area and binding energy are indispensable to describe the interfacial phenomena, Myers and Prausnitz took a radically different approach by extending the ideal solution model for vapor-liquid equilibria (VLE) to adsorption of gas mixtures. The "solution model" is remarkably accurate for predicting the adsorption isotherm of a gas mixture from those for pure components at moderate pressure, yet it is computationally convenient for practical applications. Because the number of pure species is limited in comparison to that for mixtures, the solution model has been invaluable for design and optimization of industrial adsorption processes and remains relevant today[61].

Driven by increasing concerns over global climate change and rapid developments in renewable energy, research in gas adsorption has experienced considerable growth in recent years. However, the main focus of current literature has been shifted from adsorption equilibria *per se* to discovery of novel nanoporous materials, in particular open-framework materials promising for large-scale hydrogen/methane storage or for selective adsorption

of carbon dioxide from gas mixtures[62]. Unlike conventional adsorbents such as activated carbon or silica gel, open-framework materials are porous crystalline solids viable for solution synthesis by coordinate bonding of secondary building units (SBUs), *i.e.*, libraries of organic linkers and organometallic/nonmetallic nodes self-organized into periodic and porous frameworks[63]. Theoretical investigations are useful to acquire a better knowledge of adsorbate-adsorbent interactions and, perhaps more important, for discovery and rational design of nanoporous materials tailored to specific adsorbates. The modular nature of the building blocks makes the framework structures predictable based on the topology and the geometry of specific link-node coordination complexes, rendering unprecedented opportunities for computational design/discovery of crystalline porous materials, and to have a precise control over their porosity and atomic compositions (size, shape, and functionality). Molecular modeling is useful to identify specific open-framework materials from a virtually infinite number of SBU combinations to meet specific practical needs[64-67].

Whereas there have been impressive theoretical developments toward the discovery of better adsorbents for gas storage and separation[68-71], computational materials design remains in early development; there are enormous challenges from practical perspectives. To predict material performance from the chemistry of its building blocks, we need efficient multiscale modeling methods that account for not only intrinsic properties in vacuum but also interactions with a working environment under diverse thermodynamic conditions. As illustrated schematically in Figure 1, computational materials design (or discovery) entails quantum mechanical (QM) calculations for determining electronic properties as well as molecular and crystal structures, and statistical mechanical (SM)

calculations for predicting the physicochemical properties of materials under different environments. Myriad computational methods are available for predicting electronic, molecular and thermodynamic properties[72]. Typically, these computational methods are established in the context of drastically different theoretical frameworks; approximations are inevitable at each level. As a result, multiscale modeling requires a judicious selection of QM and SM methods. An optimal choice resides not necessarily only in terms of the theoretical rigor at individual scales but, perhaps more important, a reliable connection between different methods and the overall computational efficiency to attain pragmatic goals.

Amid numerous computational tools in QM and SM, density functional theory (DFT) provides a unified mathematical framework to describe the properties of many-body systems using the one-body density profiles as the fundamental variables. Whereas the original concepts, as first introduced many years ago by Hohenberg and Kohn[73], were intended to provide an alternative to the Schrödinger equation for predicting ground-state electronic properties, the mathematical framework has been generalized, applicable to electronic systems at finite temperature and to statistical-mechanical systems including those containing classical particles and polymers[74]. While nowadays DFT is best known for its applications to electronic systems at 0 K, due to its extreme popularity in computational chemistry and materials science[75], the practicality of classical DFT for studying adsorption and other interfacial phenomena has been well established[76]. For example, classical DFT programs have been routinely used to analyze experimental data for the characterization of porous materials by gas adsorption[77]. Because DFT calculations

avoid explicit multi-body wave functions for quantum systems or microstates for thermodynamic systems containing classical particles, its computational efficiency is by far superior to wave-function-based QM methods and conventional molecular simulations in SM. The computational efficiency and flexibility in density functionals make DFT an ideal choice for multiscale modeling for both QM and SM calculations[78].

In a previous work[79], we demonstrated that the classical DFT could be used for rapid screening a large library of metal-organic frameworks (MOFs) potentially useful for H_2 storage. Using extensive Monte Carlo (MC) simulation data as the benchmark, we tested the theoretical performance of four versions of free-energy functionals that are commonly used in the literature to describe the thermodynamic properties of inhomogeneous fluids[80-83]. All these functionals incorporate the modified fundamental-measure theory (MFMT)[84] to account for molecular excluded-volume effects but they differ in representing the attraction part of the excess free energy. In stark contrast to previous calibrations with model systems containing Lennard-Jones (LJ) fluids in idealized pores, we find that the theoretical predictions are sensitive to specific gas components (*e.g.*, N_2 adsorption versus hydrogen storage) and thermodynamic conditions. In this work, we test the performance of different classical DFT methods for predicting methane adsorption in model slit pores as well as in a large library of hypothetical nanostructured materials. In addition to adsorption isotherms, we consider methane diffusivity in top-performance MOFs using an extended excess-entropy scaling scheme proposed in our earlier work[27]. After extensive calibration with our simulation results, the DFT methods have been applied to identify promising MOF materials for methane storage and possible variations of operation conditions to attain the

adsorption target set by the U. S. Department of Energy (DOE) for natural gas storage in vehicles.

2.2. Molecular Model and Theory

The theoretical models for predicting adsorption isotherms and diffusivity have been reported in our previous publications[27,79]. For completeness, here we recapitulate only the basic ideas of classical DFT and the computational procedures. In Supplementary Materials, we present the key equations from the four versions of the excess free energy functional used in this work and additional results from classical DFT predictions.

Molecular model

To describe gas adsorption in MOF materials, we need to define both bonded and non-bonded interactions among MOF atoms, and MOF-gas and gas-gas pair interactions in addition to temperature T and pressure P of the gas phase. As in our previous work, we assume that the MOF materials are sufficiently rigid so that their crystalline structures are unchanged by gas adsorption. The crystallographic information files (CIFs) of MOF materials are adopted from the hypothetical library constructed by Wilmer et al.[68]

As a general rule for selecting the size of the computation box, we use a 2×2×2 supercell of the crystalline structure for each material. The conventional periodic boundary conditions (PBC) are applied to all directions. For most MOFs considered in this work, the 2×2×2 supercell ensures that each dimension of the simulation box is larger than twice of the cut-off distance. For MOFs with very small unit cells, however, we increase the supercell size by adding more repeating unit cells of the crystalline structure such that each dimension is larger than twice of the cut-off distance. As usual, methane molecules are

represented by Lennard-Jones (LJ) particles, with parameters, ε_{CH4}/k_B=148.0 K and σ_{CH4}=3.73 Å, obtained from the TraPPE force field[85]. For each gas molecule inside the MOF material, the potential energy at position **r** is approximated by pairwise-additive interactions with all solid atoms

$$V^{\text{ext}}(\mathbf{r}) = \sum_{i \in \text{MOF}} u_{if}(\mathbf{r} - \mathbf{r}_i) \tag{32}$$

where subscript *i* represents the i^{th} atom from the MOF framework, and $\mathbf{r}_i$ stands for the position of atom *i*. The pair potential between atom *i* and gas molecule *f*, $u_{if}(\mathbf{r})$, is also represented by the LJ potential

$$u_{if}(r) = 4\varepsilon_{if}\left[\left(\frac{\sigma_{if}}{r}\right)^{12} - \left(\frac{\sigma_{if}}{r}\right)^{6}\right] \tag{33}$$

where parameters ε_{if} and σ_{if} are calculated from the Lorentz-Berthelot (LB) mixing rule. In both simulations and classical DFT calculations performed in this work, the LJ parameters for the MOF atoms are taken from the universal force field (UFF)[86].

Adsorption thermodynamics

Classical DFT allows us to predict the local number density of gas molecules within the adsorbent phase, *viz.*, inside each MOF material[87]

$$\rho(\mathbf{r}) = \rho_b \exp\left[-\beta V^{\text{ext}}(\mathbf{r}) - \beta\Delta\mu^{\text{ex}}(\mathbf{r})\right] \tag{34}$$

where ρ_b stands for the number density of gas molecules in the bulk, $\beta = 1/(k_B T)$, and k_B is the Boltzmann constant. The last term on the right side of Eq. (34) is defined by $\Delta\mu^{\text{ex}}(\mathbf{r}) = \mu^{\text{ex}}(\mathbf{r}) - \mu_b^{\text{ex}}$, that represents the deviation of local excess chemical potential

$\mu^{ex}(\mathbf{r})$ from that corresponding to the bulk phase, μ_b^{ex}. Thermodynamic properties of the gas phase, including ρ_b and μ_b^{ex} as functions of T and P, are calculated from the modified Benedict-Webb-Rubin (MBWR) equation of state[88]. In general, the local chemical potential depends on the local density profile $\rho(\mathbf{r})$; it must be determined self-consistently from Eq.(34) by iterations.

Intuitively, Eq.(34) may be understood as the Boltzmann distribution of gas molecules in the presence of an external field, $V^{ext}(\mathbf{r})$. Within the framework of classical DFT, this equation is formally exact. Approximations are introduced only in calculating the local excess chemical potential, that can be derived from the functional derivative of the excess Helmholtz energy, $F^{ex}(\mathbf{r})$,

$$\mu^{ex}(\mathbf{r}) = dF^{ex}(\mathbf{r}) / d\rho(\mathbf{r}). \tag{35}$$

Like the excess properties of a uniform thermodynamic system, $F^{ex}(\mathbf{r})$ accounts for the thermodynamic non-ideality due to intermolecular interactions. The excess Helmholtz energy is an intrinsic property independent on the external potential, *i.e.*, interaction of gas molecules with the adsorbent atoms. If the intermolecular interaction between gas molecules is negligible, the excess Helmholtz energy vanishes. In that case, Eq.(34) corresponds to the distribution of ideal-gas molecules inside the porous material.

Whereas accurate expressions have been developed for $F^{ex}(\mathbf{r})$ of inhomogeneous simple fluids below the vapor-liquid critical temperature[80,89], little is known about their performance at high temperature and pressure, *i.e.*, conditions relevant to gas adsorption in typical industrial processes. In this work, we consider four versions of classical DFT that

have been used for predicting hydrogen adsorption in various MOF materials. All these functionals are based on the modified fundamental measure theory (MFMT)[84] to describe molecular excluded volume effects but differ in the contribution to account for intermolecular attractions. The attractive part of the excess Helmholtz energy functional is distinguished in terms of the mean-field approximation (MFA)[81], the first-order mean-spherical approximation (FMSA)[80], and two slightly different forms of weighted density approximations (WDA-Y[82] and WDA-L[83]). The equations for these functionals and numerical details are discussed in Supplementary Materials.

Total gas adsorption is conventionally expressed as the volume of adsorbed gas molecules per unit volume of the porous material at the standard state (STP). Total adsorption G can be calculated from the molecular density profile by integration over the supercell

$$G = \frac{k_B T_0}{P_0 V} \int \rho(\mathbf{r}) \mathrm{d}\mathbf{r} \tag{36}$$

where $P_0 = 1\,\mathrm{atm}$, $T_0 = 25\,^{\circ}\mathrm{C}$, and V is the supercell volume. For applications to gas storage, we are mostly interested in the delivery amount, G_{del}, that corresponds to the change in total gas uptake by the material at compression and release conditions. Total gas adsorption or delivery amount should not be confused with the surface excess G^{ex} conventionally defined as

$$G^{ex} = \frac{k_B T_0}{P_0 V} \int [\rho(\mathbf{r}) - \rho_b] \mathrm{d}\mathbf{r} \tag{37}$$

In general, the local number density of gas molecules inside a nanostructured material is highly inhomogeneous due to extreme confinement and attraction from adsorbent atoms. The difference between absolute and excess adsorption is negligible only when the pressure of the bulk gas is very low.

Given an expression for the excess Helmholtz energy functional, we can derive the excess entropy of gas molecules inside the porous material from the thermodynamic relation

$$S^{\mathrm{ex}} = -\left(\frac{\partial F^{\mathrm{ex}}}{\partial T}\right)_{\beta m, V} \tag{38}$$

and the enthalpy of adsorption from

$$Q = -T\left(\frac{\partial \Delta W}{\partial T}\right)_{\beta m, V} \tag{39}$$

In Eq.(39), ΔW represents the difference between the grand potential of gas molecules in the porous material and that of the same amount of the bulk gas at the same temperature and chemical potential:

$$\Delta W = k_B T \int d\mathbf{r}\, r(\mathbf{r})\{\ln[r(\mathbf{r})/r_b] - 1 - \beta m_b^{ex} + Z + \beta V_{ext}(\mathbf{r})\} + F^{ex}[r(\mathbf{r})] \tag{40}$$

where $Z = Z(T, P)$ stands for the compressibility factor of the bulk gas. While enthalpy of adsorption is not explicitly studied in this work, we note that gas pressure inside a porous material corresponds to a second-order tensor where each element varies with the position. As a result, the adsorbed gas does not have an enthalpy as typically defined in classical thermodynamics for bulk fluids. Confusion might arise if one calculates the enthalpy of

adsorption based on enthalpy changes. In writing Eq. (39), we assume that the porous material is rigid such that gas adsorption has negligible effect on the solid's entropy.

Excess entropy scaling for calculating gas diffusivity

As in our previous work[27], we assume that self-diffusivity of gas molecules in a porous medium, here designated as D_s , may be determined from a linear combination of those predicted from the Knudsen diffusion model and the excess-entropy scaling method

$$\ln D_s = \left(1 - \frac{\alpha\sigma^3}{v_{free}}\right)\ln D_K + \frac{\alpha\sigma^3}{v_{free}}\ln D_E \tag{41}$$

where v_{free} represents the total accessible volume of the porous material divided by the number of confined gas molecules[90], α is a constant reflecting the maximum molecular packing density, and σ is the LJ diameter for the gas molecules. In Eq.(41), $\alpha\sigma^3 / v_{free}$ may be interpreted as the fraction of the free space inside the pore occupied by gas molecules. In the limit of closest packing, we may estimate α from that for spherical particles in a face-centered-cubic lattice

$$\alpha_{FCC} = \sqrt{2}/2 \tag{42}$$

Eq.(42) provides a first-order estimate for α if no additional information is available. For best agreement with simulation or experimental data, however, α may be used as an adjustable parameter. While this parameter varies slightly for different systems depending on crystal structure, it is independent of the thermodynamic conditions of the bulk gas including temperature and pressure.

The Knudsen model applies to gas diffusion at infinite dilution

$$D_K = \lim_{r_b \to 0} D_s \tag{43}$$

where the limiting value can be obtained from performing MD simulation at low gas pressures. Excess-entropy scaling accounts for contributions due to gas-gas interactions inside the pore, estimated from Rosenfeld's scaling rule[91]

$$D_E = \frac{0.585}{r_{av}^{1/3}} \sqrt{\frac{k_B T}{m}} \exp\left(0.788 S^{ex} / N k_B\right) \tag{44}$$

where m represents the molecular mass, r_{av} is the average number density of gas molecules inside the porous material, and N represents the total number of adsorbed gas molecules. With the excess entropy calculated from classical DFT, the hybrid method provides an efficient procedure to predict the self-diffusion coefficient of gas molecules in nanoporous materials as a function temperature and bulk pressure[27].

2.3. Results and Discussion

Adsorption in slit pores

The four classical DFT methods considered in this work have been calibrated in previous publications by extensive comparison with simulation data for inhomogeneous Lennard-Jones (LJ) fluids in model systems near a planar wall or in slit pores. At conditions near vapor-liquid equilibrium, the mean-field approximation (MFA) fails to reproduce the depletion of a LJ fluid near a hard or weakly attractive surface, while the first-order mean-spherical approximation (FMSA) performs rather well in comparison with simulation[80,89]. Surprisingly, all free-energy functionals including MFA are highly accurate for predicting the adsorption of LJ fluids in slit pores. Regrettably, previous publications were mostly

focused on comparisons for model systems at low temperatures (<200 K) that have little relevance to practical methane storage.

In this work, the classical DFT methods are first tested with simulation results for methane adsorption in slit pores of different widths and surface energies at room temperature (298 K). Figure 2 shows theoretical predictions for total adsorption and comparison with simulation data. FMSA overestimates total adsorption if the surface is weakly attractive, while the opposite holds for MFA predictions. Conversely, both weight-density approximations (WDA-L and WDA-Y) agree very well with simulation data at all conditions (Figure 2a). For adsorption in slit pores with more attractive walls (Figure 2b), the three versions of non-mean-field methods give virtually identical results. However, MFA underestimates total adsorption compared to simulation data. The poor performance of MFA is somewhat anticipated because it neglects correlation effects due to van der Waals attractions. Because correlation effects contribute to a negative chemical potential, consideration of the correlation contribution would increase total adsorption.

Adsorption and delivery capacities

The performance of different DFT methods for methane adsorption in porous materials may not be fully consistent with that for simple systems. To illustrate, we consider methane adsorption in two representative MOF materials, MOF-5[7] and Cu-BTC[92], at room temperature. Figure 3 compares total adsorption predicted from different classical DFT methods with results from GCMC simulation. Overall, the four versions of classical DFT methods all show good agreement with simulation data. However, their accuracies are slightly different for different materials. In stark contrast to their performance in slit

pores, MFA and FMSA are more accurate than WDA-L and WDA-Y for gas adsorption in MOF-5 at room temperature over the entire range of testing pressures. Both WDA methods overestimate total adsorption especially at intermediate pressures. For methane adsorption in Cu-BTC, however, WDA-Y reproduces GCMC data very well. While WDA-L and FMSA slightly underestimate the storage capacity at moderate pressures, total adsorption predicted by MFA is noticeably smaller than those from other DFT methods at high gas loadings. As indicated in our previous study[79], the performance of classical DFT methods for gas adsorption in nanoporous materials depends also on testing conditions.

For potential applications to material discovery, the classical DFT methods should be calibrated in the context of multiscale modeling and benchmarked with a large set of experimental data. While novel computational methods for predicting the crystal structures of framework materials and their interactions with gas molecules are rapid emerging[93], much work remains for systematic calibration of multiscale modeling methods. In this work, we confine our interest to comparing theoretical predictions with GCMC data for methane adsorption in over 1,000 MOF materials at various thermodynamic conditions. The crystal structures of these materials are from the Northwestern hypothetic MOF database[68], generated according to the topology of some common SBUs. These materials have been studied before for methane storage using GCMC simulations[68] and thus provide a good basis to test the performance of different classical DFT methods for materials screening. For validation of the theoretical performance, we consider only 1,200 materials from the MOF database, i.e., top 300 with the largest excess CH_4 adsorption in weight; top 300 with the largest excess CH_4 adsorption in volume; top 300 with the largest void fraction;

top 300 with the largest surface area (m^2/cm^3), all evaluated at 298 K and 35 bar. We believe that these materials are most important for studying methane adsorption and provide a good benchmark for calibration of the four classical DFT methods considered in this work.

Figure 4 shows theoretical results predicted by MFA in comparison with GCMC data. Similar comparisons for other classical DFT methods are presented in Supplementary Materials. In addition to total adsorption at 298 K, we consider also methane delivery for each material when the pressure is reduced from 35 bar to 5 bar at the same temperature. The thermodynamic conditions for the bulk gas are in line with the ARPA-E target for methane storage. Table 1 summarizes the root-mean-square deviations (RMSD) and theory-simulation correlation coefficients (the R values) for different classical DFT methods. In general, all four classical DFT methods show good agreements with the GCMC data for total methane adsorption at the ARPA-E target condition. Surprisingly, MFA gives the best results when compared to simulation data, with RMSD=7.90 $cm^3(STP)/cm^3$ and R^2=0.99. This functional is mathematically simpler than FMSA and weighted-density approximations; it is also numerically more stable and easier to converge in solving for the molecular density profiles. Although other methods show slightly larger deviations, the RMSD values are within about 6% of total adsorption.

The original target set by ARPA-E for CH_4 storage states that, at 298 K and 35 bar, the volumetric storage capacity should exceed 180 v/v for qualified nanoporous materials. Under such conditions, the adsorbed natural gas (ANG) will have an energy density comparable to that of the compressed natural gas (CNG) at the same temperature and 250

bar[68]. While that target can be easily reached by many MOF candidates, none of the existing materials meet the new ARPA-E target for methane storage in transportation vehicles[94]. The new ARPA-E target specifies not only the total gas uptake but also the delivery amount by nanoporous materials between compression at 35 bar and release at 5 bar at room temperature. In Figure 4b, we compare methane delivery predicted by MFA and GCMC methods. In general, the MFA predictions agree very well with the simulation data, especially for medium and high loading MOF materials. The deviation becomes more noticeable for materials with high total adsorption but low delivery. Considering the accuracy of MFA prediction for the total methane storage capacity at 298 K and 5 bar (Figure 4a), the large discrepancy for delivery may be attributed to numerical issues in our classical DFT calculations. Because those MOFs have large adsorption capabilities at both 35 and 5 bar, delivery is small and sensitive to numerical details.

Diffusivity

Classical DFT gives the density profile of gas molecules in a porous material that reflects the microscopic details of adsorbent-adsorbate interactions. Not only is the density profile related to the adsorption isotherm, it can also be used to identify important adsorbent-adsorbate interactions and predict other thermodynamic properties including enthalpy of adsorption and excess entropy. While the enthalpy of adsorption is important for practical applications, the excess entropy provides a convenient starting point for predicting transport coefficients over a broad range of thermodynamic conditions.

In our previous work[27], we have demonstrated that Rosenfeld's excess-entropy scaling method can be combined with the Knudsen model to predict the self-diffusivity of

gas molecules in various nanoporous materials. Because the excess entropy is readily available from adsorption calculations and the Knudsen model applies to gas diffusion at infinite dilution, the new computational procedure is much faster than traditional MD simulation methods for calculating the gas self-diffusivity over a broad range of thermodynamic conditions.

Figure 5 presents the self-diffusion coefficients of CH_4 in the two MOF materials considered above, MOF-5 and Cu-BTC, at 298 K over a broad range of pressures. The theoretical results are calculated according to Eq.(41). With α treated as an adjustable parameter ($a = 0.42$), the extended excess entropy scaling method is able to reproduce the simulation data almost quantitatively. Semi-quantitative results are attainable with approximation $a \approx a_{FCC}$.

Figure 6 shows the self-diffusivities of CH_4 in the top five MOFs that, as identified below, show the highest volumetric delivery (see Table 3). Here temperature is fixed at 298 K, and α is an adjustable parameter for each material. Again, the extended excess entropy scaling method reproduces the simulation data very well over the entire range of pressures; the approximation $a \approx a_{FCC}$ leads to semi-quantitative agreement between theory and MD simulation data. Interestingly, the MOF materials with top delivery show similar gas diffusivity at both low and high loadings, even though their relative ranks are slightly different.

Characteristics of "good" adsorbents

Conventional thermodynamic models for gas adsorption such as Langmuir and BET isotherms presume that, at a given bulk condition, the total gas uptake is linearly

proportional to available adsorbent surface area (or accessible surface area). Whereas ambiguity might arise in its definition (or measurement) for a particular porous material, the surface area has been routinely used as an important measure for identification of promising MOFs with large adsorption capability. The significance of surface area has been rarely challenged even for widespread applications of simulation methods.

To find possible correlations between gas adsorption capability and materials surface area, we plot methane adsorption versus accessible surface area[95,96] for 1,200 MOFs materials at 298 K and 35 bar. While Figure 7a shows some positive correlation for total adsorption, no trend in Figure 7b correlates the accessible surface areas and delivery. More important, if one focuses on the top MOF candidates for methane storage (see Figure 8), neither the simulation results nor the classical DFT predictions exhibit any convincing relationship between those two quantities. The decoupling of delivery from the (accessible) surface area is somewhat anticipated because although the geometric accessible surface areas are calculated based on the locus of the surface potential minimum, it only accounts for one gas molecule at a time. The surface area does not take into consideration the correlation between adsorbed gas molecules that is important, especially for candidates with high loading capacities. Conversely, the BET surface area is nicely correlated with adsorption because it is obtained from fitting to the gas adsorption data. Therefore, good correlation between BET surface area and adsorption capability is not surprising.

According to Figures 4 and S1, a material with high methane adsorption capacity does not warrant a large delivery at the ARPA-E conditions. While adsorption capacity appears to be in good correlation with the void fraction, such correlation does not exist for

the top candidates. Conversely, Figure 4b shows that MOFs with high CH_4 weight adsorption coincide with those with high delivery, suggesting that it may serve as a good indicator to identify promising materials for methane storage.

ARPA-E MOVE target

Methane delivery capacities for all MOF materials considered in this work are below 160 cm^3/cm^3, far below the ARPA-E target 315 cm^3/cm^3. To achieve the desired volumetric delivery, we could either increase the gas uptake at the compressed stage or reduce the remnant amount upon release. Table 2 summarizes the performance of the top 10 MOFs identified from different theoretical methods if we set the initial pressure to 250 bar, the same as that in a compressed natural gas tank (CNG). According to this table, the top materials identified by GCMC are in good agreement with those from various classical DFT methods. For the top candidates, the list of MOFs generated from FMSA agrees the best with that from simulation, with 9 out of 10 materials identical.

If the initial compression pressure is set to 250 bar, many MOFs may meet the target for weight delivery of 0.5 g/g, and the best material is able to achieve up to 95% of the volumetric ARPA-E target. If we raise the release temperature to 358 K, the ARPA-E volumetric target may also be reached (see Table S1). Alternatively, the ARPA-E target can be reached by reducing the initial storage temperature to 233 K, the lowest operation temperature according to DOE instructions. In that case, many MOFs could reach the ARPA-E target by compression at 75 bar and release at 298 K and 5 bar (see Table S2). At higher release temperature, all top 10 MOFs achieve the ARPA-E methane storage target for both gravimetric and volumetric targets (see Table 2).

Unlike the results shown in Table 1, the classical DFT and GCMC methods predict different top 10 candidates to meet the ARPA-E target (see Table 2). Nevertheless, all these materials exhibit similar adsorption capabilities. The GCMC candidates are among the top 50 materials identified by the classical DFT methods. In both Tables 1 and 2, there are about 3% numerical discrepancies between DFT and GCMC data. Considering 5% statistical error in typical GCMC simulations, we believe the classical DFT methods should be sufficiently accurate to identify promising MOF materials for further experimental investigations.

2.4. Conclusions

We have calibrated four versions of classical density functional theory (DFT) for potential applications to the discovery of novel metal-organic frameworks (MOFs) for methane storage. Overall, the classical DFT methods show good agreement with the simulation results for methane adsorption in slit pores as well as in MOF-5 and Cu-BTC. Their relative performance is sensitive to thermodynamic conditions and depends also on the specific material under consideration. Using the ARPA-E methane delivery capabilities of over 1,200 MOFs as the benchmark, we find that, surprisingly, the results from the mean-field approximation (MFA) agree best with the simulations data, with a root-mean-square deviation (RMSD) of only 7.90 cm^3(STP)/cm^3. Considering its theoretical simplicity, we conclude that MFA is probably the best choice for screening nanostructured materials for methane storage. While this work focuses on methane adsorption and shows that classical DFT is a promising computational tool for materials screening, a similar conclusion holds for adsorption of other gases including those with partial atomic charges,

provided that an accurate Helmholtz energy functional is available. Working along this direction is under current investigation and will be reported in future publications.

Whereas the BET surface area is conventionally used as a benchmark to identify nanoporous materials with large adsorption capacity, we find that, in general, there is no convincing correlation between a geometric surface area and the net delivery at conditions relevant to methane storage. While none of the existing materials satisfies the ARPA-E target, many MOFs can be identified to give a weight delivery exceeding 0.5 g/g if the initial compression pressure is modified to 250 bar, the same as that in a compressed natural gas tank. The volumetric target may also be reached if the release temperature is raised to 358 K. Alternatively, the ARPA-E target can be fulfilled by reducing the initial storage temperature to 233 K, the lowest operation temperature according to DOE instruction.

The classical DFT is computationally extremely efficient when compared to conventional simulation methods, in particular for calculating thermodynamic properties for a large library of materials over a broad parameter space. Figure 9 shows the statistics of the computational time for implementing classical DFT calculations on a single desktop computer (*i.e.*, one 3.0 GHz Sandy Bridge CPU core). The average computational time is within 2 minutes for each sample, which is faster than that for conventional GCMC simulation by more than one order of magnitude. DFT provides quantitative information on the excess entropy that can be used for predicting gas self-diffusivities in porous materials, important for practical applications but extremely time-consuming to calculate using conventional simulation methods. Good performance and computational efficiency make classical DFT a suitable choice for high-throughput calculations.

Figure 2-1. Computational materials design involves quantum mechanical (QM) calculations for understanding the chemistry of individual building blocks and the microscopic structure for molecules and solids, and statistical-mechanical (SM) calculations to predict their performance under diverse thermodynamic conditions. Because multiple approaches are available for both QM and SM calculations, practical procedures for multiscale modeling should be calibrated with extensive experimental data in terms of both theoretical accuracy and computational efficiency.

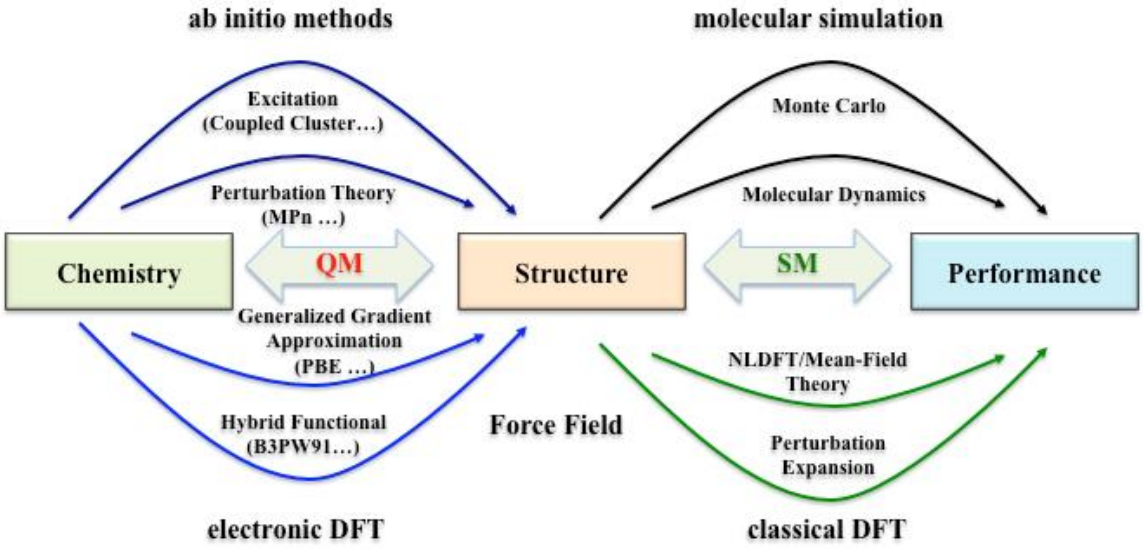

Figure 2-2. a) Methane adsorption in slit pores of reduced width H/σ =2, 3, 4 from top to bottom at 298K. The interaction between the gas molecule and each wall is described with Steele's 10-4-3 potential, where $\sigma_w = \sigma$, $\varepsilon_w = 3.142\varepsilon$ and $\Delta = 0.7071\sigma$; b) The same as a) except $\varepsilon_w = 6.283\varepsilon$.

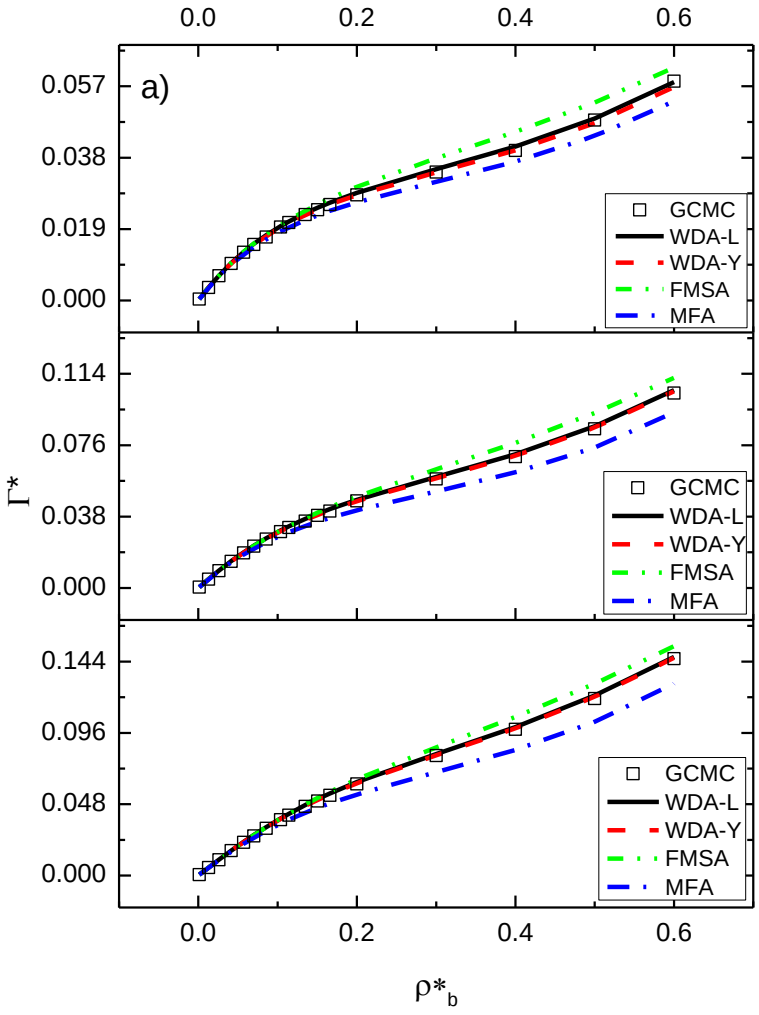

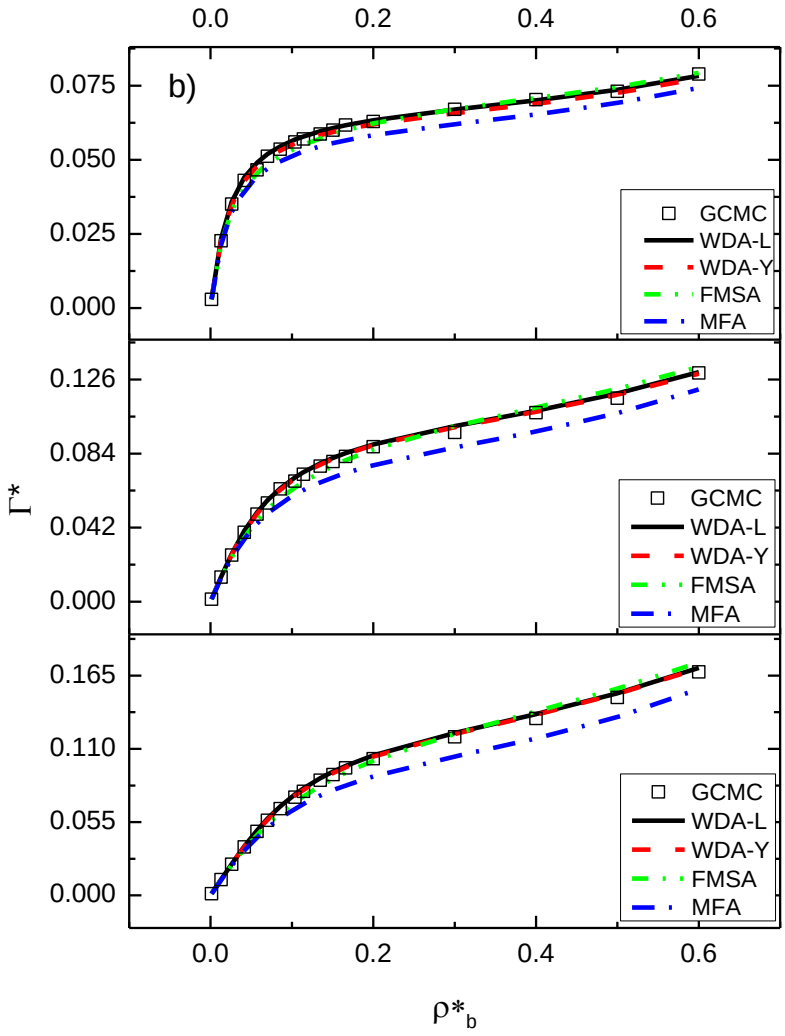
b)
GCMC
WDA-L
WDA-Y
FMSA
MFA
Γ*
ρ*b
0.0
0.2
0.4
0.6
0.075
0.050
0.025
0.000
0.126
0.084
0.042
0.000
0.165
0.110
0.055
0.000

Figure 2-3. Methane adsorption isotherms at 298K for a) MOF-5 and b) Cu-BTC framework materials calculated from GCMC simulation and from different classical DFT methods.

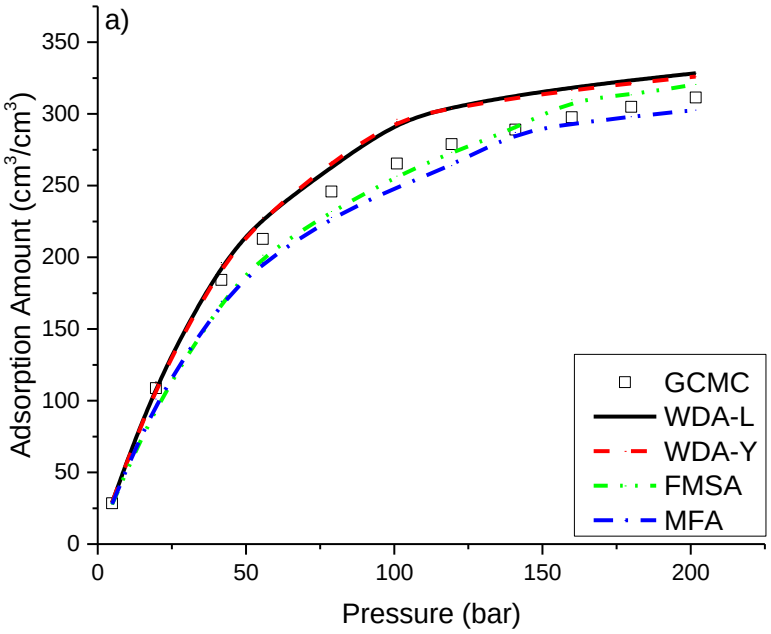

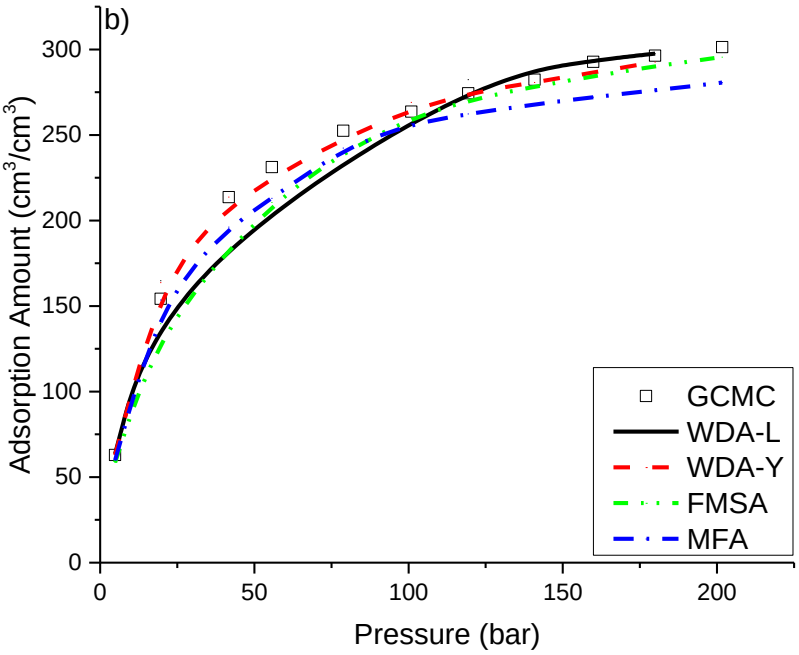
b)
Adsorption Amount (cm3/cm3)
Pressure (bar)
0
50
100
150
200
250
300
GCMC
WDA-L
WDA-Y
FMSA
MFA

Figure 2-4. Comparison of methane adsorption at 298 K in 1,200 MOFs calculated from GCMC and from MFA methods. a) Total adsorption amount at 5 bar; b) Delivery amount between 35 bar and 5 bar. Color code: Navy blue, top 300 from excess CH_4 adsorption in weight category; Red, top 300 from excess CH_4 adsorption in volume category; Purple, top 300 from void fraction category; Sky blue, top 300 from surface area (m^2/cm^3) category from the Northwestern Hypothetical MOF Database.

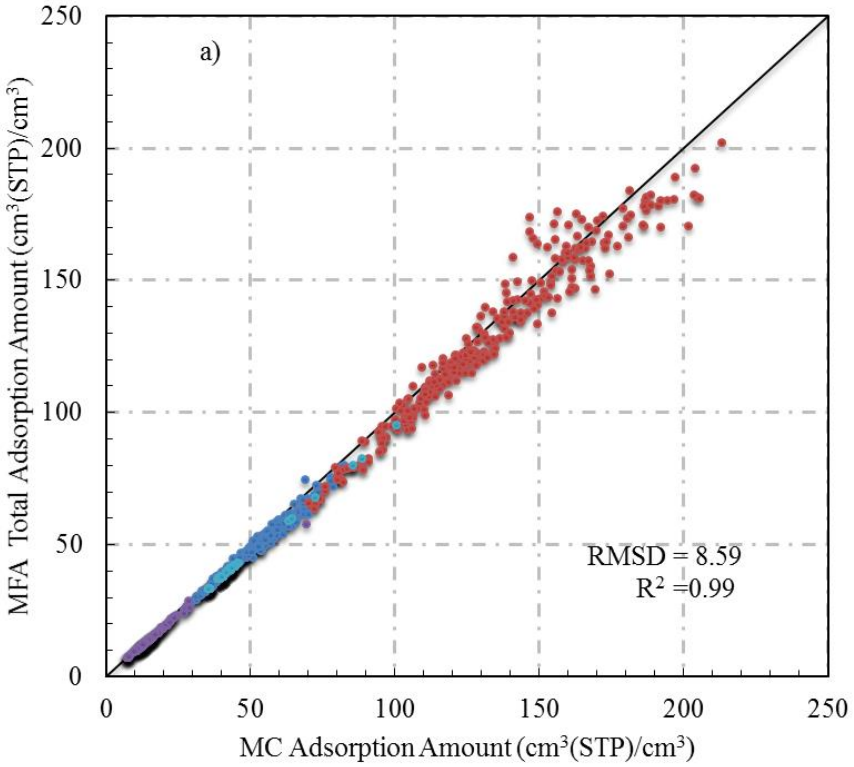

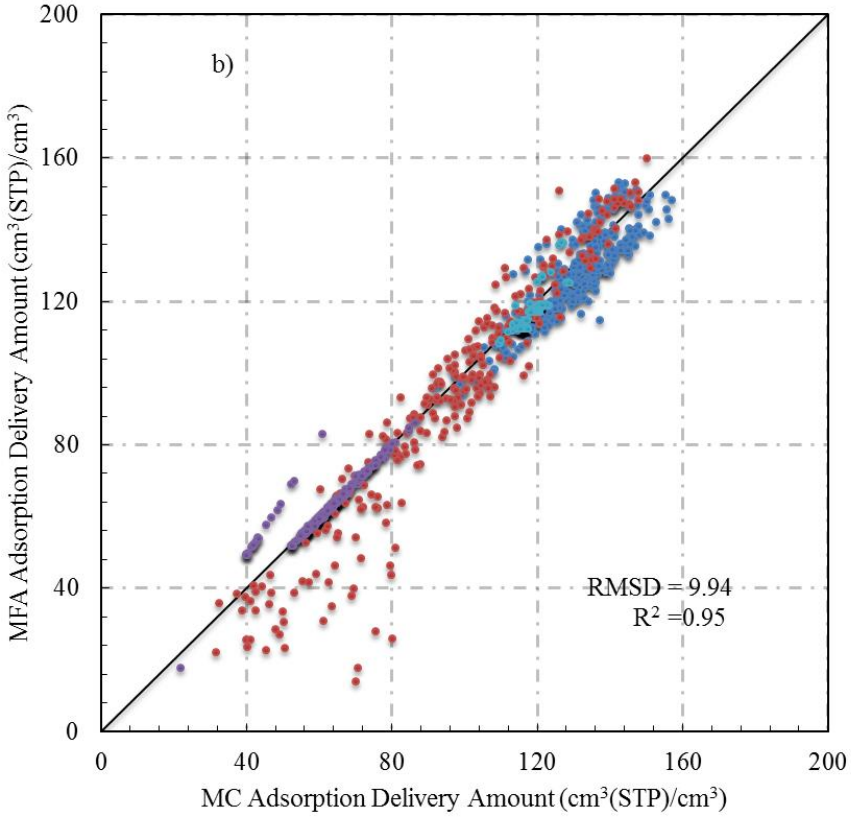
b)
RMSD = 9.94
R² =0.95
MFA Adsorption Delivery Amount (cm³(STP)/cm³)
MC Adsorption Delivery Amount (cm³(STP)/cm³)
0
40
80
120
160
200

Figure 2-5. Self-diffusivities of CH_4 molecules in MOF-5 and Cu-BTC at 298 K predicted by MD simulation and by the extended excess-entropy scaling method, respectively. Filled dots are results from MD simulations, while the lines are obtained from the extended excess-entropy scaling method.

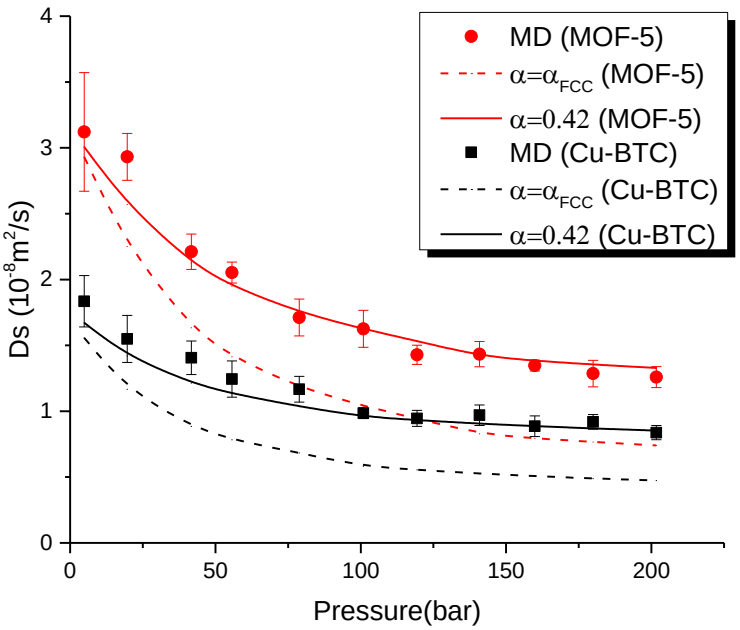

Figure 2-6. Self-diffusivities of CH_4 in top 5 MOFs with the highest volumetric delivery amount for compression at 233 K and 75 bar and release at 358 K and 5 bar predicted by FMSA method. The symbols are self-diffusion coefficients predicted by MD simulation, and the lines are from the extended excess-entropy scaling method.

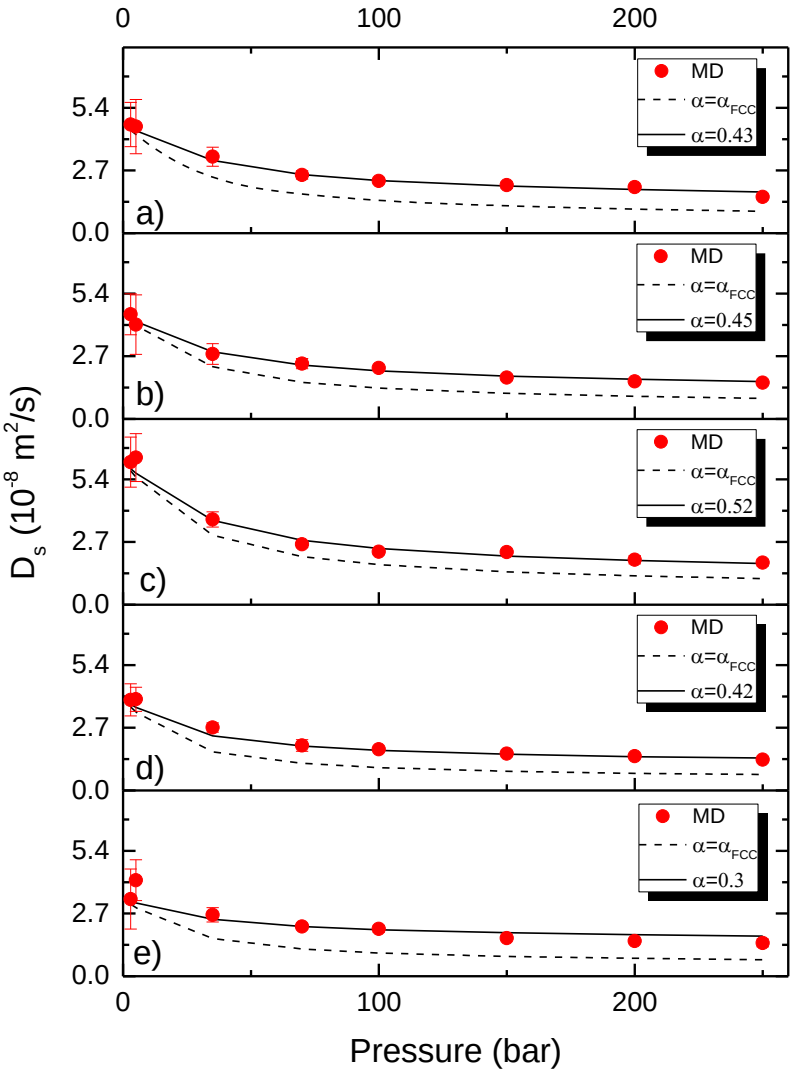

Figure 2-7. Adsorption of methane in 1,200 MOFs at 298 K and 35 bar as a function of the accessible surface area calculated according to the MFA and GCMC methods. a) Total adsorption amount; b) Delivery amount. Green dots: DFT data; Red dots: GCMC data.

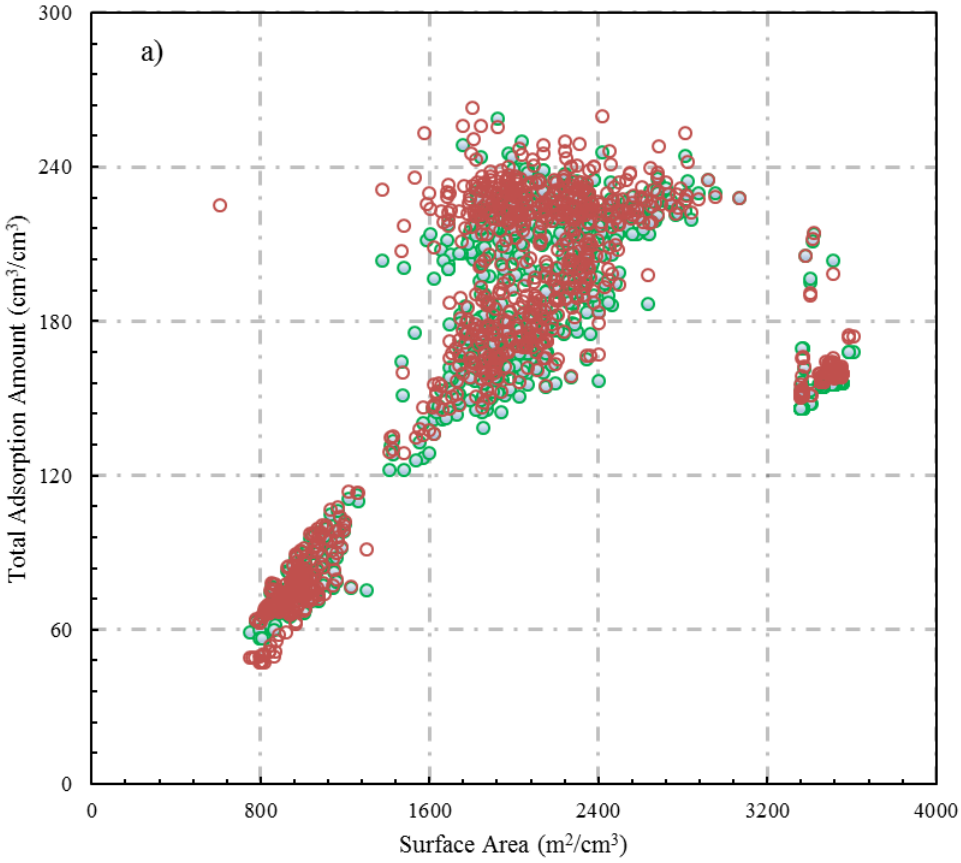

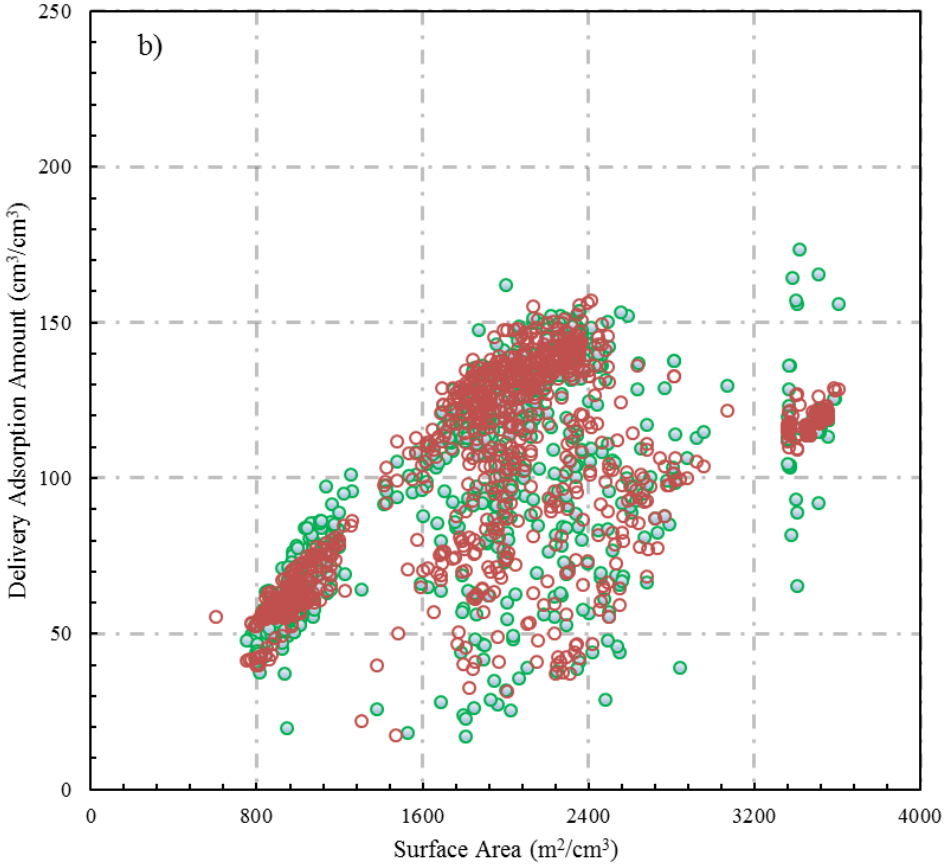
b)
250
200
150
100
50
0
Delivery Adsorption Amount (cm³/cm³)
0
800
1600
2400
3200
4000
Surface Area (m²/cm³)

Figure 2-8. Top 10 MOF candidates with the highest adsorption amounts of methane at 298 K and 35 bar as a function of the accessible surface area. Cycles: predicted by GCMC; Diamonds: predicted by MFA, while filled ones stand for total adsorption amounts and blank ones for delivery amounts between 298 K, 35 bar and 298 K, 5 bar

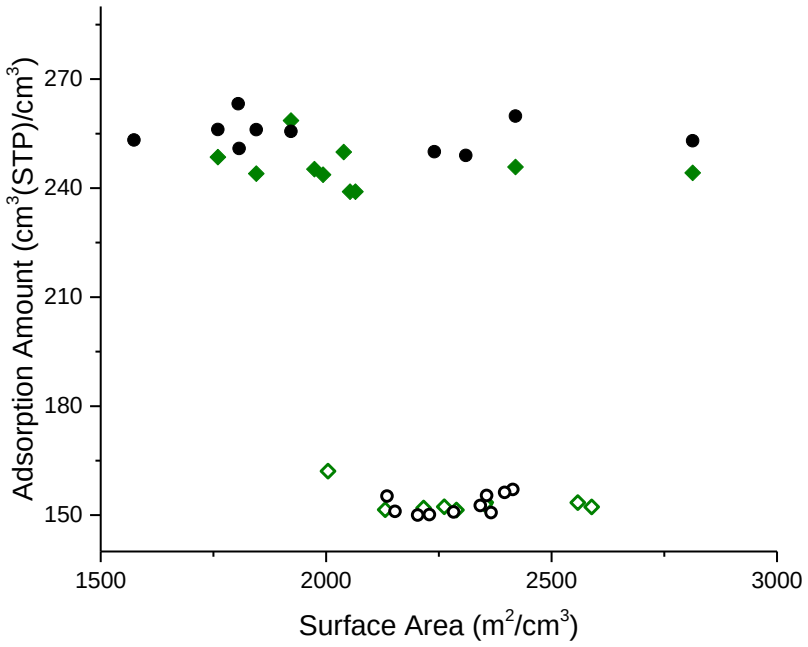

Figure 2-9. Distribution of computational time for predicting methane adsorption in 1,200 MOFs with MFA.

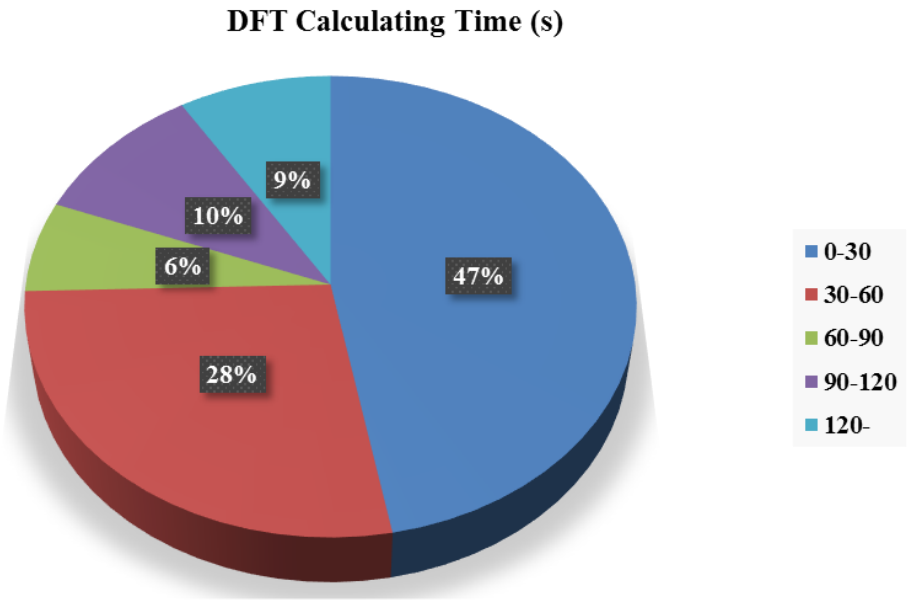

Support Information

Figure S2-1 Comparison of CH_4 absolute adsorption amount at 298 K and 35 bar in 1,200 MOFs calculated from GCMC and from different classical DFT methods: a) WDA-Y b) WDA-L c) FMSA d) MFA. Color code: Navy blue, top 300 from excess CH_4 adsorption in weight category; Red, top 300 from excess CH_4 adsorption in volume category; Purple, top 300 from void fraction category; Sky blue, top 300 from surface area (m^2/cm^3) category from the Northwestern Hypothetical MOF Database.

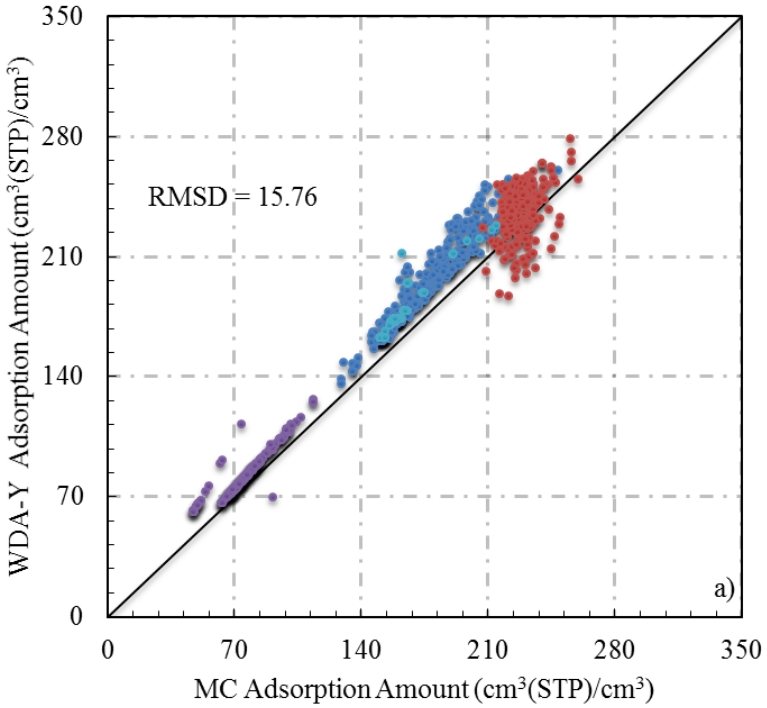

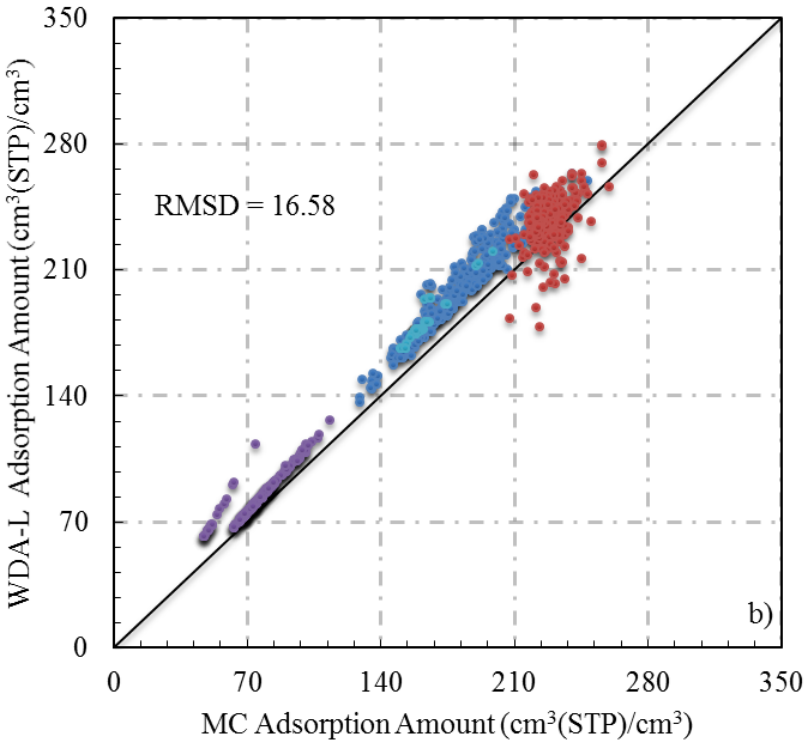
RMSD = 16.58
WDA-L Adsorption Amount (cm³(STP)/cm³)
MC Adsorption Amount (cm³(STP)/cm³)
0
70
140
210
280
350
b)

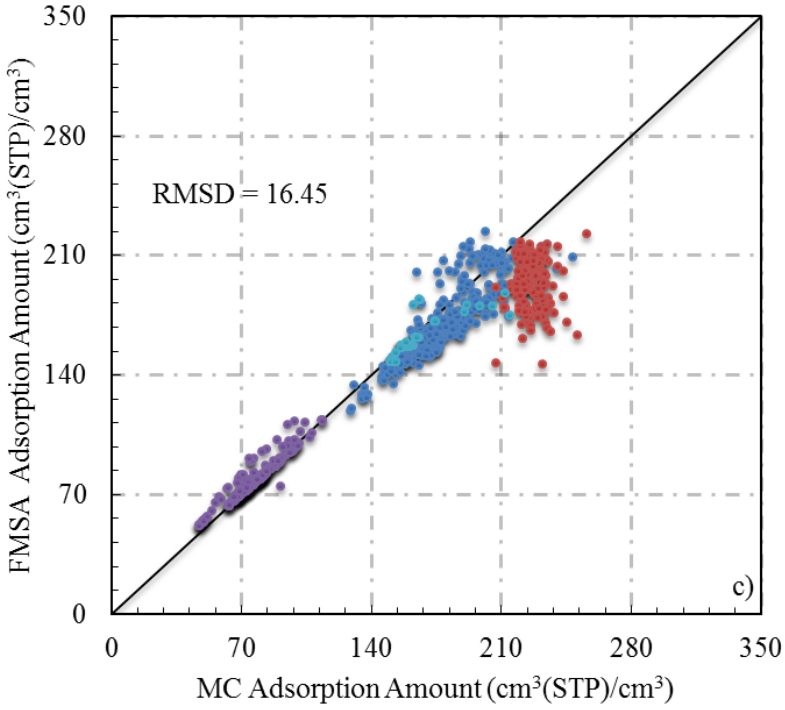
RMSD = 16.45
FMSA Adsorption Amount (cm³(STP)/cm³)
MC Adsorption Amount (cm³(STP)/cm³)
0
70
140
210
280
350
c)

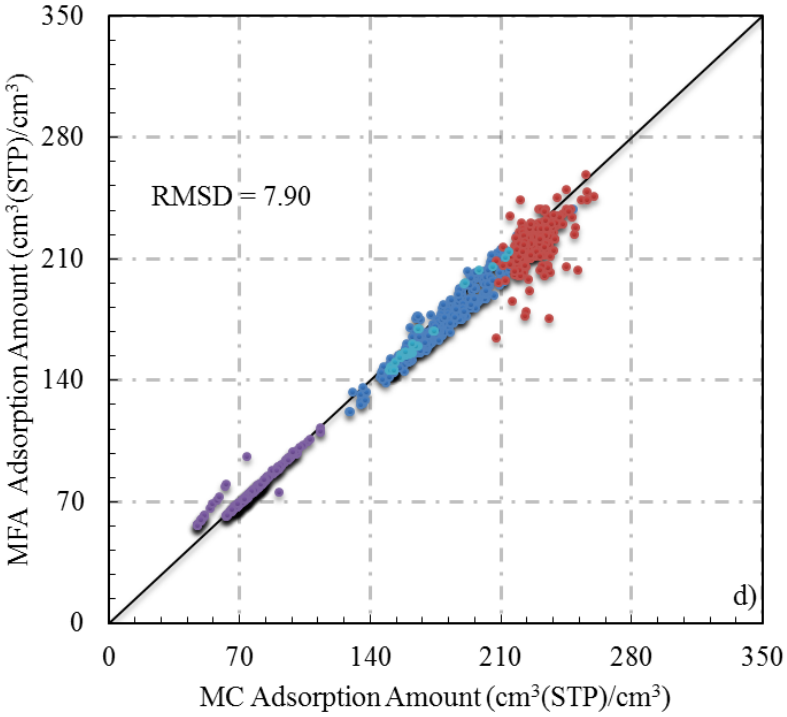
RMSD = 7.90
d)
MFA Adsorption Amount (cm³(STP)/cm³)
MC Adsorption Amount (cm³(STP)/cm³)
0
70
140
210
280
350

Table S2-1 Top 10 MOF candidates identified by GCMC and by various classical DFT methods according to the CH_4 volumetric delivery amount between compression at T=298 K, P=250 bar and release at T=358 K, P=5 bar.

	FMSA			MFA			WDA-Y			GCMC		
Rank	**No.**	**$\Gamma_{del,V}$**	**$\Gamma_{del,M}$**	**No.**	**$\Gamma_{del,V}$**	**$\Gamma_{del,M}$**	**No.**	**$\Gamma_{del,V}$**	**$\Gamma_{del,M}$**	**No.**	**$\Gamma_{del,V}$**	**$\Gamma_{del,M}$**
1	1101	314.8	0.66	1026	293.7	0.46	1101	322.3	0.68	1031	309.0	0.60
2	1089	313.6	0.65	1033	292.9	0.49	1213	322.1	0.69	1111	307.0	0.60
3	1031	313.6	0.61	1013	292.6	0.46	1111	322.0	0.63	1089	307.0	0.64
4	1033	312.4	0.52	1011	292.5	0.46	1031	321.7	0.63	1030	306.8	0.59
5	1111	312.2	0.61	1022	292.4	0.47	1089	321.1	0.67	1032	306.7	0.52
6	1213	311.7	0.67	1019	291.3	0.44	1025	321.0	0.62	1101	306.7	0.64
7	1025	311.2	0.60	1197	290.7	0.45	1064	319.9	0.60	1011	306.4	0.48
8	1026	311.2	0.49	1028	289.7	0.44	1145	318.6	0.65	1034	306.2	0.60
9	1064	310.9	0.58	1046	289.4	0.42	1053	317.9	0.60	1086	305.5	0.62
10	1011	310.8	0.48	1098	289.2	0.44	1011	317.6	0.49	1213	305.2	0.66

*: The No. stands for the serial number in the Northwestern Hypothetical MOF Database, while the 1st digit means the category (1 for excess CH_4 adsorption in weight category; 2 for excess CH_4 adsorption in volume category; 3 for void fraction category; 4 for surface area (m^2/cm^3) category), the last 3 digits means the rank in the category. Γ_{del} means delivery amount, where V stands for adsorption amount in units of $cm^3(STP)/cm^3$ and M stands for adsorption amount in units of g/g

Table S2-2 Top 10 MOF candidates predicted by GCMC and various DFT methods according to CH_4 volumetric delivery amount between compression at T=233 K, P=75 bar and release at T=298 K, P=5 bar.

	FMSA			MFA			WDA-Y			GCMC		
Rank	**No.**	**$\Gamma_{del,V}$**	**$\Gamma_{del,M}$**	**No.**	**$\Gamma_{del,V}$**	**$\Gamma_{del,M}$**	**No.**	**$\Gamma_{del,V}$**	**$\Gamma_{del,M}$**	**No.**	**$\Gamma_{del,V}$**	**$\Gamma_{del,M}$**
1	1031	305.3	0.60	1033	294.7	0.49	1111	335.2	0.66	1145	317.1	0.64
2	1101	302.0	0.63	1031	292.3	0.57	1025	333.0	0.64	1089	317.0	0.66
3	1111	301.8	0.59	1055	290.5	0.52	1034	331.1	0.65	1162	317.0	0.62
4	1025	301.0	0.58	1022	290.2	0.46	1041	330.8	0.65	1213	316.8	0.68
5	1089	300.9	0.63	1111	289.9	0.57	1064	329.0	0.62	1101	316.3	0.66
6	1213	300.5	0.65	1026	289.9	0.45	1030	328.9	0.63	1031	315.7	0.62
7	1037	300.1	0.55	1011	289.8	0.45	1086	328.3	0.66	1297	312.4	0.53
8	1052	299.7	0.60	1098	287.6	0.44	1055	324.6	0.58	1064	312.1	0.59
9	1055	299.5	0.54	1064	286.8	0.54	1188	324.4	0.67	1111	311.7	0.61
10	1034	299.3	0.58	1071	286.8	0.50	1297	323.7	0.55	1055	311.6	0.56

Table S2-3 CH_4 volumetric adsorption amounts of top 300 MOF candidates from excess CH4 adsorption in weight category, predicted by GCMC and MFA methods at T=298 K, P=35 bar, and delivery amount, releasing at T=298 K, P=5 bar, in the unit of cm^3/cm^3.

#	**Total.$_{MC}$**	**Total.$_{DFT}$**	**Delivery$_{MC}$**	**Delivery$_{DFT}$**
1	188.06	183.74	137.01	135.12
2	197.40	185.26	148.22	138.67
3	184.57	173.15	143.41	134.46
4	211.66	198.97	146.66	137.76
5	210.22	199.45	146.92	140.15
6	187.83	175.35	138.96	128.26
7	191.14	177.26	145.14	133.09
8	189.79	177.34	141.43	132.08
9	179.49	169.75	129.37	122.14
10	180.55	178.37	133.71	133.16
11	203.56	194.55	149.78	147.00
12	183.93	178.79	135.77	131.77
13	200.71	196.21	150.03	148.07
14	196.62	193.01	137.94	137.38
15	179.09	173.69	131.39	128.04
16	181.25	182.47	125.58	128.51
17	205.29	206.25	139.44	146.32
18	189.16	175.00	144.97	133.20
19	211.75	199.41	155.43	145.70
20	193.24	195.52	138.03	145.70
21	221.14	222.41	141.07	147.19
22	188.79	191.26	140.79	145.85
23	209.94	215.27	135.62	148.31
24	197.63	185.94	144.99	136.18
25	172.89	161.75	136.62	127.76
26	188.67	189.61	137.79	144.34
27	162.69	151.74	117.52	108.91
28	211.75	197.16	156.27	143.18
29	217.07	205.43	157.07	148.34
30	171.57	160.83	134.80	125.80
31	170.49	158.41	135.92	125.45
32	189.25	176.39	144.87	134.44
33	178.70	181.50	135.84	141.46
34	170.02	157.36	135.02	124.15
35	175.00	165.86	126.13	118.03

36	204.76	209.34	144.03	153.00
37	178.45	165.90	138.97	128.29
38	174.15	165.15	135.48	128.21
39	204.26	208.53	143.06	152.33
40	189.89	193.47	131.84	141.36
41	167.10	155.59	132.57	122.92
42	196.13	193.89	140.82	141.31
43	208.38	211.85	135.84	146.54
44	196.97	199.04	143.53	149.12
45	197.56	200.23	144.04	150.75
46	199.22	198.69	142.28	148.31
47	201.11	188.99	152.65	142.16
48	203.90	205.85	139.44	148.90
49	188.87	179.03	129.03	119.83
50	218.23	223.69	142.35	153.48
51	187.40	178.86	129.01	121.19
52	162.20	151.36	130.43	120.88
53	163.83	167.75	111.25	116.05
54	192.41	182.39	135.38	127.96
55	165.78	168.35	125.72	130.54
56	170.83	162.71	130.32	124.64
57	185.22	175.86	124.65	119.12
58	171.55	160.17	129.59	119.04
59	202.25	192.46	147.68	141.11
60	152.79	144.86	110.82	105.06
61	192.74	195.03	139.72	147.13
62	202.57	203.48	141.50	149.53
63	200.89	202.93	142.71	148.91
64	173.02	161.58	134.48	125.04
65	212.84	214.73	135.25	139.38
66	166.62	156.26	122.04	111.72
67	180.43	172.79	135.51	130.05
68	159.86	151.18	111.66	105.50
69	165.11	176.99	117.49	131.71
70	193.24	200.81	142.05	151.95
71	181.66	170.02	140.13	130.59
72	206.39	205.98	140.38	147.35
73	213.70	205.68	145.35	140.40
74	147.39	141.57	110.44	107.27
75	178.53	167.27	133.14	124.17

76	212.22	200.54	145.29	137.98
77	202.05	186.74	135.71	124.48
78	187.90	192.73	132.59	141.12
79	182.64	172.11	135.53	125.96
80	209.45	194.65	140.92	131.66
81	180.77	173.07	128.27	122.45
82	161.16	170.66	116.73	128.46
83	207.95	213.79	135.95	150.31
84	184.71	178.48	135.12	131.53
85	181.97	170.15	140.29	130.22
86	160.86	150.39	126.74	118.00
87	178.48	168.01	135.24	127.18
88	211.45	197.99	139.36	129.54
89	158.04	145.45	126.58	115.42
90	190.12	194.02	136.72	146.40
91	174.77	168.63	132.38	128.18
92	191.11	180.31	138.05	128.79
93	189.11	175.93	146.92	135.50
94	198.54	186.42	149.35	139.39
95	201.43	186.91	150.88	138.40
96	178.22	167.61	131.70	120.70
97	166.69	157.76	129.26	122.45
98	189.27	191.71	141.13	146.68
99	193.62	181.92	145.43	136.24
100	185.27	179.16	140.07	135.64
101	146.43	144.69	115.39	115.06
102	215.59	212.72	147.15	151.42
103	184.99	184.49	131.71	133.33
104	162.66	165.03	117.89	121.82
105	223.84	222.11	143.94	147.51
106	194.37	191.39	135.63	136.41
107	159.58	161.08	117.50	120.16
108	220.97	211.44	151.02	149.93
109	192.93	187.13	141.33	138.11
110	134.96	131.67	98.86	96.99
111	163.47	158.70	127.42	124.79
112	227.47	226.55	142.11	147.55
113	183.43	179.91	129.98	129.10
114	175.84	172.48	123.47	119.27
115	138.04	133.11	99.76	95.47

116	240.07	234.82	134.54	138.10
117	165.73	165.02	126.69	128.06
118	172.35	177.60	129.80	137.15
119	234.03	225.03	133.27	131.48
120	203.14	199.69	138.30	138.03
121	222.61	223.85	141.34	148.79
122	146.59	145.92	105.35	107.19
123	181.87	180.54	135.87	137.13
124	154.81	153.23	109.08	110.32
125	200.58	198.31	138.58	139.35
126	231.28	228.72	134.29	138.22
127	186.56	185.31	126.31	126.16
128	159.91	156.49	124.94	123.29
129	229.72	228.06	141.23	146.44
130	175.86	172.27	134.31	132.94
131	177.65	178.04	118.74	119.61
132	153.12	150.15	117.93	116.88
133	177.19	176.22	127.37	128.89
134	181.65	178.59	138.24	136.88
135	145.52	141.94	106.76	103.46
136	169.94	167.89	129.97	129.75
137	170.61	166.18	116.99	117.01
138	210.12	206.57	140.33	139.40
139	159.78	157.53	120.53	120.53
140	175.37	173.58	132.49	133.53
141	203.41	203.41	145.79	149.79
142	164.10	160.96	114.50	111.90
143	166.33	167.84	109.71	113.05
144	227.11	222.82	132.60	137.85
145	150.20	149.30	117.39	118.19
146	185.37	181.36	134.09	132.64
147	150.59	152.64	113.87	116.88
148	187.16	184.98	130.29	130.98
149	195.71	193.21	138.76	138.87
150	164.00	161.21	108.63	107.93
151	223.34	218.95	141.50	140.59
152	234.74	228.45	139.56	136.20
153	187.63	186.84	127.38	129.19
154	175.85	175.18	134.57	135.60
155	201.99	199.50	137.26	138.09

156	239.85	233.81	135.42	140.37
157	173.56	169.05	123.42	119.83
158	168.03	165.01	110.47	107.35
159	165.75	169.50	121.38	126.71
160	136.01	136.06	97.24	98.75
161	147.24	148.05	109.63	111.58
162	154.88	154.24	120.52	121.93
163	194.63	197.12	137.36	142.98
164	209.62	205.74	135.98	135.15
165	172.84	169.99	121.50	119.38
166	174.78	172.39	133.06	132.47
167	177.18	172.49	130.39	127.67
168	177.45	166.21	139.18	130.16
169	177.37	171.05	127.88	122.50
170	197.20	186.11	143.79	135.84
171	204.61	199.79	145.53	146.44
172	182.63	186.46	129.77	135.83
173	194.72	183.48	141.80	134.34
174	182.38	176.28	139.35	135.59
175	172.22	162.00	123.71	116.14
176	176.16	172.89	125.82	123.44
177	209.64	204.85	147.56	146.97
178	167.13	158.07	128.86	122.41
179	177.05	167.75	128.63	122.23
180	196.36	202.24	133.80	142.96
181	216.52	205.90	143.06	136.11
182	173.63	172.35	131.46	131.70
183	183.95	177.58	131.96	128.22
184	207.55	211.45	136.63	145.02
185	189.06	179.43	134.26	126.27
186	193.08	194.76	136.12	142.15
187	209.99	198.49	146.21	138.09
188	152.78	144.60	121.73	115.33
189	163.61	156.68	121.13	115.94
190	135.14	128.03	103.40	97.75
191	194.18	198.99	130.87	142.20
192	178.68	175.00	129.69	127.70
193	174.62	166.99	120.61	113.61
194	221.20	222.62	132.12	144.32
195	171.55	166.05	125.38	121.48

196	153.50	147.65	119.23	115.49
197	195.23	185.38	146.97	139.86
198	150.66	145.73	117.37	113.41
199	187.90	175.14	132.76	120.97
200	197.93	186.95	136.25	128.67
201	179.94	167.68	130.85	120.14
202	186.75	177.60	144.27	137.23
203	158.79	158.18	125.78	127.00
204	173.82	164.19	126.08	118.34
205	145.78	144.66	111.66	111.94
206	164.81	155.69	122.41	114.35
207	128.84	122.03	99.39	93.99
208	196.21	181.39	134.10	120.25
209	186.05	181.09	132.92	129.76
210	130.26	133.24	91.89	95.92
211	135.80	126.74	108.09	101.03
212	171.64	160.77	123.07	113.36
213	148.55	138.43	119.53	111.09
214	209.60	201.20	150.71	145.80
215	163.22	155.63	126.86	120.80
216	155.55	147.03	111.45	104.52
217	172.20	168.12	131.61	129.83
218	200.45	189.81	143.02	135.88
219	177.04	167.51	134.64	127.56
220	183.01	173.07	135.06	127.92
221	197.08	186.85	140.77	134.66
222	157.93	149.40	123.00	116.02
223	171.33	164.05	130.47	125.20
224	200.81	190.55	141.28	133.06
225	169.67	159.43	129.70	121.58
226	248.54	238.68	138.14	129.40
227	157.58	151.91	123.71	120.02
228	162.01	155.27	125.34	120.27
229	202.22	189.86	142.80	134.32
230	168.54	161.27	130.46	125.06
231	206.00	189.26	137.24	114.90
232	167.69	157.86	114.85	106.62
233	134.87	125.90	107.89	100.64
234	170.70	162.92	131.37	125.74
235	157.93	153.67	121.22	118.28

236	182.70	167.96	131.98	116.66
237	151.63	144.50	111.28	105.95
238	205.20	212.07	126.68	140.24
239	169.86	160.49	135.08	127.73
240	214.06	204.31	132.78	125.19
241	129.11	122.20	97.89	91.71
242	179.08	183.33	132.54	139.59
243	156.60	149.81	118.46	111.93
244	203.38	190.38	135.92	123.10
245	201.62	190.36	137.89	128.81
246	208.50	210.41	130.59	136.16
247	151.42	143.57	118.54	112.86
248	177.20	168.73	135.36	128.86
249	156.39	150.61	122.87	118.55
250	157.96	149.09	120.68	113.73
251	218.05	209.61	155.23	149.95
252	166.62	175.06	120.71	131.80
253	168.05	161.52	128.15	123.02
254	201.04	195.48	132.79	128.47
255	174.49	166.43	125.13	119.20
256	137.46	128.61	104.10	96.04
257	165.64	158.30	123.65	116.52
258	170.29	162.72	126.38	120.44
259	172.09	167.73	133.16	131.14
260	165.69	160.77	121.91	119.22
261	179.77	176.22	125.34	123.52
262	185.09	176.56	133.96	128.26
263	175.68	166.01	124.16	114.95
264	165.69	157.54	121.90	112.87
265	193.49	181.78	129.84	120.25
266	173.00	167.33	129.44	126.19
267	189.90	184.53	136.23	133.50
268	191.93	202.80	120.26	135.30
269	146.67	140.57	112.99	108.20
270	171.06	165.44	126.48	123.58
271	196.40	186.96	139.30	133.21
272	159.93	151.29	124.89	117.94
273	209.06	202.27	135.43	130.10
274	168.13	161.77	131.51	127.64
275	183.64	186.11	134.53	140.07

276	176.22	169.03	127.35	121.96
277	187.99	192.46	133.15	140.03
278	201.77	191.74	137.31	131.49
279	166.51	165.30	115.37	113.75
280	164.15	175.42	122.51	136.20
281	189.54	181.91	133.88	126.68
282	215.41	205.93	133.10	125.94
283	174.75	171.06	128.73	127.77
284	150.38	142.06	113.49	104.79
285	203.07	195.93	147.90	144.25
286	221.10	212.84	139.39	133.34
287	193.80	183.50	136.97	130.09
288	175.36	164.90	131.13	122.78
289	190.40	179.97	125.48	114.61
290	195.97	187.16	145.40	140.04
291	167.00	156.79	132.72	124.92
292	205.72	197.50	132.95	125.01
293	159.51	152.71	124.88	119.88
294	169.53	161.87	123.49	116.89
295	155.75	147.17	115.55	107.54
296	174.91	166.33	130.46	124.66
297	176.84	162.95	140.11	128.03
298	174.00	167.45	133.38	128.52
299	165.71	177.32	113.28	127.65
300	187.07	189.79	134.19	140.69

Table S2-4 CH_4 volumetric adsorption amounts of top 300 MOF candidates from excess CH4 adsorption in volume category, predicted by GCMC and MFA methods at T=298 K, P=35 bar, and delivery amount, releasing at T=298 K, P=5 bar, in the unit of cm^3/cm^3.

#	**Total.$_{MC}$**	**Total.$_{DFT}$**	**Delivery$_{MC}$**	**Delivery$_{DFT}$**
1	253.01	244.20	101.56	98.63
2	259.83	245.83	46.55	43.88
3	263.20		89.27	
4	247.30	238.92	116.18	99.47
5	248.09	234.05	77.30	
6	244.94	249.92	128.26	139.64
7	243.04	235.93	102.28	99.89
8	240.32	229.73	104.29	94.42
9	236.35	220.64	64.35	46.51
10	245.07	238.68	134.67	129.40
11	253.25		80.22	
12	246.24	237.08	78.50	81.78
13	240.07	234.82	134.54	138.10
14	246.36		57.73	
15	256.08	243.98	94.92	93.18
16	241.85	234.47	99.38	98.62
17	239.85	233.81	135.42	140.37
18	233.61	239.03	137.00	148.81
19	240.55	234.43	89.97	91.34
20	230.26	239.03	122.44	137.44
21	235.69	175.48	70.51	18.00
22	245.04	205.37	40.24	23.80
23	234.94	229.33	120.54	120.34
24	233.98	220.52	61.74	56.21
25	234.94	234.18	124.03	130.22
26	232.67	231.41	97.17	95.90
27	249.01		37.19	
28	256.14	248.52	87.82	83.96
29	238.50	221.24	84.13	83.40
30	255.60	258.58	116.23	129.46
31	235.29	228.16	104.53	105.12
32	242.74	230.24	98.11	93.44
33	239.53	230.84	77.84	
34	234.03	225.03	133.27	131.48
35	234.11	228.33	107.62	113.38

36	231.24	203.78	39.87	25.78
37	250.91	203.85	45.37	22.89
38	243.37	230.13	39.66	37.81
39	234.74	228.45	139.56	136.20
40	231.28	228.72	134.29	138.22
41	234.44	228.39	85.03	87.67
42	233.85	225.48	119.91	115.40
43	238.36	225.69	57.09	41.82
44	237.43	227.89	64.71	65.76
45	208.77	196.59	70.92	64.79
46	236.07	224.73	95.11	86.89
47	226.03	210.27	63.34	35.02
48	231.11	229.58	136.05	139.60
49	231.78	225.92	135.92	140.18
50	232.64		46.63	
51	232.25	218.42	69.80	71.39
52	231.58	220.96	76.16	62.52
53	236.13	231.86	92.70	97.74
54	231.21	239.00	119.29	126.90
55	229.80		70.25	
56	235.50	218.38	93.88	82.36
57	241.09	233.96	60.35	67.82
58	230.76	224.08	127.08	128.66
59	228.42	222.62	139.34	144.32
60	233.19	220.42	97.04	92.42
61	234.99	234.90	105.24	112.77
62	224.09	217.30	125.34	122.63
63	230.58	229.75	128.82	133.84
64	230.10	229.65	111.03	117.05
65	237.95	214.75	59.12	44.08
66	223.24	179.64	49.06	27.16
67	229.72	228.06	141.23	146.44
68	234.32		69.56	
69	227.34	229.95	100.08	106.60
70	222.73	217.12	92.01	87.60
71	250.02	227.91	37.17	
72	231.48	223.23	120.67	113.96
73	233.95	231.86	86.92	87.12
74	227.07	215.37	107.06	96.47
75	233.55	212.37	52.99	38.95

76	230.43	227.48	116.59	113.05
77	233.58		40.96	
78	226.07	230.71	141.32	151.52
79	225.59	226.84	97.24	100.23
80	232.15	225.87	103.64	93.61
81	229.03	221.48	86.56	78.96
82	227.66	222.31	104.22	99.83
83	231.81	223.08	97.85	85.11
84	229.10	226.22	102.81	107.45
85	231.92	226.33	86.27	88.81
86	237.90	235.52	68.26	66.66
87	226.67	224.98	108.32	118.41
88	227.11	222.82	132.60	137.85
89	231.56	228.94	77.24	77.41
90	227.47	226.55	142.11	147.55
91	226.98	228.64	107.73	109.85
92	230.68	227.19	124.28	128.05
93	228.48	211.54	67.21	64.01
94	229.12	223.04	91.22	89.10
95	230.39	223.06	90.81	92.95
96	228.73	229.10	106.27	114.19
97	228.50	223.55	74.50	74.41
98	235.23		40.99	
99	222.33	202.07	75.62	28.11
100	230.27		75.13	
101	230.10	220.46	101.24	89.39
102	225.48	211.62	64.90	65.94
103	236.22		87.21	
104	230.26	230.98	95.45	104.10
105	226.21	212.32	79.71	43.88
106	225.55	220.53	125.00	124.89
107	227.47	220.84	93.39	97.85
108	228.73	223.12	117.19	116.81
109	236.25	202.23	80.22	26.16
110	224.55	220.58	134.90	131.67
111	228.24	220.26	97.24	90.70
112	225.16	222.41	145.09	147.19
113	225.68	215.37	106.23	98.30
114	230.44	224.38	87.98	74.85
115	226.24	222.52	108.40	109.17

116	227.95	227.81	121.74	129.82
117	224.32	222.94	111.83	113.24
118	231.89	212.39	64.29	61.02
119	222.92	223.69	147.04	153.48
120	228.37	229.72	103.94	114.70
121	221.88	229.08	125.94	138.83
122	229.37	228.01	115.51	122.16
123	234.19		32.44	
124	229.58	222.74	81.60	83.40
125	227.88	216.29	72.16	62.84
126	227.69	227.72	132.28	133.13
127	216.45	207.05	78.26	58.28
128	222.96	176.69	70.19	17.01
129	230.51	219.27	83.73	77.80
130	229.06	214.87	70.01	56.96
131	238.51	221.36	42.02	40.92
132	229.79	219.24	71.53	62.29
133	225.01	227.02	134.16	144.50
134	229.50	223.93	87.86	87.87
135	227.19	222.86	101.39	103.36
136	212.24	197.83	86.99	74.42
137	223.34	218.95	141.50	140.59
138	222.61	223.85	141.34	148.79
139	229.32	226.23	77.39	82.47
140	219.93	205.82	81.45	78.17
141	234.97	226.68	72.46	68.95
142	222.66		56.79	
143	236.67	229.84	107.14	93.66
144	226.81	218.09	89.48	83.52
145	227.34	218.97	82.39	76.83
146	224.54	221.98	83.65	79.68
147	222.85	220.52	102.52	105.67
148	231.22	223.19	99.82	95.00
149	225.58	220.27	91.04	95.90
150	225.45	222.81	102.40	105.16
151	228.95		79.70	
152	229.37	217.32	56.34	52.84
153	233.68	215.41	46.72	38.57
154	219.33	200.46	72.77	
155	232.68		77.28	

156	221.84	220.88	112.55	103.69
157	222.18	215.27	147.86	148.31
158	226.43	213.00	59.50	55.63
159	221.01	218.27	118.24	115.76
160	214.08	208.25	75.63	62.95
161	226.96	214.37	96.23	92.69
162	224.78	226.67	101.06	109.65
163	226.77	217.54	126.34	115.90
164	224.81	220.36	96.74	100.85
165	229.55		76.40	
166	214.97	234.92	108.65	124.95
167	221.83	224.26	117.57	123.74
168	223.32	222.55	95.87	101.60
169	221.08	215.19	110.30	112.98
170	217.15		50.13	
171	222.86	212.77	62.73	41.75
172	222.24	216.83	112.24	108.88
173	221.46	210.47	109.75	104.31
174	229.10	227.66	67.93	73.61
175	222.97	217.69	107.55	108.87
176	220.13	200.06	82.55	63.83
177	224.77	224.26	120.67	119.56
178	225.36		62.99	
179	234.19		55.48	
180	222.62	218.87	101.23	106.82
181	215.06	207.02	103.20	96.00
182	233.08	237.62	108.68	117.54
183	225.29	220.38	97.24	102.38
184	225.47		86.58	
185	223.84	222.11	143.94	147.51
186	218.17	212.45	104.96	102.46
187	223.18		76.58	
188	227.02	214.21	65.20	55.51
189	224.97		55.62	
190	226.70	218.97	73.38	75.44
191	227.57	212.33	79.66	46.42
192	221.53	214.13	108.31	96.15
193	220.90	216.22	117.36	117.67
194	221.86	208.88	100.81	87.37
195	240.28	245.20	115.49	117.31

196	223.21	216.58	73.87	83.17
197	221.82	213.66	117.22	108.52
198	225.60	219.17	62.24	57.64
199	225.87	228.45	82.54	93.30
200	227.09		70.10	
201	222.72	216.74	92.36	97.06
202	221.75		81.06	
203	222.36	214.71	115.61	113.18
204	235.00	204.65	31.55	22.11
205	228.42	214.25	74.50	66.23
206	220.62	220.82	137.11	142.22
207	221.36	213.91	118.32	117.13
208	221.01	230.59	110.95	129.51
209	216.21	185.62	50.43	23.38
210	223.22		87.65	
211	224.99	226.94	106.34	115.40
212	218.47	215.43	80.79	77.44
213	225.88	218.95	92.28	92.47
214	230.90	218.53	64.76	54.40
215	218.84	220.49	142.88	148.63
216	220.59	224.13	92.63	101.50
217	221.30	220.66	109.29	112.84
218	231.50	227.65	81.08	78.60
219	215.14	211.26	136.03	132.28
220	221.69	218.68	136.49	139.54
221	221.66	209.99	97.39	88.20
222	222.53	215.88	94.43	83.91
223	229.13		59.12	
224	221.12	213.20	104.54	96.74
225	220.14	225.73	150.16	160.10
226	221.51	227.76	121.62	130.52
227	233.71	223.46	76.03	65.66
228	225.14	227.26	91.43	99.73
229	218.40	211.85	145.85	146.54
230	225.98	212.95	78.81	63.24
231	224.48	197.93	61.25	31.70
232	222.79	213.90	66.46	70.61
233	221.77	219.80	93.58	97.18
234	222.84	218.65	131.91	137.48
235	223.64	215.51	106.53	97.43

236	218.70		69.46	
237	229.08	214.40	42.44	34.01
238	222.09	219.56	99.75	98.54
239	224.52	215.42	101.87	98.20
240	235.13		53.48	
241	218.71	218.60	93.40	92.57
242	223.88	213.66	100.34	95.79
243	225.58	230.37	122.74	127.75
244	217.54	213.79	145.55	150.31
245	232.07	206.42	46.32	35.58
246	220.33	243.70	126.07	151.21
247	222.01	221.43	103.71	107.54
248	222.99	213.77	102.05	92.03
249	221.20	213.85	97.59	95.48
250	231.32	222.02	44.21	40.47
251	207.27		17.23	
252	234.57	227.70	37.45	39.22
253	234.05		66.73	
254	233.09	216.75	41.08	36.43
255	219.05	205.64	117.64	102.09
256	222.08	218.05	105.60	97.77
257	230.72	211.59	71.50	48.63
258	221.71	217.77	147.74	150.61
259	219.89	220.60	124.36	132.01
260	219.43	216.16	92.57	93.47
261	223.97	221.89	97.61	99.10
262	222.36	225.28	113.99	121.59
263	207.26	209.08	118.70	119.82
264	223.33	213.60	88.92	91.53
265	219.68	225.13	139.24	148.10
266	218.05	213.93	85.71	87.72
267	217.59	222.06	103.11	111.91
268	221.80	218.59	111.49	110.12
269	223.07	214.94	86.15	80.73
270	221.72	225.70	111.38	126.75
271	223.63	218.46	106.98	99.66
272	222.26	223.69	78.72	86.27
273	230.95	221.50	42.40	39.13
274	219.26	211.29	103.84	98.82
275	230.78	203.74	38.73	33.80

276	220.12	216.09	99.58	99.16
277	220.74	210.21	81.40	75.81
278	219.49		69.61	
279	217.32	217.78	120.74	123.18
280	218.19	216.29	109.28	111.24
281	218.42	214.42	116.45	113.85
282	210.88	216.80	97.40	105.40
283	218.26	208.58	112.50	114.72
284	219.65	218.90	137.84	145.44
285	236.24	211.62	50.09	33.66
286	221.49	213.70	134.71	134.11
287	222.48	215.63	73.63	72.88
288	225.88		41.00	
289	219.89	211.62	98.90	91.19
290	211.26		74.56	
291	218.73	215.74	114.53	117.60
292	221.26		61.58	
293	222.80	217.12	117.84	119.21
294	221.54	214.27	89.50	93.48
295	233.03	200.47	68.83	38.21
296	222.67	220.01	65.65	66.59
297	216.99	202.79	106.46	95.92
298	225.12	191.58	47.96	28.73
299	222.12	218.43	104.58	104.15
300	222.96		74.07	

*: Blank space means the DFT calculation doesn't converge, due to the numerical difficulty.

Table S2-5 CH_4 volumetric adsorption amounts of top 300 MOF candidates from void fraction category, predicted by GCMC and MFA methods at T=298 K, P=35 bar, and delivery amount, releasing at T=298 K, P=5 bar, in the unit of cm^3/cm^3.

#	**Total.$_{MC}$**	**Total.$_{DFT}$**	**Delivery$_{MC}$**	**Delivery$_{DFT}$**
1	64.04	63.06	53.51	52.98
2	74.66	73.39	61.19	60.54
3	77.80	75.60	63.36	62.02
4	68.93	68.11	56.68	56.41
5	68.55	67.30	56.73	56.05
6	75.36	74.56	61.45	61.14
7	63.64	63.02	53.05	52.93
8	63.16	61.88	52.72	51.92
9	67.61	66.72	55.91	55.54
10	78.91	77.51	64.01	63.51
11	64.88	63.93	53.98	53.50
12	63.20	62.00	52.74	52.01
13	74.65	72.97	61.50	60.57
14	74.35	72.03	61.53	59.88
15	74.35	72.97	61.28	60.57
16	68.20	67.00	56.16	55.52
17	72.21	70.86	59.63	58.90
18	86.70	85.57	69.09	68.81
19	68.54	67.19	56.55	55.76
20	91.28	75.52	21.99	17.87
21	78.52	77.32	63.71	63.35
22	63.12	62.22	52.69	52.20
23	75.69	73.90	61.86	60.86
24	65.61	64.62	54.50	53.99
25	65.88	64.57	54.84	53.97
26	68.77	67.72	56.73	56.20
27	73.33	72.03	60.45	59.88
28	68.29	67.75	56.05	56.01
29	84.19	82.81	67.21	66.71
30	91.79	89.98	72.45	71.39
31	78.00	76.54	63.21	62.46
32	72.95	72.09	59.90	59.73
33	74.65	72.97	61.50	60.57
34	69.19	68.11	56.83	56.37
35	68.73	68.04	57.30	57.12

36	89.06	87.24	70.49	69.86
37	69.25	68.21	56.98	56.50
38	100.40	97.41	77.96	76.30
39	80.08	78.53	64.83	64.10
40	68.90	67.78	56.90	56.32
41	67.51	67.19	56.29	56.41
42	88.34	86.19	70.55	69.22
43	80.35	78.84	64.88	64.32
44	74.63	73.59	61.57	61.05
45	77.66	76.29	63.19	62.42
46	72.50	71.73	59.87	59.73
47	69.07	68.14	56.52	56.24
48	76.36	74.67	62.27	61.39
49	79.87	78.78	64.45	64.21
50	72.66	71.73	60.12	59.73
51	69.92	69.27	57.55	57.39
52	72.08	71.34	59.24	59.11
53	99.32	97.78	75.04	74.47
54	84.57	82.59	67.77	66.51
55	66.64	65.49	55.25	54.60
56	80.27	78.39	65.16	64.13
57	67.33	67.11	56.18	56.37
58	90.86	89.05	71.56	70.72
59	74.54	73.80	61.14	61.04
60	69.48	68.18	57.27	56.49
61	97.23	95.69	73.02	72.48
62	97.76	96.85	75.24	75.28
63	62.72	61.83	52.28	51.87
64	68.02	66.76	56.11	55.36
65	79.07	77.45	64.04	63.31
66	73.41	71.87	60.47	59.53
67	77.59	75.69	63.68	62.40
68	80.78	79.97	65.10	65.10
69	89.28	87.77	70.30	69.92
70	68.43	67.08	56.26	55.55
71	82.13	80.39	66.25	65.35
72	81.95	79.86	65.89	64.77
73	68.82	67.60	56.48	55.86
74	66.36	65.58	54.86	54.63
75	62.64	62.05	52.24	52.06

76	66.56	65.38	55.19	54.47
77	49.19	59.11	41.64	51.69
78	80.39	78.81	64.72	64.06
79	69.93	68.26	57.31	56.29
80	67.80	66.80	55.94	55.48
81	97.99	96.88	74.60	73.97
82	80.47	78.67	64.81	63.77
83	66.41	65.31	55.08	54.50
84	80.99	79.36	65.39	64.63
85	81.72	80.08	65.63	64.98
86	68.05	66.63	56.18	55.28
87	113.36	112.48	84.69	83.85
88	66.27	65.96	55.13	55.31
89	69.45	68.54	56.89	56.55
90	63.21	62.04	52.69	52.06
91	67.26	66.24	55.77	55.38
92	73.94	72.03	61.05	59.88
93	68.26	66.96	56.09	55.42
94	72.59	71.04	59.78	58.92
95	68.27	67.01	57.06	56.29
96	69.56	68.45	57.25	56.67
97	82.12	79.99	66.47	65.25
98	69.09	67.56	57.00	55.94
99	72.46	71.49	59.25	58.89
100	69.07	68.26	56.59	56.33
101	88.31	86.70	70.78	70.05
102	70.74	70.08	57.90	58.00
103	79.03	77.73	63.98	63.52
104	82.79	80.95	66.60	65.66
105	85.10	83.84	68.41	67.94
106	70.87	69.99	58.49	58.21
107	80.38	78.91	64.70	64.15
108	83.19	81.28	67.10	65.99
109	71.92	70.12	59.15	57.98
110	72.51	70.81	59.85	58.83
111	68.05	67.45	55.92	55.94
112	49.34	59.30	41.81	51.90
113	106.84	104.85	79.18	78.35
114	73.31	71.85	60.48	59.51
115	75.64	74.00	62.04	61.09

116	95.79	94.46	76.08	75.63
117	81.66	80.04	66.13	65.33
118	74.49	73.96	61.11	61.14
119	82.95	81.24	67.62	66.62
120	73.66	71.87	60.59	59.54
121	72.13	70.72	59.04	58.21
122	82.51	81.02	66.21	65.68
123	66.91	66.24	55.08	55.00
124	49.02	59.00	41.41	51.55
125	95.58	93.88	75.29	74.58
126	104.04	103.01	80.85	80.66
127	75.95	74.95	62.02	61.74
128	81.93	80.69	65.76	65.38
129	81.96	80.11	65.98	65.03
130	88.85	87.35	71.26	70.44
131	80.38	78.95	64.66	64.25
132	94.71	93.91	75.09	75.17
133	50.52	60.90	42.76	53.27
134	77.07	75.47	62.87	62.04
135	80.27	78.23	65.02	63.88
136	51.37	61.90	43.19	53.88
137	67.99	66.83	56.07	55.39
138	69.48	68.80	58.01	57.78
139	68.24	67.03	56.94	56.30
140	72.20	70.92	59.47	58.85
141	68.30	67.50	56.25	55.88
142	80.51	79.09	64.75	64.16
143	72.20	71.49	59.44	59.35
144	81.77	80.86	66.07	65.93
145	72.59	70.80	59.94	58.88
146	69.49	68.09	57.09	56.26
147	77.57	76.04	63.04	62.36
148	73.87	71.94	60.75	59.54
149	90.51	89.83	71.04	71.61
150	69.73	68.99	58.21	57.97
151	69.42	68.53	57.65	57.26
152	68.49	67.60	56.29	55.89
153	71.57	71.10	59.06	59.16
154	78.35	77.29	63.63	63.30
155	79.81	78.39	64.33	63.74

156	83.57	82.36	67.07	66.82
157	80.03	78.97	64.21	63.94
158	73.27	71.67	60.24	59.35
159	66.30	65.74	55.25	55.18
160	79.49	78.57	63.75	63.71
161	87.30	88.04	70.08	71.44
162	96.22	95.45	73.67	73.56
163	92.51	91.03	73.46	72.50
164	80.51	79.20	64.91	64.58
165	107.64	106.25	80.16	80.47
166	76.53	75.21	62.34	61.88
167	84.97	84.79	67.16	67.70
168	73.74	72.57	61.53	60.89
169	81.41	79.95	65.25	64.72
170	84.46	84.02	69.04	69.20
171	71.89	70.67	59.14	58.61
172	74.58	72.86	61.43	60.41
173	76.82	75.96	63.07	62.87
174	74.78	74.05	61.65	61.42
175	71.75	71.16	59.87	59.79
176	90.27	88.89	71.63	71.44
177	76.05	75.27	61.73	61.48
178	85.82	84.13	68.52	67.67
179	71.60	70.49	59.13	58.63
180	73.91	72.86	60.73	60.26
181	71.36	70.03	58.58	57.81
182	80.53	79.69	64.63	64.58
183	66.53	65.57	55.53	55.02
184	47.75	57.10	40.39	49.89
185	79.29	78.56	64.05	64.07
186	73.55	73.07	61.24	61.28
187	81.32	79.98	65.70	65.22
188	94.61	93.87	75.58	75.83
189	50.20	60.41	42.41	52.77
190	66.16	65.31	55.17	54.79
191	92.43	91.02	73.24	72.47
192	69.86	68.88	58.32	57.88
193	72.99	71.62	60.00	59.27
194	94.21	92.51	74.58	74.10
195	78.13	76.95	63.18	62.78

196	99.74	98.19	77.59	76.98
197	92.20	91.56	73.67	74.05
198	85.54	83.92	68.42	67.80
199	53.99	66.13	45.38	57.65
200	90.58	90.09	72.27	72.71
201	81.23	79.99	66.54	66.00
202	79.68	78.92	64.53	64.61
203	72.80	71.28	60.16	59.18
204	74.94	74.42	61.95	61.81
205	47.49	56.66	40.14	49.48
206	49.71	60.01	41.95	52.36
207	72.03	71.07	59.45	59.03
208	81.53	79.69	65.64	64.77
209	68.54	67.98	57.17	57.04
210	68.61	67.45	56.28	55.70
211	97.14	95.86	74.76	74.42
212	71.79	70.68	59.13	58.63
213	90.89	89.78	73.09	72.88
214	96.17	93.88	75.55	74.39
215	51.28	62.39	43.13	54.32
216	79.94	79.24	64.21	64.36
217	73.16	72.37	60.06	59.93
218	76.47	75.39	63.22	62.64
219	79.77	78.93	64.67	64.63
220	76.16	74.90	62.07	61.58
221	68.50	67.44	56.66	56.06
222	73.30	71.89	60.32	59.53
223	81.60	80.39	66.07	65.59
224	71.26	70.47	59.23	58.94
225	78.86	77.73	63.77	63.41
226	113.21	110.19	86.39	86.19
227	78.12	77.83	63.19	63.62
228	79.81	79.41	64.61	64.93
229	100.78	98.17	79.46	78.70
230	55.66	68.74	46.69	59.89
231	76.73	75.93	62.45	62.31
232	72.12	70.91	59.34	58.81
233	68.76	67.55	56.45	55.86
234	73.53	72.73	60.68	60.51
235	67.43	67.24	56.16	56.41

236	71.81	71.07	58.98	58.89
237	47.54	56.60	40.18	49.40
238	83.54	82.25	68.65	68.10
239	79.74	78.75	64.38	64.11
240	81.93	80.92	65.81	65.67
241	73.70	72.80	60.87	60.53
242	98.41	98.11	76.90	77.24
243	98.79	98.61	78.48	79.24
244	47.40	56.82	40.12	49.67
245	77.53	76.02	62.99	62.29
246	73.27	72.28	60.22	59.83
247	67.67	66.96	56.44	56.20
248	79.90	78.46	64.66	63.86
249	74.76	74.08	61.10	61.15
250	77.36	76.15	63.79	63.20
251	83.57	82.83	68.28	68.04
252	57.95	71.19	48.45	61.84
253	77.30	76.87	62.38	62.59
254	47.32	56.69	40.00	49.50
255	77.54	76.57	62.51	62.24
256	80.79	79.49	64.76	64.48
257	77.46	75.97	63.17	62.52
258	71.19	69.41	58.74	57.53
259	74.01	73.40	60.62	60.68
260	76.50	75.67	62.51	62.33
261	79.80	79.61	64.55	65.13
262	78.77	76.98	64.15	63.17
263	75.64	75.15	62.33	62.40
264	82.29	80.67	66.43	65.71
265	73.60	72.66	60.69	60.30
266	78.67	76.90	63.98	62.94
267	67.59	66.64	56.51	55.97
268	74.11	96.23	60.95	83.19
269	100.68	99.16	76.96	76.58
270	74.07	73.00	61.07	60.51
271	79.94	79.37	64.24	64.50
272	80.85	79.97	66.40	66.04
273	78.80	78.22	63.49	63.69
274	62.18	78.70	52.28	68.96
275	68.83	68.72	57.00	57.36

276	79.77	79.21	64.37	64.50
277	63.09	79.98	53.09	70.08
278	80.29	78.86	65.21	64.65
279	79.58	78.57	65.81	65.34
280	98.84	98.52	77.99	78.79
281	89.85	88.12	71.69	71.50
282	73.36	72.38	60.30	59.89
283	81.46	79.85	65.36	64.66
284	74.73	73.70	60.32	60.05
285	71.90	71.28	60.07	59.90
286	77.02	75.75	62.40	61.82
287	65.90	65.26	54.90	54.74
288	73.45	72.15	60.49	59.78
289	78.27	77.00	64.71	63.97
290	47.23	56.61	39.93	49.45
291	76.66	76.15	63.95	63.97
292	51.45	61.93	43.32	53.94
293	49.60	59.69	41.89	52.12
294	74.46	73.46	61.17	60.67
295	73.29	72.83	60.24	60.30
296	101.93	101.29	80.09	80.60
297	83.46	82.51	66.64	66.58
298	113.51	110.92	84.72	84.78
299	59.15	73.06	49.44	63.44
300	72.73	71.78	60.08	59.64

Table S2-6 CH_4 volumetric adsorption amounts of top 300 MOF candidates from surface area (m^2/cm^3) category, predicted by GCMC and MFA methods at T=298 K, P=35 bar, and delivery amount, releasing at T=298 K, P=5 bar, in the unit of cm^3/cm^3.

#	**Total.$_{MC}$**	**Total.$_{DFT}$**	**Delivery$_{MC}$**	**Delivery$_{DFT}$**
1	174.20	168.18	128.72	125.36
2	173.64	168.18	127.98	125.36
3	174.47	168.18	128.90	125.36
4	159.61	155.96	120.85	118.82
5	159.62	155.96	120.45	118.82
6	159.74	155.96	120.94	118.82
7	158.25	155.96	119.16	118.82
8	159.61	155.96	120.85	118.82
9	161.14	155.96	121.82	118.82
10	160.17	155.96	120.94	118.82
11	159.74	155.96	120.94	118.82
12	159.74	155.96	120.94	118.82
13	159.74	155.96	120.94	118.82
14	159.74	155.96	120.94	118.82
15	159.74	155.96	120.94	118.82
16	159.74	155.96	120.94	118.82
17	159.74	155.96	120.94	118.82
18	159.74	155.96	120.94	118.82
19	159.51	155.96	120.76	118.82
20	159.74	155.96	120.94	118.82
21	161.63	155.96	122.48	118.82
22	159.61	155.96	120.85	118.82
23	162.23	155.96	123.18	118.82
24	159.74	155.96	120.94	118.82
25	159.74	155.96	120.94	118.82
26	161.01	155.96	122.07	118.82
27	159.74	155.96	120.94	118.82
28	160.74	155.96	121.56	118.82
29	159.61	155.96	120.85	118.82
30	159.32	155.96	120.18	118.82
31	159.74	155.96	120.94	118.82
32	159.89	155.96	121.19	118.82
33	159.74	155.96	120.94	118.82
34	161.34	155.96	122.18	118.82
35	159.74	155.96	120.94	118.82

36	159.74	155.96	120.94	118.82
37	161.15	155.96	122.17	118.82
38	159.51	155.96	120.76	118.82
39	160.77	155.96	121.51	118.82
40	159.61	155.96	120.85	118.82
41	159.48	155.96	120.45	118.82
42	160.18	155.96	121.03	118.82
43	159.74	155.96	120.94	118.82
44	159.74	155.96	120.94	118.82
45	159.74	155.96	120.94	118.82
46	158.50	155.96	119.72	118.82
47	159.35	155.96	120.43	118.82
48	159.51	155.96	120.76	118.82
49	160.40	155.96	121.49	118.82
50	159.74	155.96	120.94	118.82
51	159.74	155.96	120.94	118.82
52	161.24	155.96	122.07	118.82
53	161.01	155.96	122.07	118.82
54	161.01	155.96	122.07	118.82
55	159.74	155.96	120.94	118.82
56	159.29	155.96	120.20	118.82
57	160.79	155.96	121.92	118.82
58	159.74	155.96	120.94	118.82
59	159.74	155.96	120.94	118.82
60	160.74	155.96	121.56	118.82
61	159.51	155.96	120.76	118.82
62	159.74	155.96	120.94	118.82
63	160.74	155.96	121.56	118.82
64	159.74	155.96	120.94	118.82
65	160.74	155.96	121.56	118.82
66	158.42	155.96	119.56	118.82
67	161.01	155.96	122.07	118.82
68	159.48	155.96	120.11	118.82
69	159.74	155.96	120.94	118.82
70	159.74	155.96	120.94	118.82
71	161.01	155.96	122.07	118.82
72	159.74	155.96	120.94	118.82
73	159.51	155.96	120.76	118.82
74	159.74	155.96	120.94	118.82
75	159.95	155.96	120.98	118.82

76	159.61	155.96	120.85	118.82
77	159.74	155.96	120.94	118.82
78	159.48	155.96	120.51	118.82
79	159.32	155.96	120.18	118.82
80	160.74	155.96	121.56	118.82
81	159.29	155.96	120.20	118.82
82	159.32	155.96	120.18	118.82
83	159.61	155.96	120.85	118.82
84	159.32	155.96	120.18	118.82
85	159.74	155.96	120.94	118.82
86	159.74	155.96	120.94	118.82
87	159.74	155.96	120.94	118.82
88	160.74	155.96	121.56	118.82
89	159.32	155.96	120.18	118.82
90	159.61	155.96	120.85	118.82
91	159.74	155.96	120.94	118.82
92	159.53	155.96	120.29	118.82
93	161.34	155.96	122.04	118.82
94	158.42	155.40	118.34	117.30
95	159.36	155.40	119.10	117.30
96	159.65	155.40	119.58	117.30
97	158.37	155.40	118.40	117.30
98	158.54	155.40	118.44	117.30
99	158.01	155.40	117.71	117.30
100	160.20	155.40	119.75	117.30
101	158.42	155.40	118.34	117.30
102	158.42	155.40	118.34	117.30
103	158.42	155.40	118.34	117.30
104	158.69	155.40	118.63	117.30
105	158.54	155.40	118.44	117.30
106	159.96	155.40	119.71	117.30
107	158.60	155.40	118.63	117.30
108	159.03	155.40	119.01	117.30
109	159.52	155.40	119.08	117.30
110	158.45	155.40	118.73	117.30
111	159.52	155.40	119.08	117.30
112	158.42	155.40	118.34	117.30
113	158.54	155.40	118.44	117.30
114	159.70	155.40	119.67	117.30
115	159.03	155.40	119.01	117.30

116	160.19	155.40	119.94	117.30
117	159.52	155.40	119.08	117.30
118	158.19	155.40	118.09	117.30
119	159.52	155.40	119.08	117.30
120	159.70	155.40	119.58	117.30
121	158.54	155.40	118.44	117.30
122	158.42	155.40	118.34	117.30
123	158.42	155.40	118.34	117.30
124	160.78	155.40	120.64	117.30
125	159.52	155.40	119.08	117.30
126	158.54	155.40	118.44	117.30
127	157.67	155.40	117.69	117.30
128	158.45	155.40	118.73	117.30
129	158.37	155.40	118.40	117.30
130	158.42	155.40	118.34	117.30
131	158.37	155.40	118.40	117.30
132	158.54	155.40	118.44	117.30
133	158.42	155.40	118.34	117.30
134	160.20	155.40	119.75	117.30
135	159.65	155.40	119.58	117.30
136	163.65	159.82	121.08	119.18
137	159.60	155.40	119.44	117.30
138	159.65	155.40	119.58	117.30
139	158.42	155.40	118.34	117.30
140	158.42	155.40	118.34	117.30
141	163.87	159.82	121.05	119.18
142	160.20	155.40	119.81	117.30
143	159.40	155.40	119.26	117.29
144	159.03	155.40	119.01	117.30
145	158.42	155.40	118.34	117.30
146	159.70	155.40	119.58	117.30
147	160.56	155.40	120.52	117.30
148	160.70	155.40	120.38	117.30
149	158.42	155.40	118.34	117.30
150	158.42	155.40	118.34	117.30
151	158.42	155.40	118.34	117.30
152	163.65	159.82	121.08	119.18
153	158.37	155.40	118.40	117.30
154	163.58	159.82	120.87	119.18
155	158.37	155.40	118.40	117.30

156	158.42	155.40	118.34	117.30
157	159.12	155.40	119.16	117.30
158	158.42	155.40	118.34	117.30
159	159.76	155.40	119.52	117.30
160	159.38	155.40	119.49	117.30
161	158.42	155.40	118.34	117.30
162	158.42	155.40	118.34	117.30
163	158.42	155.40	118.34	117.30
164	158.42	155.40	118.34	117.30
165	158.42	155.40	118.34	117.30
166	158.42	155.40	118.34	117.30
167	158.42	155.40	118.34	117.30
168	159.94	155.40	120.30	117.30
169	158.42	155.40	118.34	117.30
170	158.42	155.40	118.34	117.30
171	160.23	155.40	120.18	117.30
172	159.12	155.40	119.16	117.30
173	159.52	155.40	119.08	117.30
174	158.11	155.40	118.32	117.30
175	158.61	155.40	118.74	117.30
176	158.54	155.40	118.44	117.30
177	198.48	203.54	126.06	135.80
178	163.65	159.82	121.08	119.18
179	165.44	159.82	122.48	119.18
180	163.43	159.82	120.77	119.18
181	159.12	155.40	119.16	117.30
182	163.65	159.82	121.08	119.18
183	159.65	155.40	119.58	117.30
184	158.42	155.40	118.34	117.30
185	158.42	155.40	118.34	117.30
186	158.12	155.40	117.73	117.30
187	163.65	159.82	121.08	119.18
188	158.42	155.40	118.34	117.30
189	158.42	155.40	118.34	117.30
190	158.19	155.40	118.09	117.30
191	158.42	155.40	118.34	117.30
192	163.65	159.82	121.08	119.18
193	159.45	155.40	119.48	117.30
194	159.40	155.40	119.30	117.30
195	158.42	155.40	118.34	117.30

196	159.73	155.40	119.51	117.30
197	159.56	155.40	119.15	117.30
198	163.65	159.82	121.08	119.18
199	163.65	159.82	121.08	119.18
200	164.24	159.82	121.28	119.18
201	159.52	155.40	119.08	117.30
202	158.42	155.40	118.34	117.30
203	158.54	155.40	118.44	117.30
204	163.65	159.82	121.08	119.18
205	163.65	159.82	121.08	119.18
206	158.42	155.40	118.34	117.30
207	163.65	159.82	121.08	119.18
208	163.65	159.82	121.08	119.18
209	163.65	159.82	121.08	119.18
210	163.76	159.82	121.15	119.18
211	163.65	159.82	121.08	119.18
212	163.65	159.82	121.08	119.18
213	162.88	159.82	120.13	119.18
214	163.84	159.82	120.84	119.18
215	164.38	159.82	121.40	119.18
216	156.39	154.49	113.51	113.66
217	156.39	154.49	113.51	113.66
218	156.39	154.49	113.51	113.66
219	156.39	154.49	113.51	113.66
220	156.39	154.49	113.51	113.66
221	156.39	154.49	113.51	113.66
222	157.83	154.49	115.06	113.66
223	157.58	154.50	114.38	113.67
224	157.87	154.49	114.81	113.66
225	157.83	154.49	115.06	113.66
226	157.38	154.49	114.33	113.66
227	157.87	154.49	114.81	113.66
228	158.70	154.49	115.92	113.66
229	156.39	154.49	113.51	113.66
230	156.39	154.49	113.51	113.66
231	158.66	154.49	115.45	113.66
232	156.39	154.49	113.51	113.66
233	156.39	154.49	113.51	113.66
234	156.39	154.49	113.51	113.66
235	156.39	154.49	113.51	113.66

236	156.39	154.49	113.51	113.66
237	158.75	154.74	117.29	115.25
238	156.39	154.49	113.51	113.66
239	156.39	154.49	113.51	113.66
240	156.39	154.49	113.51	113.66
241	159.36	155.55	116.33	114.92
242	159.40	155.56	116.45	114.92
243	159.64	155.55	116.99	114.92
244	214.51	213.98	114.06	118.89
245	212.07	210.89	123.66	128.46
246	151.19	147.93	109.63	108.42
247	190.10	195.34	127.12	136.47
248	150.98	147.93	109.30	108.42
249	191.10	196.44	126.66	136.60
250	156.34	152.99	113.19	111.82
251	205.37	205.49	120.06	125.70
252	162.55	161.43	118.01	119.67
253	151.40	145.88	116.06	112.52
254	166.04	169.52	121.50	127.23
255	152.01	145.88	116.27	112.52
256	152.90	145.88	117.51	112.52
257	165.46	169.42	121.25	127.21
258	151.20	145.88	115.61	112.52
259	152.82	145.88	117.19	112.52
260	152.41	145.88	116.75	112.52
261	151.40	145.88	115.96	112.52
262	151.96	145.88	116.46	112.52
263	150.96	145.97	115.36	112.57
264	151.20	145.88	115.61	112.52
265	158.60	156.44	114.17	114.43
266	152.01	145.88	116.27	112.52
267	152.40	146.00	116.99	112.60
268	151.96	145.88	116.46	112.52
269	151.88	145.88	116.43	112.52
270	151.40	145.88	115.96	112.52
271	152.82	145.88	117.19	112.52
272	151.40	145.88	115.96	112.52
273	153.14	150.28	110.02	109.27
274	165.70	169.51	121.33	127.22
275	150.47	145.97	114.91	112.57

276	151.52	145.88	116.06	112.52
277	151.37	145.88	115.87	112.52
278	151.76	145.97	116.26	112.57
279	152.01	145.88	116.27	112.52
280	151.98	145.94	116.47	112.58
281	151.08	146.01	115.48	112.61
282	151.01	145.88	115.69	112.52
283	151.95	145.88	116.49	112.52
284	151.20	145.88	115.61	112.52
285	152.16	145.97	116.56	112.57
286	152.01	145.88	116.27	112.52
287	151.37	145.88	115.83	112.52
288	152.01	145.88	116.27	112.52
289	150.95	145.88	115.59	112.52
290	151.07	145.88	115.56	112.52
291	151.96	145.88	116.46	112.52
292	151.49	146.00	116.18	112.60
293	152.02	145.88	116.53	112.52
294	151.40	145.88	115.96	112.52
295	150.02	145.88	114.44	112.52
296	152.01	145.88	116.27	112.52
297	150.62	145.88	115.27	112.52
298	155.56	153.20	111.92	111.71
299	150.84	145.97	115.36	112.57
300	152.90	145.88	117.51	112.52

References:

1. Yang Q, Liu D, Zhong C, Li J-R. Development of Computational Methodologies for Metal–Organic Frameworks and Their Application in Gas Separations. *Chemical Reviews.* 2013/10/09 2013;113(10):8261-8323.

2. Dincă M, Long JR. Hydrogen Storage in Microporous Metal–Organic Frameworks with Exposed Metal Sites. *Angewandte Chemie International Edition.* 2008;47(36):6766-6779.

3. Furukawa H, Miller MA, Yaghi OM. Independent verification of the saturation hydrogen uptake in MOF-177 and establishment of a benchmark for hydrogen adsorption in metal-organic frameworks. *Journal of Materials Chemistry.* 2007;17(30):3197-3204.

4. Murray LJ, Dinca M, Long JR. Hydrogen storage in metal-organic frameworks. *Chemical Society Reviews.* 2009;38(5):1294-1314.

5. Suh MP, Park HJ, Prasad TK, Lim D-W. Hydrogen Storage in Metal–Organic Frameworks. *Chemical Reviews.* 2012/02/08 2011;112(2):782-835.

6. Kondo M, Yoshitomi T, Matsuzaka H, Kitagawa S, Seki K. Three-Dimensional Framework with Channeling Cavities for Small Molecules: {[M2(4, 4′-bpy)3(NO3)4]·xH2O}n (M □ Co, Ni, Zn). *Angewandte Chemie International Edition in English.* 1997;36(16):1725-1727.

7. Eddaoudi M, Kim J, Rosi N, et al. Systematic Design of Pore Size and Functionality in Isoreticular MOFs and Their Application in Methane Storage. *Science.* 2002;295(5554):469-472.

8. Mason JA, Veenstra M, Long JR. Evaluating metal-organic frameworks for natural gas storage. *Chemical Science.* 2014;5(1):32-51.

9. Peng Y, Srinivas G, Wilmer CE, et al. Simultaneously high gravimetric and volumetric methane uptake characteristics of the metal-organic framework NU-111. *Chemical Communications.* 2013;49(29):2992-2994.

10. Wilmer CE, Farha OK, Yildirim T, et al. Gram-scale, high-yield synthesis of a robust metal-organic framework for storing methane and other gases. *Energy & Environmental Science.* 2013;6(4):1158-1163.

11. Guo Z, Wu H, Srinivas G, et al. A Metal–Organic Framework with Optimized Open Metal Sites and Pore Spaces for High Methane Storage at Room Temperature. *Angewandte Chemie International Edition.* 2011;50(14):3178-3181.

12. Ma S, Sun D, Simmons JM, Collier CD, Yuan D, Zhou H-C. Metal-Organic Framework from an Anthracene Derivative Containing Nanoscopic Cages Exhibiting High Methane Uptake. *Journal of the American Chemical Society.* 2008/01/01 2007;130(3):1012-1016.

13. Wu H, Zhou W, Yildirim T. High-Capacity Methane Storage in Metal−Organic Frameworks M2(dhtp): The Important Role of Open Metal Sites. *Journal of the American Chemical Society.* 2009/04/08 2009;131(13):4995-5000.

14. Chui SS-Y, Lo SM-F, Charmant JPH, Orpen AG, Williams ID. A Chemically Functionalizable Nanoporous Material [Cu3(TMA)2(H2O)3]n. *Science.* February 19, 1999 1999;283(5405):1148-1150.

15. Wilmer CE, Leaf M, Lee CY, et al. Large-scale screening of hypothetical metal − organic frameworks. *Nat Chem.* 2012;4(2):83-89.

16. Merkel TC, Freeman BD, Spontak RJ, et al. Ultrapermeable, Reverse-Selective Nanocomposite Membranes. *Science.* April 19, 2002 2002;296(5567):519-522.

17. Kamakoti P, Morreale BD, Ciocco MV, et al. Prediction of Hydrogen Flux Through Sulfur-Tolerant Binary Alloy Membranes. *Science.* January 28, 2005 2005;307(5709):569-573.

18. Li J-R, Sculley J, Zhou H-C. Metal–Organic Frameworks for Separations. *Chemical Reviews.* 2012/02/08 2011;112(2):869-932.

19. Balbuena PB, Gubbins KE. Theoretical interpretation of adsorption behavior of simple fluids in slit pores. *Langmuir.* 1993/07/01 1993;9(7):1801-1814.

20. Lastoskie C, Gubbins KE, Quirke N. Pore size heterogeneity and the carbon slit pore: a density functional theory model. *Langmuir.* 1993/10/01 1993;9(10):2693-2702.

21. Cracknell RF, Gordon P, Gubbins KE. Influence of pore geometry on the design of microporous materials for methane storage. *The Journal of Physical Chemistry.* 1993/01/01 1993;97(2):494-499.

22. Peng Y, Krungleviciute V, Eryazici I, Hupp JT, Farha OK, Yildirim T. Methane Storage in Metal–Organic Frameworks: Current Records, Surprise Findings, and Challenges. *Journal of the American Chemical Society.* 2013/08/14 2013;135(32):11887-11894.

23. Skoulidas AI. Molecular Dynamics Simulations of Gas Diffusion in Metal−Organic Frameworks: Argon in CuBTC. *Journal of the American Chemical Society.* 2004/02/01 2004;126(5):1356-1357.

24. Skoulidas AI, Sholl DS. Self-Diffusion and Transport Diffusion of Light Gases in Metal-Organic Framework Materials Assessed Using Molecular Dynamics Simulations. *The Journal of Physical Chemistry B.* 2005/08/01 2005;109(33):15760-15768.

25. Keskin S, Liu J, Rankin RB, Johnson JK, Sholl DS. Progress, Opportunities, and Challenges for Applying Atomically Detailed Modeling to Molecular Adsorption and Transport in Metal−Organic Framework Materials. *Industrial & Engineering Chemistry Research.* 2009/03/04 2008;48(5):2355-2371.

26. Rosenfeld Y. Relation between the transport coefficients and the internal entropy of simple systems. *Physical Review A.* 1977;15(6):2545-2549.

27. Liu Y, Fu J, Wu J. Excess-entropy scaling for gas diffusivity in nanoporous materials. *Langmuir.* 2013;29(42):12997-13002.

28. Düren T, Millange F, Férey G, Walton KS, Snurr RQ. Calculating Geometric Surface Areas as a Characterization Tool for Metal−Organic Frameworks. *The Journal of Physical Chemistry C.* 2007/10/01 2007;111(42):15350-15356.

29. Bae Y-S, Yazaydın AÖ, Snurr RQ. Evaluation of the BET Method for Determining Surface Areas of MOFs and Zeolites that Contain Ultra-Micropores. *Langmuir.* 2010/04/20 2010;26(8):5475-5483.

30. Frost H, Düren T, Snurr RQ. Effects of Surface Area, Free Volume, and Heat of Adsorption on Hydrogen Uptake in Metal−Organic Frameworks. *The Journal of Physical Chemistry B.* 2006/05/01 2006;110(19):9565-9570.

31. Myers AL. Thermodynamics of adsorption in porous materials. *AIChE Journal.* 2002;48(1):145-160.

32. Bhatia SK, Myers AL. Optimum Conditions for Adsorptive Storage. *Langmuir.* 2006/02/01 2006;22(4):1688-1700.

33. Lee S-J, Bae Y-S. Can Metal–Organic Frameworks Attain New DOE Targets for On-Board Methane Storage by Increasing Methane Heat of Adsorption? *The Journal of Physical Chemistry C.* 2014/08/28 2014;118(34):19833-19841.

34. Amrouche H, Creton B, Siperstein F, Nieto-Draghi C. Prediction of thermodynamic properties of adsorbed gases in zeolitic imidazolate frameworks. *RSC Advances.* 2012;2(14):6028-6035.

35. Sircar S. Basic Research Needs for Design of Adsorptive Gas Separation Processes. *Industrial & Engineering Chemistry Research.* 2006/08/01 2006;45(16):5435-5448.

36. Hartzog DG, Sircar S. Sensitivity of PSA process performance to input variables. *Adsorption.*1(2):133-151.

37. Steele WA. The physical interaction of gases with crystalline solids: I. Gas-solid energies and properties of isolated adsorbed atoms. *Surface Science.* 1973;36(1):317-352.

38. Rappe AK, Casewit CJ, Colwell KS, Goddard WA, Skiff WM. UFF, a full periodic table force field for molecular mechanics and molecular dynamics simulations. *Journal of the American Chemical Society.* 1992/12/01 1992;114(25):10024-10035.

39. Ma S, Sun D, Simmons JM, Collier CD, Yuan D, Zhou H-C. Metal-Organic Framework from an Anthracene Derivative Containing Nanoscopic Cages Exhibiting High Methane Uptake. *Journal of the American Chemical Society.* 2008/01/01 2008;130(3):1012-1016.

40. Chui SS-Y, Lo SM-F, Charmant JPH, Orpen AG, Williams ID. A Chemically Functionalizable Nanoporous Material [Cu₃(TMA)₂(H₂O)₃]_n. *Science.* 1999;283(5405):1148-1150.

41. Johnson JK, Zollweg JA, Gubbins KE. The Lennard-Jones equation of state revisited. *Molecular Physics.* 1993/02/20 1993;78(3):591-618.

42. Martin MG. 2013; http://towhee.sourceforge.net.

43. Plimpton S. Fast Parallel Algorithms for Short-Range Molecular Dynamics. *Journal of Computational Physics.* 1995;117(1):1-19.

44. Siderius DW, Gelb LD. Predicting Gas Adsorption in Complex Microporous and Mesoporous Materials Using a New Density Functional Theory of Finely Discretized Lattice Fluids. *Langmuir.* 2009/02/03 2009;25(3):1296-1299.

45. Li Z, Cao D, Wu J. Density-functional theory and Monte Carlo simulation for the surface structure and correlation functions of freely jointed Lennard-Jones polymeric fluids. *The Journal of Chemical Physics.* 2005;122(17):-.

46. Ye Z, Chen H, Cai J, Liu H, Hu Y. Density functional theory of homopolymer mixtures confined in a slit. *The Journal of Chemical Physics.* 2006;125(12):-.

47. Barker JA, Henderson D. Perturbation Theory and Equation of State for Fluids. II. A Successful Theory of Liquids. *The Journal of Chemical Physics.* 1967;47(11):4714-4721.

48. Cotterman RL, Schwarz BJ, Prausnitz JM. Molecular thermodynamics for fluids at low and high densities. Part I: Pure fluids containing small or large molecules. *AIChE Journal.* 1986;32(11):1787-1798.

49. Yu Y-X. A novel weighted density functional theory for adsorption, fluid-solid interfacial tension, and disjoining properties of simple liquid films on planar solid surfaces. *The Journal of Chemical Physics.* 2009;131(2):-.

50. Yu Y-X, Wu J. Structures of hard-sphere fluids from a modified fundamental-measure theory. *The Journal of Chemical Physics.* 2002;117(22):10156-10164.

51. Rosenfeld Y. Free-energy model for the inhomogeneous hard-sphere fluid mixture and density-functional theory of freezing. *Physical Review Letters.* 1989;63(9):980-983.

52. Roland R. Fundamental measure theory for hard-sphere mixtures: a review. *Journal of Physics: Condensed Matter.* 2010;22(6):063102.

53. Tarazona P, Evans R. A simple density functional theory for inhomogeneous liquids. *Molecular Physics.* 1984/07/01 1984;52(4):847-857.

54. Carnahan NF, Starling KE. Equation of State for Nonattracting Rigid Spheres. *The Journal of Chemical Physics.* 1969;51(2):635-636.

55. Tang Y, Tong Z, Lu BCY. Analytical equation of state based on the Ornstein-Zernike equation. *Fluid Phase Equilibria.* 1997;134(1–2):21-42.

56. Tang Y. On the first-order mean spherical approximation. *The Journal of Chemical Physics.* 2003;118(9):4140-4148.

57. Hager W, Zhang H. A New Conjugate Gradient Method with Guaranteed Descent and an Efficient Line Search. *SIAM Journal on Optimization.* 2005;16(1):170-192.

58. Yang RT. *Gas separation by adsorption processes*. Singapore ; River Edge, N.J.: World Scientific; 1997.

59. Duong DD. *Adsorption analysis : equilibria and kinetics*. London: Imperial College Press; 1998.

60. Myers AL, Prausnitz JM. Thermodynamics of mixed-gas adsorption. *AIChE Journal.* 1965;11(1):121-127.

61. Myers AL, Monson PA. Physical adsorption of gases: the case for absolute adsorption as the basis for thermodynamic analysis. *Adsorption.* Apr 2014;20(4):591-622.

62. Snurr RQ. New Horizons for the Physical Chemistry of Nanoporous Materials. *J Phys Chem Lett.* Jul 21 2011;2(14):1842-1843.

63. Ockwig NW, Delgado-Friedrichs O, O'Keeffe M, Yaghi OM. Reticular chemistry: Occurrence and taxonomy of nets and grammar for the design of frameworks. *Accounts Chem Res.* Mar 2005;38(3):176-182.

64. Keskin S, Liu J, Rankin RB, Johnson JK, Sholl DS. Progress, Opportunities, and Challenges for Applying Atomically Detailed Modeling to Molecular Adsorption and Transport in Metal-Organic Framework Materials. *Ind Eng Chem Res.* Mar 4 2009;48(5):2355-2371.

65. Jiang JW, Babarao R, Hu ZQ. Molecular simulations for energy, environmental and pharmaceutical applications of nanoporous materials: from zeolites, metal-organic frameworks to protein crystals. *Chem Soc Rev.* 2011;40(7):3599-3612.

66. Yang QY, Liu DH, Zhong CL, Li JR. Development of Computational Methodologies for Metal-Organic Frameworks and Their Application in Gas Separations. *Chem Rev.* Oct 2013;113(10):8261-8323.

67. Getman RB, Bae YS, Wilmer CE, Snurr RQ. Review and Analysis of Molecular Simulations of Methane, Hydrogen, and Acetylene Storage in Metal-Organic Frameworks. *Chem Rev.* Feb 2012;112(2):703-723.

68. Wilmer CE, Leaf M, Lee CY, et al. Large-scale screening of hypothetical metal-organic frameworks. *Nat Chem.* Feb 2012;4(2):83-89.

69. Colon YJ, Snurr RQ. High-throughput computational screening of metal-organic frameworks. *Chem Soc Rev.* Aug 21 2014;43(16):5735-5749.

70. Wu D, Wang CC, Liu B, Liu DH, Yang QY, Zhong CL. Large-scale computational screening of metal-organic frameworks for CH4/H2 separation. *Aiche J.* Jul 2012;58(7):2078-2084.

71. Sun WZ, Lin LC, Peng X, Smit B. Computational screening of porous metal-organic frameworks and zeolites for the removal of SO2 and NOx from flue gases. *Aiche J.* Jun 2014;60(6):2314-2323.

72. Tadmor EB, Miller RE. *Modeling materials: continuum, atomistic, and multiscale techniques*. Cambridge ; New York: Cambridge University Press; 2011.

73. Hohenberg P, Kohn W. Inhomogeneous Electron Gas. *Phys Rev B.* 1964;136(3B):B864-B871.

74. Evans R. Nature of the Liquid-Vapor Interface and Other Topics in the Statistical-Mechanics of Nonuniform, Classical Fluids. *Adv Phys.* 1979;28(2):143-200.

75. Parr RG, Yang W. *Density-functional theory of atoms and molecules*. New York: Oxford University Press 1989.

76. Wu JZ. Density functional theory for chemical engineering: From capillarity to soft materials. *Aiche J.* Mar 2006;52(3):1169-1193.

77. Lastoskie C, Gubbins KE, Quirke N. Pore size distribution analysis of microporous carbons: a density functional theory approach. *The Journal of Physical Chemistry.* 1993/05/01 1993;97(18):4786-4796.

78. Jia Fu YL, and Jianzhong Wu. Molecular density functional theory for multiscale modeling of hydration free energy. *Chemical Engineering Science.* 2014;accepted.

79. Jia Fu YL, Yun Tian and Jianzhong Wu. Density functional methods for fast screening of metal-organic frameworks for hydrogen storage. *Journal of Physical Chemistry C.* 2014;DOI: 10.1021/jp505963m.

80. Tang YP, Wu JZ. Modeling inhomogeneous van der Waals fluids using an analytical direct correlation function. *Phys Rev E.* Jul 2004;70(1):011201.

81. Ravikovitch PI, Neimark AV. Density functional theory model of adsorption on amorphous and microporous silica materials. *Langmuir.* 2006 Dec 19 2006;22(26):11171-11179.

82. Yu Y-X. A novel weighted density functional theory for adsorption, fluid-solid interfacial tension, and disjoining properties of simple liquid films on planar solid surfaces. *Journal of Chemical Physics.* Jul 14 2009;131(2):024704.

83. Liu Y, Liu HL, Hu Y, Jiang JW. Development of a Density Functional Theory in Three-Dimensional Nanoconfined Space: H2 Storage in Metal Organic Frameworks. *J. Phys. Chem. B.* 2009;113(36):12326-12331.

84. Yu Y-X, Wu J. Structures of hard-sphere fluids from a modified fundamental-measure theory. *J. Chem. Phys.* 2002;117(22):10156-10164.

85. Martin MG, Siepmann JI. Transferable Potentials for Phase Equilibria. 1. United-Atom Description of n-Alkanes. *The Journal of Physical Chemistry B.* 1998/04/01 1998;102(14):2569-2577.

86. Rappe AK, Casewit CJ, Colwell KS, Goddard WA, Skiff WM. Uff, a Full Periodic-Table Force-Field for Molecular Mechanics and Molecular-Dynamics Simulations. *J Am Chem Soc.* Dec 2 1992;114(25):10024-10035.

87. Wu J. Density functional theory for liquid structure and thermodynamics In: Lu X, Hu Y, Chen H, eds. *Molecular thermodynamics of complex systems*. Berlin: Springer; 2009:1-74

88. Johnson JK, John AZ, Keith EGD-LD. The Lennard-Jones equation of state revisited. *Mol. Phys.* 1992;78(3):591-618.

89. Tang YP, Wu JZ. A density-functional theory for bulk and inhomogeneous Lennard-Jones fluids from the energy route. *Journal of Chemical Physics.* Oct 8 2003;119(14):7388-7397.

90. He P, Liu H, Zhu J, et al. Tests of excess entropy scaling laws for diffusion of methane in silica nanopores. *Chemical Physics Letters.* May 11 2012;535:84-90.

91. Rosenfeld Y. RELATION BETWEEN TRANSPORT-COEFFICIENTS AND INTERNAL ENTROPY OF SIMPLE SYSTEMS. *Physical Review A.* 1977 1977;15(6):2545-2549.

92. Chui SSY, Lo SMF, Charmant JPH, Orpen AG, Williams ID. A chemically functionalizable nanoporous material [Cu3 (TMA) 2 (H2O) 3] n. *Science.* 1999;283(5405):1148-1150.

93. Addicoat MA, Coupry DE, Heine T. AuToGraFS: Automatic Topological Generator for Framework Structures. *J Phys Chem A.* Oct 9 2014;118(40):9607-9614.

94. Methane Opportunities for Vehicular Energy. http://arpa-e.energy.gov/?q=arpa-e-programs/move.

95. Walton KS, Snurr RQ. Applicability of the BET Method for Determining Surface Areas of Microporous Metal−Organic Frameworks. *J Am Chem Soc.* 2007/07/01 2007;129(27):8552-8556.

96. Sarkisov L, Harrison A. Computational structure characterisation tools in application to ordered and disordered porous materials. *Molecular Simulation.* 2011/12/01 2011;37(15):1248-1257.

Chapter 3. A Comprehensive Analysis of BET Surface Area for Microporous Materials

Abstract

Brunauer-Emmett-Teller (BET) method has been extensively used to characterize the surface areas of porous materials by semi-empirical fitting of gas-adsorption isotherms. Recent advances in materials synthesis question the exact meaning of the BET surface area and its applicability to a wide variety of microporous materials with the pore structure precisely defined at the atomic scales. There has been much debate in the recent literature on whether the BET surface area provides a faithful representation of the geometrical area if the pore structure is exactly known and whether the BET area is practically meaningful beyond the adsorption model. In this work, we provide a comprehensive analysis of the BET surface areas for both model and realistic microporous materials using the grand canonical Monte Carlo simulation for the adsorption of nitrogen gas at 77 K. Extensive simulation data for over 1000 materials indicate that the BET and geometrical surface areas are in general of the same order of magnitude but the standard BET method yields little information on the geometrical accessible surface areas.

Introduction

Porous materials are used in extensive chemical reaction and separation processes. The practical performance a porous material is often tied up with the internal surface areas per unit weight or volume, which is conventionally measured by gas adsorptions. The initial idea of "surface area measurements" stems from Langmuir's pioneering work for a comprehensive description of monolayer adsorption[97,98]. The Langmuir adsorption isotherm was later extended by Brunauer Emmett, and Teller by considering more realistic multilayer adsorption of gas molecules at the surface[99,100]. Nowadays BET adsorption isotherms have been routinely used for determining the specific surface areas of both amorphous and crystalline porous materials such as activated carbons and metal organic frameworks (MOFs). While the true geometrical area of an amorphous porous material is hardly known, the atomic structure of a crystalline material is experimentally accessible, opening an independent verification of the BET surface area. Although the BET method remains a popular choice to assess the surface area of new materials[101,102], it has been widely speculated that it does not provide a true measure of the geometrical area other than a relative adsorptive property to compare different materials[101,103,104]. The applicability of the BET method to micro- or sub-micro porosity characterization is even more controversial because it involves more complicated adsorption mechanism related to micropore filing effects[101,105-107]. As the BET method assumes uniform adsorption of gas molecules on a flat surface without lateral interactions, it works best for adsorbents with macropore or large mesopores[107,108]. For microporous materials (pore size < 2 nm), recent experimental and computational investigations revealed that the BET analysis provides

only an apparent "surface area" occupied by the adsorbate molecules on the strongest adsorption sites instead of the true geometrically accessible area[103,104,109]. For the recently synthesized MOFs or mixed zeolites with complicated multimodal pore structure with extremely high surface areas, the N_2 adsorption isotherms at 77K exhibit stepwise behavior, suggesting that the BET method may fail to perform a linear fitting in any pressure region[103,110,111]. The pressure range suitable for the linear fitting of the BET method is even more controversial due to the fact that the degree of linearity does not validate any hypothesis of the BET surface area itself[102,104]. In order to aid the selection of pressure range, the BET consistency criterion has been recommended to check the validity of the BET method[105,106]. By investigating a set of experimentally synthesized MOF materials, Snurr and coworkers indicated that the BET surface area does not necessarily agree with the geometrical surface area even when the consistency criterion is fulfilled[109]. However, the conclusion is contradictory with their earlier publications that show good agreement between the BET and geometric surface areas[29,95]. From a fundamental perspective, the BET method is essentially an empirical procedure that is dependent not only on the theoretical assumptions but also on empirical parameters such as the cross-section area (a^2) of adsorbed gas molecules. Even for nitrogen adsorption, the molecular parameter might be altered with different surface structures and interactions[108,112-115].

The purpose of this work is, by extensive Monte Carlos simulations, to provide a comprehensive understanding of the relation between the BET and geometric surface areas for both the conventional models of amorphous porous materials and for crystalline open framework materials. We firstly apply the BET model to slit pore systems where the

geometrical surface area is defined without ambiguity. By systematically adjusting the surface interaction strength and the pore size of a slit pore, we show that the lattice size (a) occupied by each nitrogen molecule is not fixed, which may result in inconsistent BET and geometrical surface areas. To assess the surface area of open framework materials, we select 1200 representative hypothetical MOF structures from an online database prepared by Snurr and coworkers[15]. The database includes top 300 MOF materials with the largest surface area, top 300 with the largest void fraction, top 300 with the largest volumetric adsorption capacity, and top 300 materials with the largest weight adsorption capacity. The ranking criteria are based methane adsorption, which is consistent with our previous work for material screening[116]. The diversity of these materials renders an excellent benchmark for the comprehensive examination of the BET method for characterization of the surface areas of adsorbents with a wide range of porosity, topology and guest-host interactions. Unlike non-ordered porous materials, the geometrical area of MOFs can be independently calculated by rolling the specific probe (mostly N_2) over the atoms of the crystal structure of interest[28-30]. The geometric surface area measured with the N_2 probe is usually named as the nitrogen accessible surface area (NASA), which can be used as a contrast to non-ordered porous materials. NASA can also be used to determine ideal textural parameters from the crystalline structure and compare with the standard BET surface areas. With the nitrogen adsorption isotherms at 77K generated by the grand canonical Monte Carlo (GCMC) simulations, we can apply the BET method to determine the BET surface areas for all the materials considered in this work and compare the results with the corresponding NASAs defined with different N_2 probe sizes that are commonly used in the

literature[29,48,96]. We find that the BET analysis of the surface area is highly sensitive to the pore size, structure heterogeneity, and adsorbate-adsorbent interactions. Importantly, there is no simple correlation of the BET surface areas with NASAs.

Methods

Nitrogen accessible surface area (NASA)

We calculate NASA for each crystalline material based on the method introduced by Walton et al.[95]. The geometric area is determined from the loci of a probe particle that is randomly placed at a predefined distance d from individual atoms of the adsorbent without overlapping with other atoms. The surface area for the ith atom is

$$s_i = f_i \times \pi \times d_i^2 \tag{45}$$

where f_i is the fraction of randomly generated locations where the probe particle does not overlap with atoms of the framework material. The total accessible surface area of the material can be ready calculated by adding up the surface areas of all the framework atoms,

$$S_{NASA} = \sum_{i=1}^{n} s_i \tag{46}$$

Apparently, the procedure depend on parameter d for each atom. In this work, we will assess the geometric surface area using the Lennard-Jones (LJ) diameter d_{LJ}, the van der Waals diameter d_{vdw}, and the Barker-Henderson diameter d_{BH}. The LJ diameter is defined as

$$d_{LJ} = (\sigma_{ff} + \sigma_{ss})/2 \tag{47}$$

where σ_{ff} and σ_{ss} are the LJ diameters for the probe molecule (N_2) and an atom of the adsorbent material. The van der Waals diameter corresponds to the separation between two atoms where the LJ potential exhibits a minimum:

$$d_{vdw} = \sqrt[6]{2} d_{LJ} \tag{48}$$

According to previous investigations[29,96], the van der Waals diameter provides the best estimation of the pore sizes and projection areas of adsorbate[117], provided that the interaction between the atoms from the material and the probe molecule can be described as the LJ potential.

In addition to the two definitions probing distance commonly adopted in the literatures[28,118], we also calculate the geometric area using the Barker-Henderson diameter d_{BH}, which depends on temperature and the LJ diameter[48]

$$\frac{d_{BH}}{d_{LJ}} = \frac{1 + 0.2977T^*}{1 + 0.33163T^* + 0.0010477T^{*2}} \tag{49}$$

where T^* is the reduced temperature defined as $T^* = k_B T / \epsilon$, k_B is the Boltzmann constant, and $\epsilon = \sqrt{\epsilon_{ff}\epsilon_{ss}}$ is the LJ energy parameter for the probe interaction with individual atoms of the absorbent.

Brunauer-Emmett-Teller (BET) Surface Area

We calculate the BET surface area for each material based on the linear fitting of the adsorption isotherm for nitrogen gas at 77 K[99]:

$$\frac{P/P_0}{n(1-P/P_0)} = \frac{1}{n_m k_0} + \frac{k_0 - 1}{n_m k_0}\left(\frac{P}{P_0}\right) \tag{50}$$

where n is the adsorption amount. For both slit pore and MOFs we used the total amount of gas molecules in the system, which has negligible difference with excess adsorption amount at this subcritical condition. P is the gas pressure in the bulk, P_0 is the saturation pressure (1 atm for nitrogen at 77 K), k_0 is a parameter proportional to the exponential of the surafec adsorption energy, and n_m is the effective monolayer capacity defined by the BET model. Both n_m and k_0 can be extracted from the linear regression of the nitrogen adsorption isotherm with Eq.(50). In particular, parameter n_m is directly related with the BET surface area, which is calculated by assuming that the pore surface is completely covered with the gas molecules

$$S_{BET} = n_m \cdot a^2 \tag{51}$$

where a^2 is the cross-sectional area of each nitrogen molecule in the monolayer. It is taken as 0.162 nm^2 by convention, assuming that the monolayer density is the same as that of bulk liquid[102]. In other words, the average lattice size a is empirically set as 0.4 nm in the BET method.

Because the BET model is not universally applicable to all adsorption isotherms, we use the following two consistency criteria as proposed by Rouquerol et al.[102,119] to ensure that the BET fitting is in the reasonable pressure region:

a. k_0 should be positive since it represents the exponential of the adsorption energy in the BET model;
b. the pressure range should be limited to the region where $n(1-P/P_0)$ increases with P/P_0.

Two additional criteria were proposed in Rouquerol's original work, which were problematic to implement as indicated by Gómez-Gualdrón et al.[109]. It has been long recognized that the BET surface area is highly sensitive to the range of pressure selected for fitting the adsorption isotherm and to the size of the probe molecule used to determine the surface area. Among numerous attempts to settle down this problem, the BET consistency criteria has been widely accepted to check the validity of the BET method. However, as discussed by recent publications, the satisfaction of the four consistency criteria is still not sufficient to validate BET area as a true measurement of surface area of the material.

Grand canonical Monte Carlo (GCMC) simulations

In this work, all adsorption isotherms used in the BET fitting were obtained from GCMC simulations. To obtain N_2 adsorption isotherms at 77 K for both model slit pores and MOFs, we carried out standard GCMC simulations using the Towhee program[120]. We used the united atom model for the gas molecules (N_2) and the rigid molecular model for the nanoporous materials. The LJ potential is used to describe all atomic pair interactions. The cross LJ parameters are given by the Lorentz-Berthelot combination rule. For crystalline materials, the MC simulations were performed on 2x2x2 unit cells of adsorbents under the three dimensional periodic boundary conditions. Similar numbers of gas molecules were simulated for the slit-pore models (ok. The van der Waals interactions were evaluated using 12.9 Å cutoff in shifted potential style. Each GCMC simulation run includes 10^6 moves for equilibration and another 10^6 moves for data collection. MC moves include molecular insertions, deletions, and translations of the gas molecules. Chemical

potentials used in the simulations were calculated from the MBWR equation of state[41]. The structures of the MOFs are from the crystalline information files (CIFs)[7,10,11,13,15,39,40,121]. Carbon slit pore model is represented by the Steele wall 10-4-3 potential, which is commonly used in experimental characterization of amorphous materials such as activated carbons[19,20].

The same model parameters were used in both BET surface area and NASA determinations. Specifically, we used the universal force field (UFF) for all the framework atoms of the adsorbent materials[38]. For both adsorption isotherm and NASA calculations, N_2 molecules are described as a 1-site LJ core with diameter $\sigma_{ff} = 3.572$ Å and energy $\varepsilon_{ff} = 93.98K$. The same parameters were used in our earlier publication[122]. It is worth noting that simulation of N_2 77 K adsorption is typically based on the 3-sites all atom model for N_2 molecules[123]. We found that the united atom model agrees well with the all atom model for describing the isotherms at conditions of interest in this work. Similar conclusions were made by Do et al[113]. One major advantage of the 1-site model is that it speeds up the calculations by at least one order of magnitude in comparison with the all atom model for N_2.

Results and Discussions

In the following we compare systematically the BET surface area with NASA for both amorphous and crystalline porous materials. The slit pores are used to represent amorphous materials as conventional used in the literature. In addition to comparing the BET and the geometrical surface areas, the model system allows us to examine the effects of pore size and surface energy on the empirical parameters used in the BET model and

helps understand how and why the BET method fails under certain thermodynamic conditions. For crystalline porous materials, we first consider a set of experimentally synthesized MOFs and zeolites, which includes IRMOFs discussed in an earlier publication by Walton el al.[95]. A similar procedure is extended to examine a larger database including 1200 hypothetical MOFs within 4 representative categories.

Figure 2 (A) shows the adsorption isotherms for nitrogen gas in slit pores with the pore width ranging from that for a nanopore ($H/\sigma = 2.5$), a micropore ($H/\sigma = 5$), to that for two mesopores ($H/s = 10, 20$), where $s = 3.572$ Å represents the LJ diameter for each nitrogen molecule. As well documented, the adsorption isotherms are quite different for nano, micro and meso pores. For a nanopore ($H/\sigma = 2.5$), the surface excess increases monotonically with the bulk pressure. The adsorption isotherm deviates from the Langmuir-like behavior because of strong intermolecular correlations. When the pore size increases, the adsorption isotherm exhibits several inflection points due to layering transitions inside the slit pore, accompanied by noticeable hysteresis between adsorption and desorption isotherms. When the pore size is sufficiently large such that the gas molecules near two parallel surfaces are not correlated, the adsorption isotherms become independent of the pore size (e.g., approximately the same for H/σ = 10 and 20 as shown in panel A). Nitrogen adsorption in a single surface resemble typical type II isotherms according to the IUPAC classification[105].

Figure 2 (B) presents the BET fitting for the four adsorption isotherms. Clearly, the range of pressure where the BET linearity holds is different for different pores. For the smallest pore ($H/\sigma = 2.5$), the BET method is applicable only to the low pressure region

due to fact that the BET model ignores intermolecular interaction between gas molecules, which is strong even at low pressure for small pore as shown on panel (A), where we can see the inflection point (corresponding to point B in BET theory which is the monolayer capacity n_m)[102] in the isotherm curve is reached at much smaller pressure for $H/\sigma = 2.5$ compared to other three pore widths. Also due to the same point B shared by the three other pore widths, they have the same BET fitting results as shown on panel (B), where the 3 lines collapse together. With the BET surface area obtained from panel (B) we compared its ratio to the geometrical for different pore widths and surface interactions in Panel (C), where we can see that for larger pores, the BET surface areas are more consistent with geometrical areas, though BET method tends to give a systematic larger surface area with increasing surface interactions. However, for small pores the BET method underestimates the surface area regardless of the surface interaction energy. For slit pores with stronger surface interaction ($\varepsilon_{sf}/\varepsilon_{ff} = 0.70$), this effect might be cancelled by the systematic larger BET area with increasing surface energy. For smaller pore with relative weaker interaction, the BET method significantly underestimates the surface area as shown in panel C for the case $\varepsilon_{sf}/\varepsilon_{ff} = 0.40$ and $H/\sigma = 2.5$.

Figure 3 shows the N_2 lattice size parameter (a) and the energy parameter ($\ln k_0$) used in the BET model obtained from linear fitting of the adsorption isotherms for different slit pores. Panel (A) shows that the lattice size is between 0.38 to 0.42 nm for N_2 molecule relatively insensitive to the pore size and the surface energy. While these values are within the conventional range used to apply the BET method, the lattice size is much larger than 0.4 nm for smaller pores. The larger lattice size for nanopores is consistent with what we

see from Figure 2. If the same lattice size for nitrogen is adopted for applying BET method to calculate the surface area, the smaller pores tend to underestimate the geometric surface area. Figure 2B shows that the adsorption energy decreases with increasing the pore width, and becomes constant when the pore size is sufficiently large (when the two surfaces are not correlated). The BET energy parameter becomes larger for pores with stronger surface energy (larger $\varepsilon_{sf} / \varepsilon_{ff}$) as shown in the inset of panel (B).

Figure 4 compares the BET surface areas with two different definitions of NASA for 12 experimentally synthesized porous materials. Here the 6 IRMOFs were previously discussed by Walton et al.[95] who concluded that the BET method provided a good representation of the geometric surface areas. Overall, the BET surface area is consistent with NASA calculated with the van der Waals diameter ($NASA_2$), even though we see noticeable overestimation of the surface area except for IRMOF-14. For comparison, Figure 4 also includes the geometric area ($NASA_1$) calculated with LJ diameters. In that case, the BET method severely overestimates the surface areas of all the materials. The difference between $NASA_1$ and $NASA_2$ arises from the systematic larger probe size selected to calculate the geometrical area using the van der Waals diameters than that based on the LJ diameters. Within these limited number of materials selected, it appears that the BET method provides a reasonable estimation of the geometric surface areas for porous materials with complex structures and diverse surface interactions. As indicated in an earlier theoretical study by Gelb and Gubbins[107], the BET method tends to systematically overestimate the surface areas of porous systems with highly confined structure and complex surface curvature.

Figure 5 compare the BET and geometric surface areas for a large library of MOFs including 1200 diverse geometrical structures and surface interactions. In addition to the LJ and van der Waals diameters commonly used for definitions of NASAs as shown in panel (A) and (B), we added in panel (C) to show how the BET surface area correlates with the geometrical area defined by the Barker-Henderson (hard-sphere) diameter. Overall, the correlation of the BET area with the hard-sphere defined geometrical surface area ($NASA_3$) is consistent with geometrical surface area calculated with pure LJ diameters ($NASA_1$). In both cases, the BET method systematically overestimates the surface area especially for the materials ranked according to void, weight and volumetric categories. By contrast, the van der Waals diameter ($NASA_2$) gives a much better agreement with the BET surface area. Even though the BET surface area correlates better with $NASA_2$ than the other two, it still shows a large scattering of data in the MOFs ranked according to the volumetric and surface categories. In all cases, the BET surface area is not a proper characterization for the true geometrical surface areas of materials with complex structures and surface interactions, in particular for materials with small the specific surface areas.

Recent experiments indicate that the BET surface area provides a poor representation of the geometric area also for materials with multimodal pore size distributions[103,104]. To illustrate the effect of pore size distribution, we consider also a mixed pore model for amorphous material. In figure 6, we consider 3 combinations of different pore sizes with the same surface interaction $\varepsilon_{sf} / \varepsilon_{ff} = 0.55$ that approximately mimics carbon graphite materials. For mixed-pore systems containing a nanopore ($H / \sigma = 2.5$) as shown in panel (A) and (B), the BET fitting results are very sensitive to

the mixing fraction f. For systems containing only large pores as shown in panel (C), however, the BET fitting results are independent of the mixing fractions. As summarized in panel (D), the BET method tends to give a systematic larger surface area for system mixed only with larger pores ($H/\sigma = 5,10$), though it is not affected by the pore size distribution of the system. However, for the systems including nanopores (e.g., $H/\sigma = 2.5$), the BET surface area highly depends on the pore size distribution of the system. As the fraction of small pores increases, we see more deviation of BET surface area from true geometrical surface area. This effect can be further verified from Figure 5 for materials in the surface category. Because most materials in this category have a high fraction of nanopores, the underestimation of surface area by the BET method is more obvious than the other three cases shown in Figure 5.

Conclusions

In this work, we provide a systematic and comprehensive analysis of the BET method for estimation of the surface areas of porous materials. GCMC simulation was used to calculate nitrogen adsorption at 77K for both model amorphous and crystalline materials. By comparing the BET surface area with geometric surface areas for over 1000 materials with complex structures and heterogeneous interactions, we find that the performance of BET analysis on surface area characterization is sensitive to the pore size, the structure heterogeneity as well as adsorbate-adsorbent interaction. For materials with small specific surface area, the BET surface area and NASAs are totally uncorrelated. Nevertheless, a positive correlation can be identified if the geometric surface area is defined according to the van der Waals diameter.

Figure 3-1. (A) Schematic illustration of BET model; (B) Slit-pore model for amorphous porous materials. (C) A representative framework material (MOF-5).

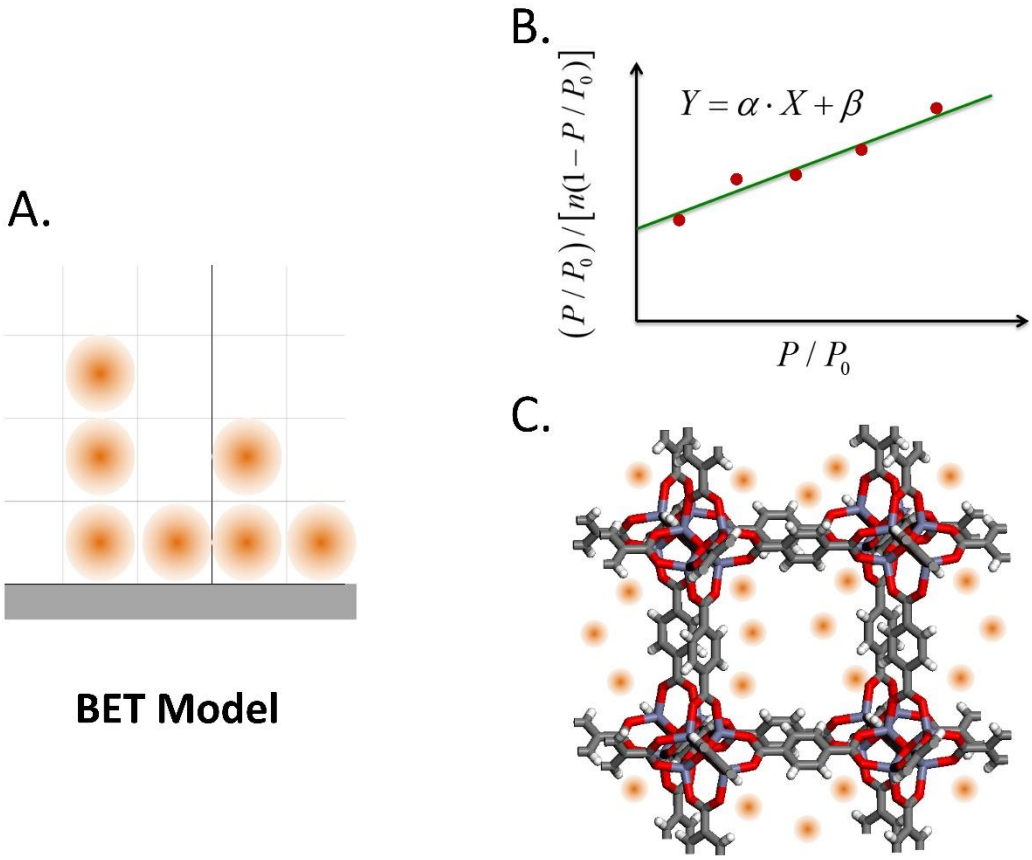

Figure 3-2. (A) The gas adsorption amount predicted from GCMC simulations for N_2 adsorption at 77K in slit pores of different pore widths; (B) The BET fitting of the adsoprion isotherms; (C) The ratio of the BET surface area with respect to the geometrical surface area of the model slit pores with different widths and surface energies. In panels A and B, the reduced surface energy is $\varepsilon_{sf}^{*} \equiv \varepsilon_{sf} / \varepsilon_{N_2}$ =0.55, where ε_{N_2} stands for the LJ energy parameter for nitrogen, H / σ is the reduced pore width. In panel (B), the symbols are from GCMC results, and all the dash lines are fitted results from BET method with different colors representing different reduced pore widths. The reduced surface potential 0.55 corresponds to the carbon graphite.

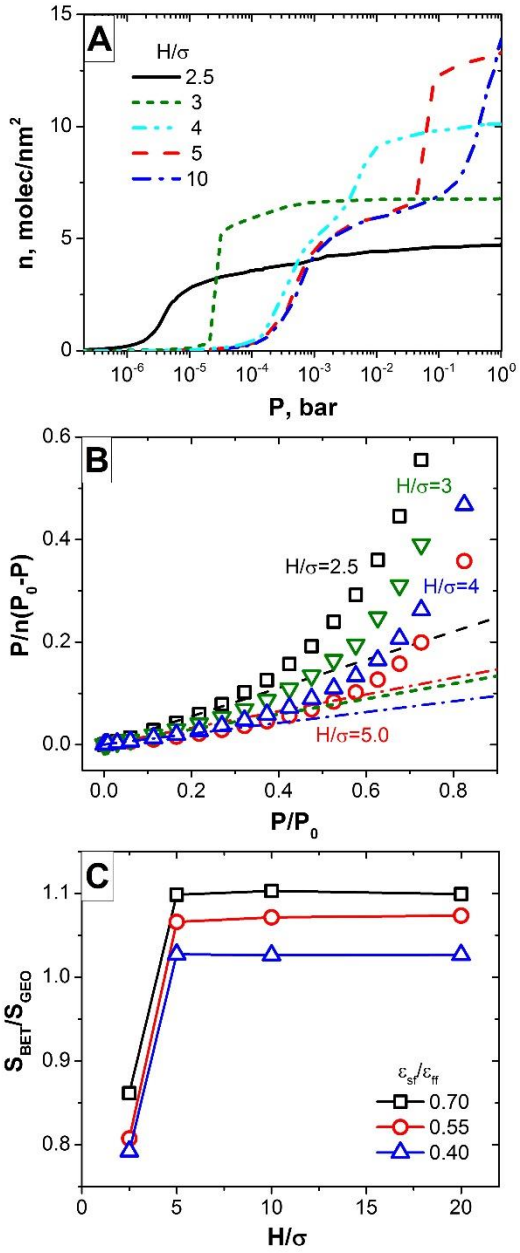
A
H/σ
2.5
3
4
5
10
n, molec/nm²
P, bar
B
H/σ=3
H/σ=2.5
H/σ=4
H/σ=5.0
P/n(P₀-P)
P/P₀
C
S_BET/S_GEO
H/σ
ε_sf/ε_ff
0.70
0.55
0.40

Figure 3-3 The effects of pore size and surface energy on the two BET model parameters: (A) the average lattice size (a)occupied by a single N_2 molecule and (B) a parameter related to the adsorption energy, $\ln(k_0)$. The inset shows how the adsorption energy changes with surface interation energy e^*_{sf} for slit pores different widths.

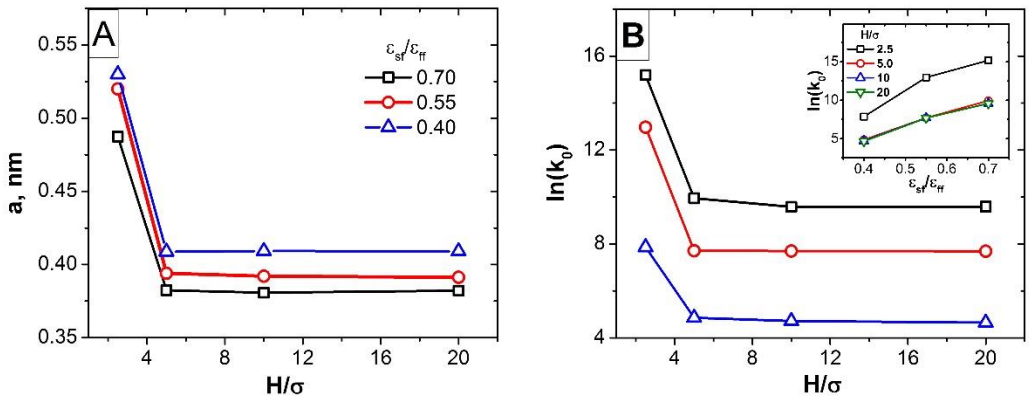

Figure 3-4 Comparison of the calculted BET surface area with two N_2 accessible surface areas (NASA) defined according to the Lennard-Jones (LJ) diameter d_{LJ} ($NASA_1$) and the van der Waals (vdw) diameter d_{vdw} ($NASA_2$), respectively.

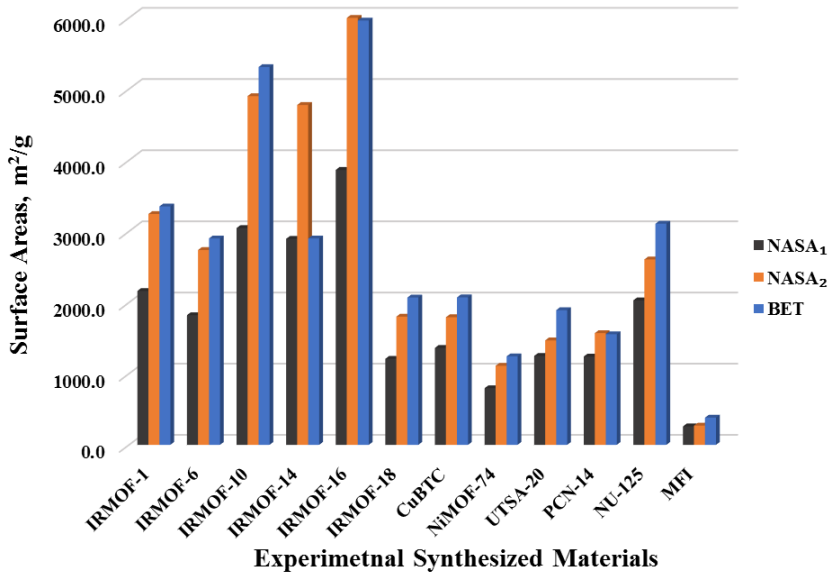

Figure 3-5 The BET surface areas calculated with consistency criteria for 1200 hypothetical MOFs compared with (A) $NASA_1$, (B) $NASA_2$ (C) $NASA_3$ calculated with the LJ dimater, the vdw diameter, and the Barker-Henderson (BH) diameter d_{BH}, respectively, for both the adsorbate and adsorbent atoms. The black square, red circle, black trangles and magenta trangles refer to the top 300 MOFs ranked in the void fraction, weight adsorption capacity, volumetric adsorption capacity, and surface area capacity in the database prepared by Snurr and coworkers.

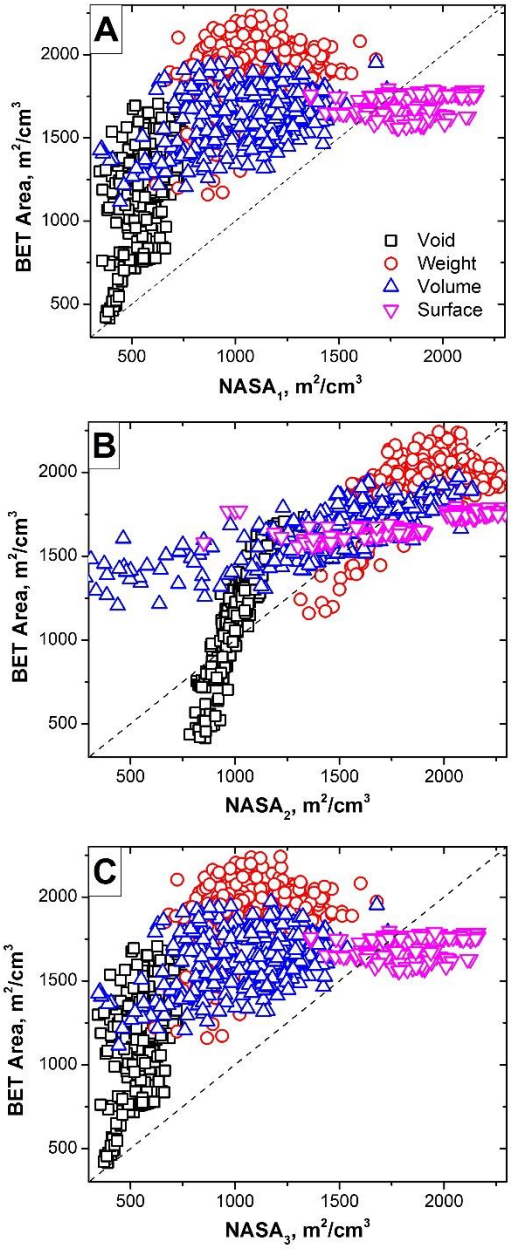

Figure 3-6 The BET fitting results for mixed slit pores of different widths (A) H/σ =2.5 and 5.0, (B) H/σ =2.5 and 10, (C) H/σ = 5.0 and 10, and the corresponding ratios of the BET surface areas with respect to the geometrical areas for different combinations of mixture and mixting fraction (D). For all the cases, f_1, f_2, f_3 and f stand for the fraction of the smaller pore in the mixture.

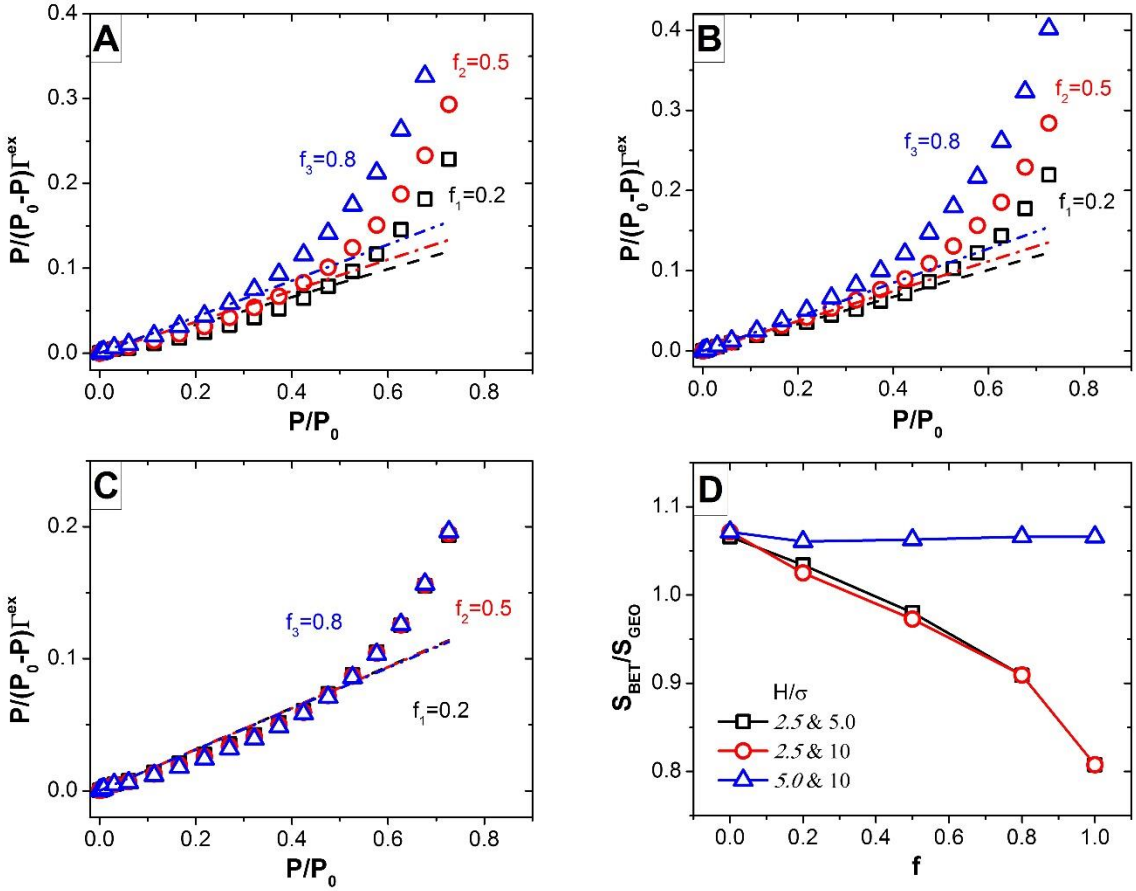

References:

1. Langmuir I. THE CONSTITUTION AND FUNDAMENTAL PROPERTIES OF SOLIDS AND LIQUIDS. PART I. SOLIDS. *Journal of the American Chemical Society.* 1916/11/01 1916;38(11):2221-2295.

2. Langmuir I. THE ADSORPTION OF GASES ON PLANE SURFACES OF GLASS, MICA AND PLATINUM. *Journal of the American Chemical Society.* 1918/09/01 1918;40(9):1361-1403.

3. Brunauer S, Emmett PH, Teller E. Adsorption of Gases in Multimolecular Layers. *Journal of the American Chemical Society.* 1938/02/01 1938;60(2):309-319.

4. Emmett PH, Brunauer S. The Use of Low Temperature van der Waals Adsorption Isotherms in Determining the Surface Area of Iron Synthetic Ammonia Catalysts. *Journal of the American Chemical Society.* 1937/08/01 1937;59(8):1553-1564.

5. Sing K. The use of nitrogen adsorption for the characterisation of porous materials. *Colloids and Surfaces A: Physicochemical and Engineering Aspects.* 2001;187–188:3-9.

6. Sing KSW. 7 - Assessment of Surface Area by Gas Adsorption. *Adsorption by Powders and Porous Solids (Second Edition)*. Oxford: Academic Press; 2014:237-268.

7. Yuan D, Getman RB, Wei Z, Snurr RQ, Zhou H-C. Stepwise adsorption in a mesoporous metal-organic framework: experimental and computational analysis. *Chemical Communications.* 2012;48(27):3297-3299.

8. Senkovska I, Kaskel S. Ultrahigh porosity in mesoporous MOFs: promises and limitations. *Chemical Communications.* 2014;50(54):7089-7098.

9. Sing KSW. Reporting physisorption data for gas/solid systems with special reference to the determination of surface area and porosity (Recommendations 1984). *Pure and Applied Chemistry.* Vol 571985:603.

10. Thommes M, Kaneko K, Neimark Alexander V, et al. Physisorption of gases, with special reference to the evaluation of surface area and pore size distribution (IUPAC Technical Report). *Pure and Applied Chemistry.* Vol 872015:1051.

11. Gelb LD, Gubbins KE. Characterization of Porous Glasses: Simulation Models, Adsorption Isotherms, and the Brunauer−Emmett−Teller Analysis Method. *Langmuir.* 1998/04/01 1998;14(8):2097-2111.

12. Sing KSW. Physisorption of gases by carbon blacks. *Carbon.* 1994/01/01 1994;32(7):1311-1317.

13. Gómez-Gualdrón DA, Moghadam PZ, Hupp JT, Farha OK, Snurr RQ. Application of Consistency Criteria To Calculate BET Areas of Micro- And Mesoporous Metal–Organic Frameworks. *Journal of the American Chemical Society.* 2016/01/13 2016;138(1):215-224.

14. Wang TC, Bury W, Gómez-Gualdrón DA, et al. Ultrahigh Surface Area Zirconium MOFs and Insights into the Applicability of the BET Theory. *Journal of the American Chemical Society.* 2015/03/18 2015;137(10):3585-3591.

15. Schneider P, Hudec P, Solcova O. Pore-volume and surface area in microporous–mesoporous solids. *Microporous and Mesoporous Materials.* 2008;115(3):491-496.

16. Bae Y-S, Yazaydın AÖ, Snurr RQ. Evaluation of the BET Method for Determining Surface Areas of MOFs and Zeolites that Contain Ultra-Micropores. *Langmuir.* 2010/04/20 2010;26(8):5475-5483.

17. Walton KS, Snurr RQ. Applicability of the BET Method for Determining Surface Areas of Microporous Metal−Organic Frameworks. *Journal of the American Chemical Society.* 2007/07/01 2007;129(27):8552-8556.

18. Engineering F, Conference, Myers AL, Belfort G, American Institute of Chemical E, Deutsche Vereinigung für Chemie- und V. Fundamentals of adsorption : proceedings of the Engineering Foundation conference held at Schloss Elmau, Bavaria, West Germany, May 6-11, 1983; 1984; New York.

19. Do DD, Do HD, Nicholson D. Effects of Surface Structure and Temperature on the Surface Mediation, Layer Concentration and Molecular Projection Area: Adsorption of Argon and Nitrogen onto Graphitized Thermal Carbon Black. *Adsorption Science & Technology.* 2007;25(6):347-363.

20. Trens P, Denoyel R, Glez JC. Comparative adsorption of argon and nitrogen for the characterisation of hydrophobized surfaces. *Colloids and Surfaces A: Physicochemical and Engineering Aspects.* 2004;245(1–3):93-98.

21. Do DD, Herrera L, Fan C, Wongkoblap A, Nicholson D. The role of accessibility in the characterization of porous solids and their adsorption properties. *Adsorption.* 2010;16(1):3-15.

22. Wilmer CE, Leaf M, Lee CY, et al. Large-scale screening of hypothetical metal–organic frameworks. *Nat Chem.* 2012;4(2):83-89.

23. Fu J, Tian Y, Wu J. Classical density functional theory for methane adsorption in metal-organic framework materials. *AIChE Journal.* 2015;61(9):3012-3021.

24. Düren T, Millange F, Férey G, Walton KS, Snurr RQ. Calculating Geometric Surface Areas as a Characterization Tool for Metal−Organic Frameworks. *The Journal of Physical Chemistry C.* 2007/10/01 2007;111(42):15350-15356.

25. Frost H, Düren T, Snurr RQ. Effects of Surface Area, Free Volume, and Heat of Adsorption on Hydrogen Uptake in Metal−Organic Frameworks. *The Journal of Physical Chemistry B.* 2006/05/01 2006;110(19):9565-9570.

26. Sarkisov L, Harrison A. Computational structure characterisation tools in application to ordered and disordered porous materials. *Molecular Simulation.* 2011/12/01 2011;37(15):1248-1257.

27. Cotterman RL, Schwarz BJ, Prausnitz JM. Molecular thermodynamics for fluids at low and high densities. Part I: Pure fluids containing small or large molecules. *AIChE Journal.* 1986;32(11):1787-1798.

28. Zagrafskaya RV, Karnaukhov AP, Fenelonov VB. Packing of molecules on solid surfaces in physical adsorption. *Reaction Kinetics and Catalysis Letters.* 1981;16(2):223-227.

29. Furukawa H, Ko N, Go YB, et al. Ultrahigh Porosity in Metal-Organic Frameworks. *Science.* 2010;329(5990):424-428.

30. Rouquerol J, Llewellyn P, Rouquerol F. Is the bet equation applicable to microporous adsorbents? In: P.L. Llewellyn FR-RJR, Seaton N, eds. *Studies in Surface Science and Catalysis.* Vol Volume 160: Elsevier; 2007:49-56.

31. Martin MG. MCCCS Towhee: a tool for Monte Carlo molecular simulation. *Molecular Simulation.* 2013/12/01 2013;39(14-15):1212-1222.

32. Johnson JK, Zollweg JA, Gubbins KE. The Lennard-Jones equation of state revisited. *Molecular Physics.* 1993/02/20 1993;78(3):591-618.

33. Eddaoudi M, Kim J, Rosi N, et al. Systematic Design of Pore Size and Functionality in Isoreticular MOFs and Their Application in Methane Storage. *Science.* 2002;295(5554):469-472.

34. Chui SS-Y, Lo SM-F, Charmant JPH, Orpen AG, Williams ID. A Chemically Functionalizable Nanoporous Material [Cu₃(TMA)₂(H₂O)₃]_n. *Science.* 1999;283(5405):1148-1150.

35. Ma S, Sun D, Simmons JM, Collier CD, Yuan D, Zhou H-C. Metal-Organic Framework from an Anthracene Derivative Containing Nanoscopic Cages Exhibiting High Methane Uptake. *Journal of the American Chemical Society.* 2008/01/01 2008;130(3):1012-1016.

36. Wu H, Zhou W, Yildirim T. High-Capacity Methane Storage in Metal−Organic Frameworks M2(dhtp): The Important Role of Open Metal Sites. *Journal of the American Chemical Society.* 2009/04/08 2009;131(13):4995-5000.

37. Guo Z, Wu H, Srinivas G, et al. A Metal–Organic Framework with Optimized Open Metal Sites and Pore Spaces for High Methane Storage at Room Temperature. *Angewandte Chemie International Edition.* 2011;50(14):3178-3181.

38. Wilmer CE, Farha OK, Yildirim T, et al. Gram-scale, high-yield synthesis of a robust metal-organic framework for storing methane and other gases. *Energy & Environmental Science.* 2013;6(4):1158-1163.

39. Baerlocher CM, L. B. Database of Zeolite Structures. 2001; http://www.iza-structure.org/databases/.

40. Balbuena PB, Gubbins KE. Theoretical interpretation of adsorption behavior of simple fluids in slit pores. *Langmuir.* 1993/07/01 1993;9(7):1801-1814.

41. Lastoskie C, Gubbins KE, Quirke N. Pore size heterogeneity and the carbon slit pore: a density functional theory model. *Langmuir.* 1993/10/01 1993;9(10):2693-2702.

42. Rappe AK, Casewit CJ, Colwell KS, Goddard WA, Skiff WM. UFF, a full periodic table force field for molecular mechanics and molecular dynamics simulations. *Journal of the American Chemical Society.* 1992/12/01 1992;114(25):10024-10035.

43. Tian Y, Wu J. Differential Heat of Adsorption and Isosteres. *Langmuir.* 2017/01/31 2017;33(4):996-1003.

44. Potoff JJ, Siepmann JI. Vapor–liquid equilibria of mixtures containing alkanes, carbon dioxide, and nitrogen. *AIChE Journal.* 2001;47(7):1676-1682.

Chapter 4. Differential Heat of Adsorption and Isosteres

Abstract

Heat of adsorption is a basic thermodynamic property extensively used not only for understanding thermal effects and heat management in industrial gas storage and separation processes but also for development and validation of adsorption models and materials force fields. Despite a long history of theoretical studies and a vast experimental literature, controversies often arise in the thermodynamic analysis of heat effects due to various assumptions used to describe gas adsorption and inconsistencies between direct calorimetric measurements and isosteric heat obtained from various adsorption isotherms. Here we present a rigorous theoretical procedure to predict isosteric heat without any assumption on the geometry of porous adsorbents or operating conditions. Quantitative relations between the differential heat and various isosteres have been established with the grand-canonical Monte Carlo simulation for gas adsorption in amorphous as well as crystalline porous materials. The inconsistencies and practical issues with conventional methods for the analysis of heat effect have been clarified in the context of the exact results for model systems. By resolving a number of controversies on heat analysis, the theoretical work is expected to have broad impacts on both the fundamentals and industrial applications of gas adsorption processes.

4.1. Introduction

Heat of adsorption is one of the most fundamental thermodynamic quantities to describe surface phenomena [31]. It is directly related to adsorbate-adsorbent interactions that are essential for assessment and screening of porous materials useful for gas storage and separation [32-34] and for thermal managements of industrial processes including various forms of pressure swing adsorption [35,36]. Because heat effects are generally more sensitive to the adsorbent-adsorbate interactions than adsorption isotherms [124], a combination of heat and isotherm measurements provides complementary information for understanding gas adsorption processes. In spite of its apparent importance, both experimental measurement and theoretical predictions of heat effects have been controversial; even the term "heat of adsorption" has been subject to a variety of interpretations and debates [61,125,126].

Two experimental procedures are commonly used to assess heat of adsorption [127]. One is through calorimetry measurement of the heat released during the adsorption process, and the other is by measuring adsorption isostere, i.e., a quantitative relation between pressure and temperature at a constant amount of the substance adsorbed (*viz*., the adsorbate) by a certain amount of the adsorbent. For practical applications, isostere measurements are more popular than calorimetry because direct detection of heat effects is often complicated and more expensive in particular at non-ambient conditions. Nevertheless, customized setups have been reported to combine volumetric (or gravimetric) isotherm experiments with calorimetry [125]. While the direct and indirect approaches are supposed to yield identical results, ambiguity often arises from different definitions of isostere and the adoption of different thermodynamic models to fit the adsorption

isotherms[127-130]. The experimental results for isosteric heat are sensitive to adsorption isotherms, particularly if the data are available only for a limited number of temperatures. Besides, the thermodynamic analysis of isostere measurements is typically based on numerical fitting of adsorption using semi-empirical models such as the single-site or dual-site Langmuir models[98,131], the Tóth model[132-134], or the virial equation[135-137]. Although the semi-empirical parameters can be correlated with the binding affinity between the adsorbate and adsorbent molecules[8], they are significant only within the context of specific isotherms. In addition, diverse models have been adopted to calculate the isosteric heat from adsorption isotherms[61]. These models differ not only in the definition of isostere but also in material characteristics such as pore volume and surface area[138,139]. The isostere analysis may lead to inconsistencies or even erroneous conclusions at highly non-ideal conditions[138,140].

Difficulties in dealing with the isosteric heat are mostly affiliated with the definition of the adsorbed phase, a concept introduced first in the pioneering works of J. W. Gibbs for the thermodynamics of heterogeneous systems. While the Gibbsian thermodynamics is convenient to describe surface properties, the interfacial region is depicted as a two-dimensional dividing surface without any volume. The isosteric heat is often interpreted as the energy to transfer an adsorbate molecule from the bulk to the adsorbed phase at some fixed thermodynamic conditions of the system such as constant temperature, pressure, and adsorbed amount. Unlike bulk systems, however, the properties of the adsorbed phase cannot be defined solely with the surface excess for each component. In particular, the Gibbsian formulism predicts an unphysical isosteric heat when the adsorption isotherm

exhibits a maximum[141]. To circumvent the divergent problem, T. L. Hills[142] proposed an alternative adsorption model by replacing the surface excess with absolute variables. Instead of using the Gibbsian formulism, the absolute adsorption model is focused on gas molecules in *the adsorbed region*[3,141]. For gas adsorption in porous materials, the adsorbed region is defined in terms of the difference between *the dead space* (i.e., the space in the cell accessible to gas molecules) and *the bulk region*[61]. The volume of the adsorbed region, also referred to as the pore volume, is typically calculated from nitrogen or argon adsorption at their respective normal boiling temperature. The volume of the dead space is calculated from helium adsorption at ambient temperature and pressure. It has been noted that the dead space could be larger than the geometrical volume of the system due to helium adsorption[143,144]. While the absolute adsorption model avoids the singularity of isosteric heat at high pressure, it is not applicable to adsorption in large pores except at low pressures[61].

In this work, we introduce a rigorous thermodynamic procedure for heat analysis that is free of inconsistency yet convenient for practical applications. The grand-canonical Monte Carlo simulation is used to demonstrate the relation between the differential heat and different isosteres for gas adsorption in amorphous and crystalline model porous materials. By avoiding problematic division between the bulk and adsorbed phases or semi-empirical estimation of the pore volume, the new theoretical procedure enables a faithful description of heat effects important for diverse applications of gas adsorption processes. The controversial issues with conventional isostere methods have also been clarified in the context of the exact results.

4.2. Theoretical Developments

To establish a rigorous thermodynamic procedure for heat of adsorption, we consider gas adsorption, as shown schematically in Fig. 1, that mimics a typical experimental setup for simultaneous measurement of adsorption heat and isotherm[145]. For simplicity, our discussion is focused on a pure gas but a similar procedure is applicable to mixtures. The *differential heat of adsorption*, designated as q_d, reflects the difference between the molar enthalpy of the gas in the bulk phase, H_b, and the differential internal energy, $(\P U / \P N)_{T,V}$,

$$q_d = H_b - (\P U / \P N)_{T,V} . \tag{52}$$

Eq.(52) follows the first law of thermodynamics for the sampling cell, a semi-open system that has a constant temperature, overall volume, and adsorbent amount. In other words, the differential heat reflects the heat released from the sampling cell upon adding an infinitesimal amount of the adsorbate at constant temperature, overall volume, and the adsorbent amount. The heat effect is measureable through differential calorimetry and depends on the thermodynamic conditions of the sampling cell including the adsorbent amount and bulk pressure (or equivalent, the chemical potential of the adsorbate). While the molar enthalpy depends on temperature *T* and pressure *P* of the bulk phase, $(\P U / \P N)_{T,V}$ represents the change in the internal energy of the entire cell in response to transferring dN moles of gas at fixed *T* and cell volume *V*. It should be noted that the change in the internal energy includes contributions from both adsorbent-adsorbate and

adsorbate-adsorbate interactions. The differential heat of adsorption can be directly measured with microcalorimetry[146] or calculated from Monte Carlo simulation using the ensemble fluctuation method[147].

Isostere heat is derived from a thermodynamic relation between the differential heat of adsorption and isotherms. By "isosteric" it is meant that the gas loading is treated as a constant. Because the adsorption cell has a fixed volume and the total amount of adsorbent, the differential internal energy is given by

$$dU = TdS + \mu dN \tag{53}$$

where S denotes the total entropy of sampling cell, and μ is the gas chemical potential. From Eq.(53), we have

$$\left(\frac{\partial U}{\partial N}\right)_{T,V} = T\left(\frac{\partial S}{\partial N}\right)_{T,V} + \mu = -T\left(\frac{\partial \mu}{\partial T}\right)_{N,V} + \mu = -T^2\left(\frac{\partial \mu / T}{\partial T}\right)_{N,V} \tag{54}$$

where the second equality follows the Maxwell relation $(\partial S / \partial N)_{T,V} = -(\partial \mu / \partial T)_{N,V}$. In practical applications, the chemical potential is often expressed in terms of gas fugacity, f,

$$\mu = \mu_0 + RT \ln f \tag{55}$$

where R stands for the gas constant, and μ_0 is the gas chemical potential at the reference state, i.e., the adsorbate as a pure ideal gas at the system temperature and unit pressure. Replacing the chemical potential in Eq.(54) with the gas fugacity leads to

$$\left(\frac{\partial U}{\partial N}\right)_{T,V} = H_0 + R\left(\frac{\partial \ln f}{\partial T}\right)_{N,V} \tag{56}$$

where H_0 is the gas molar enthalpy at the reference state. Combining of Eqs. (52) and (56) gives

$$q_d = \Delta H_b - RT^2 \left(\frac{\partial \ln f}{\partial T} \right)_{N,V} \equiv q_t \tag{57}$$

where $\Delta H_b \equiv H_b - H_0$ is the residual molar enthalpy of the bulk gas, and q_t is referred to as *the total isosteric heat*. Because Eq.(57) is derived from the fundamental equation of thermodynamics and the Maxwell relation, it is valid irrespective of the changes in the absorbent structure or phase transitions in the system (e.g., capillary condensation or wetting). As discussed below, q_t is different from the isosteric heat conventionally used in the literature.

According to Eq.(57), the differential heat of adsorption and the total isosteric heat are identical. It represents the difference between the residual molar enthalpy of the bulk gas and the residual "*partial molar enthalpy*" of the gas inside the sampling cell. We note that the total isosteric heat is not a true partial molar property because it is evaluated at a fixed cell volume and the total amounts of the adsorbate and the adsorbent in the cell. Strictly speaking, here the enthalpy cannot be defined in the conventional sense because the pressure of an inhomogeneous system is not a scalar variable. Nevertheless, like a partial molar property in bulk thermodynamics, the total isosteric heat depends on thermodynamic conditions of the entire cell including the cell size and the total amounts of gas and absorbent. Another point worth noting is that Eq.(57) is exact and immaterial to any specification of the adsorbent.

In adsorption measurements, the experimental results are conventionally reported in terms of isotherms, i.e., the surface excess as a function of the bulk gas pressure at different temperatures. The total gas amount inside the adsorption cell is typically not of a major concern because it depends on the system size [148,149]. In terms of the density profile of gas molecules inside the sampling cell, $\rho(\mathbf{r})$, the surface excess can be calculated from

$$\Gamma = \int d\mathbf{r}[\rho(\mathbf{r}) - \rho_b] \tag{58}$$

where ρ_b is the number density of the gas molecules in the bulk, and the integration extends to the entire cell volume. Whereas the total gas amount inside the cell depends on the system size, such dependence is less significant for the surface excess because the local density $\rho(\mathbf{r})$ reduces to ρ_b at macroscopic scales.

Conventionally, the isosteric heat, here designated as q_{ex} for its connection to the surface excess, is defined according to the Gibbsian adsorption formulism[31]

$$q_{ex} \equiv \Delta H_b - RT^2 \left(\frac{\partial \ln f}{\partial T} \right)_{\Gamma,V} \tag{59}$$

In the low-pressure limit, the gas fugacity can be replaced with the bulk pressure, and Eq.(59) reduces to the Clausius-Clapeyron equation[150]. Whereas *the excess isosteric heat* is often reported in the adsorption literature, it diverges when the surface excess versus pressure exhibits a maximum, i.e., when $(\partial\Gamma/\partial P)_T = 0$[138]. The singularity can be avoided by using the absolute formalism, which expresses the isosteric heat in terms of the absolute adsorption instead of the surface excess[61]

$$q_a \equiv \Delta H_b - RT^2 \left(\frac{\partial \ln f}{\partial T} \right)_{N_a, V} . \quad (60)$$

In this work, we refer to q_a as *the absolute isosteric heat* for convenience. In Eq.(60), the absolute adsorption amount is defined as

$$N_a \equiv \Gamma + \rho_b V_P \quad (61)$$

where V_p denotes the pore volume of the absorbent. The pore volume can be measured from nitrogen adsorption at 77 K or argon adsorption at 87 K near the atmospheric pressure[61]. At such conditions, the pore volume is assumed to be the same as the volume of liquid condensed inside the porous material. The latter is estimated from the gas adsorption amount at the saturation pressure and the corresponding liquid density.

4.3. Results and Discussions

The main difference between the total isosteric heat (q_t), the excess isosteric heat (q_{ex}), and the absolute isosteric heat (q_a) lies in what is fixed in evaluation of the partial derivative of the gas fugacity with respect to temperature. While such difference is innocuous at low pressure, the discrepancy becomes significant as pressure increases, which explains at least in part why controversies often arise when the heat effect is analyzed in terms of adsorption isotherms. To make quantitative comparisons, in the following we consider gas adsorption in slit pores and two representative framework materials. The slit-pore model is commonly used in experimental characterization of amorphous materials such as activated carbons[19,20]. In addition to validating the exact thermodynamic relations, this model allows us to illustrate the effects of pore size and

surface energy on the differential heat. For gas adsorption in crystalline porous materials, we consider silica zeolite with mordenite framework inverted (MFI) structure [121] and metal organic framework (MOF) Cu(hfipbb)(H_2hfipbb)$_{0.5}$ [151,152]. In both cases, we generate "experimental data" for the differential heat of adsorption, the adsorption amounts and the corresponding isosteric heat using the grand-canonical Monte Carlo simulations (GCMC)[20,85,153-155]. The MC simulations were typically performed on 2×2×2 unit cells of the adsorbents with 3-dimensional periodic boundary conditions. The van der Waals (VDW) interactions were evaluated using 12.9 Å cutoff in the shifted-potential style. Each GCMC simulation run consists of 10^6 MC moves for equilibration and another 5×10^6 moves for data collection. MC moves include insertions, deletions, and translations of the gas molecules. Chemical potentials used in the simulations were calculated using the MBWR equation of state. The data of each simulation trajectory was divided into 10000 blocks in order to perform the ensemble fluctuation calculation for isosteric heat of adsorption. All MC simulations were carried out using the Towhee program[120]. The force field parameters, along with the details of the materials structure and GCMC calculations, are given in Supporting Information (SI).

Figure 2 shows the total gas amount N, the absolute adsorbed amount N_a, and the surface excess Γ for the adsorption of krypton and hydrogen in a slit pore at 298 K over a broad range of pressure. Here the Steele 10-4-3 potential is used to describe interaction between a gas molecule and each surface of the slit pore with the parameters corresponding to those for typical activated carbons[153]. The two gases were selected because they provide representative adsorption behavior at supercritical conditions. Also shown in Fig 2 are the

differential heat of adsorption and the isosteric heat calculated according to Eqs.(57), (59) and (60), respectively.

As expected, the total, absolute, and excess adsorption amounts and their corresponding isosteric heat are quite different. For both hydrogen and krypton adsorption in the slit pore, the absolute adsorbed amount is always less than the total amount of gas inside the pore. The difference can be attributed to the fact that different gases are used to calculate the pore volume and the dead volume[61]. While both the total and absolute amounts increase monotonically with the gas pressure, the surface excess shows a maximum around 10 bar for krypton adsorption (Fig. 2B), leading to the divergence of the isosteric heat. Such a singularity has been discussed before by Salem[138], Myers[141] and others, and represents a major issue for the analysis of isosteric heat involving micropores. Interestingly, the absolute isosteric heat may also diverge at higher pressure. While the numerical issue with a maximum (or a minimum) in the excess isotherm has been well documented, less known is the divergence of the absolute isosteric heat, i.e., the isosteric heat derived from the absolute amount of adsorption. As shown in Fig. 2(A) and 2(C), the absolute amount of adsorption exhibits a maximum around 40 bar for krypton and, correspondingly, the absolute isosteric heat also goes to infinity. Because the molecular size for H_2 is much smaller than that for Kr and has weaker attraction energy, both the absolute amount and the surface excess rise monotonically with pressure. As a result, the isosteric heat has a finite value. However, both the excess and absolute models predict the isosteric heat much larger than the differential heat of adsorption predicted from the ensemble fluctuation method (Fig. 2D). By contrast, the latter agrees fully with the total

isosteric heat, confirming that Eq.(57) is the only thermodynamic consistent way to obtain the isosteric heat from adsorption isotherms.

Figure 3 presents Kr adsorption in nine slit pores with three representative surface potentials and three pore widths. The performance of different isosteric models varies drastically with the pore size and the surface energy. In all cases, the surface excess shows a maximum in the adsorption isotherm and, as a consequence, the excess isosteric heat diverges. For Kr adsorption in a 0.9 nm slit pore with a weakly attractive surface (e_{sf}^{*} =0.4), the absolute isosteric heat is significantly larger than the differential heat of adsorption, in particular as the gas pressure increases. As the surface attraction increases (ε_{sf}^{*}=0.7), the absolute isotherm also shows a maximum thus the absolute isosteric heat diverges at an intermediate pressure, similar to that obtained from the excess model. For a larger pore (1.8 nm) but with the same surface energy, the absolute adsorption model overestimates the differential heat of adsorption in the entire pressure range. As the surface energy increases, this discrepancy becomes less apparent in Henry's law region. However, the absolute isosteric heat deviates from the differential heat of adsorption at high pressure. For even a larger pore (3.6 nm), the discrepancy between absolute and total adsorption models becomes negligible. In this case, the absolute adsorption model may be justified to represent the total amount of gas molecules in the system.

The different trends in the isosteric heat of adsorption with increasing pressure can be explained in terms of different contributions from surface interaction, pore geometry and gas-gas interactions[19]. For the slit-pore model, the pore width is one of the most crucial factors in determining the overall trend of the isosteric heat. At low pressure, the heat of

adsorption arises primary from the adsorbate-adsorbent interactions, which increases with the gas pressure as more surface area is occupied. At high pressure, the surface energy is compensated by gas-gas interactions in the bulk phase, which leads to the decline of the adsorption heat. As more and more gas molecules are accumulated inside the pore, both gas-gas and gas-solid interactions become less attractive and eventually turn into repulsion. In the high-pressure region, the interplay of the attraction and repulsion branches of the gas-gas and gas-solid interactions determines the trend of the isosteric heat. For krypton adsorption in a small pore (0.9 nm), the maximum adsorption heat occurs at a lower pressure as the surface energy increases. For the larger pore (1.8 nm), the differential heat of adsorption first shows a maximum due to saturation of surface binding, then a minimum as the intermolecular repulsion becomes significant, and eventually rises with the pressure because of the surface repulsion. For adsorption in a large more (3.6 nm), surface repulsion becomes less important so that the isosteric heat declines at high pressure. Fig. S1 shows individual contributions to the internal energy for krypton adsorption in different slit pores. It is worth noting that the pressure effect on the differential heat as shown in Fig. 3 is very different from those predicted by the Fowler-Guggenheim[156] or the Hill-de Boer equation[157]. The mean-field methods predict that the heat of adsorption varies linearly with the loading, which approximately holds only at high pressure.

Because the differential heat of adsorption resembles partial molar properties, we expect that it is dependent on the system size, or more precise, the composition of the entire sampling cell. Such effect is apparent if we consider gas adsorption in Henry's law region, i.e., as the gas pressure approaches zero. In the limit of zero loading, the heat of adsorption

depends only on the adsorbate-adsorbate interactions. As shown in SI, the differential heat of adsorption for a monatomic ideal gas (IG) is given by

$$q_d^{IG} = RT - N_{AV} \frac{\int \phi(\mathbf{r}) \exp[-\beta\phi(\mathbf{r})] d\mathbf{r}}{\int \exp[-\beta\phi(\mathbf{r})] d\mathbf{r}} = RT - \langle u_{ext} \rangle \tag{62}$$

where $\phi(\mathbf{r})$ is the total potential energy of a gas molecule at position $\mathbf{r}$ for its interaction with the adsorbent, N_{AV} is the Avogadro number, and $\langle u_{ext} \rangle$ represents the molar external energy. As the system size increases, the gas-solid interaction becomes less significant for individual molecules. Therefore, the differential heat of adsorption declines along with the molar external energy. In the thermodynamic limit, $q_d^{IG} = RT$ because the denominator in Eq.(62) approaches infinite. By contrast, the isostere heat based on the surface excess is given by

$$q_{st}^{IG} = RT - N_{AV} \frac{\int \phi(\mathbf{r}) \exp[-\beta\phi(\mathbf{r})] d\mathbf{r}}{\int \{\exp[-\beta\phi(\mathbf{r})] - 1\} d\mathbf{r}} \tag{63}$$

which remains finite in Henry's law region.

Figure 4 shows the pore-size dependence of the isosteric heat at two representative pressures. At the low pressure (0.01 bar), the total isosteric heat is well represented by Henry's law. In this case, the differential heat of adsorption approaches RT for large pores as predicted by Eq. (62). However, the isosteric heat derived from excess model is very different. It drastically overestimates the differential heat of adsorption especially for large pores. Interesting, the system does not exhibit significant non-ideality even at 20 bar. As shown in Fig. 4(B), the surface excess is virtually independent of pore size in both cases while the total amounts continuously increases with the pore width.

We have also tested thermodynamic consistency between the differential heat of adsorption and various forms of isosteric heat for gas adsorption in nanoporous materials like MOFs, ZIFs and zeolites. Because of strong confinement and heterogeneous interactions, the conventional isostere models may result in problematic predictions in both low and high-pressure regions. Figure 5 illustrates various forms of heat for CH_4 adsorption in MFI zeolite and H_2 adsorption in Cu(hfipbb)(H_2hfipbb)$_{0.5}$. We see that both the excess and absolute models fail to reproduce the differential heat of adsorption at high pressure similar to that occurred in the slit-pore model. The isosteric heat of adsorption predicted by these conventional models diverge in the high pressure region that is most relevant for industrial applications such as gas storage and purification[35,36]. For H_2 adsorption in the MOF material, both the excess and the absolute models predict the isosteric heat with significant deviation from the differential heat of adsorption even at low pressure. The discrepancy in Henry's law region is consistent with that shown in Fig. 4A and may lead to more problems because the conventional models are commonly used to calibrate calorimetric equipment[129,145,158,159]. The inconsistency between isosteric heat of adsorption predicted from excess or absolute adsorption models and calorimetry data has been a controversial issue without a thorough explanation for a long time[127,159]. By comparing the different forms of isosteric heat, we provide an understanding that has been long overdue.

4.4. Conclusions

We present a rigorous thermodynamic framework for heat analysis without any assumptions on the geometric measures of the absorbent or operating conditions. Thermodynamic consistency between the differential heat of adsorption and different

forms of isosteric heat has been calibrated with simulation data for gas adsorption in model porous materials over a broad range of conditions. While the total isosteric heat, as defined in Eq.(57), is fully consistent with the differential heat of adsorption, the excess or absolute isosteric heat may lead to significant deviations from the exact results at both low and high pressure. Because the total isosteric heat is evaluated in terms of the total amount of gas in the sampling cell, it is independent of any specific experimental procedure to estimate the pore volume (or the dead space) as conventionally used in alternative isostere equations.

It should be noted that the Gibbsian thermodynamics is exact for any multiphase systems including gas adsorption discussed in this work. The conventional applications to heat analysis are problematic because the isosteric heats were defined in terms of dubious assumptions instead of rigorous derivations. While a common belief in the literature is that the difference between various definitions of isosteric heats of adsorption largely disappears at low pressure, we have demonstrated both analytically and numerically that the difference can be significant even in the ideal-gas region (i.e., Henry's law region). The discrepancy among different forms of the isosteric heat increases with the system size. We find that the absolute adsorption model works the best at low to intermediate pressure for absorbent with large micropores or mesopores and strong affinity to the adsorbates. For gas adsorption in nanoporous materials such as MOFs and zeolites, the conventional isostere models fail to reproduce the differential heat of adsorption at either low or high pressure. The exact thermodynamic model introduced in this work can be easily implemented in experimental and computational investigations of heat effects for adsorption processes including gas storage and separation.

Figure 4-1. (A) Schematic set up for gas adsorption measurements; (B) The slit-pore model for amorphous porous materials; (C) A representative framework material.

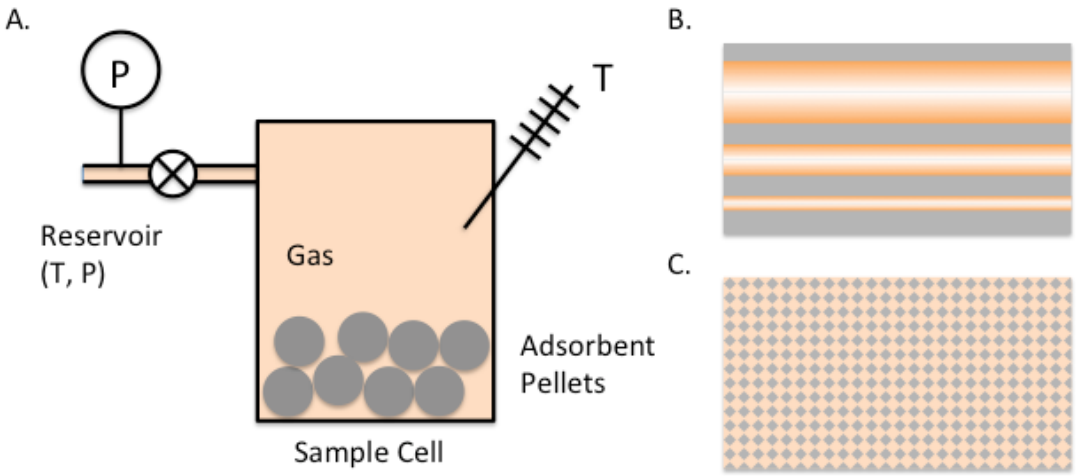

Figure 4-2. Gas adsorption and isosteric heat for H_2 (A, C) and Kr (B, D) in a slit pore at 298 K. In both cases, the pore width is 0.9 nm, and the reduced surface energy is $\varepsilon_{sf}^{*} \equiv \varepsilon_{sf} / \varepsilon_{N_2}$ =0.55, where ε_{N_2} stands for the LJ energy parameter for nitrogen. The solid, dash-dotted, and dashed lines represent the total, absolute and excess amount of adsorption, respectively (A, B), and the corresponding results for the isosteric heat (C, D). In C and D, the solid squares are the differential heat of adsorption generated from the ensemble fluctuation method, and the open circles are the corresponding results at the low-pressure limit.

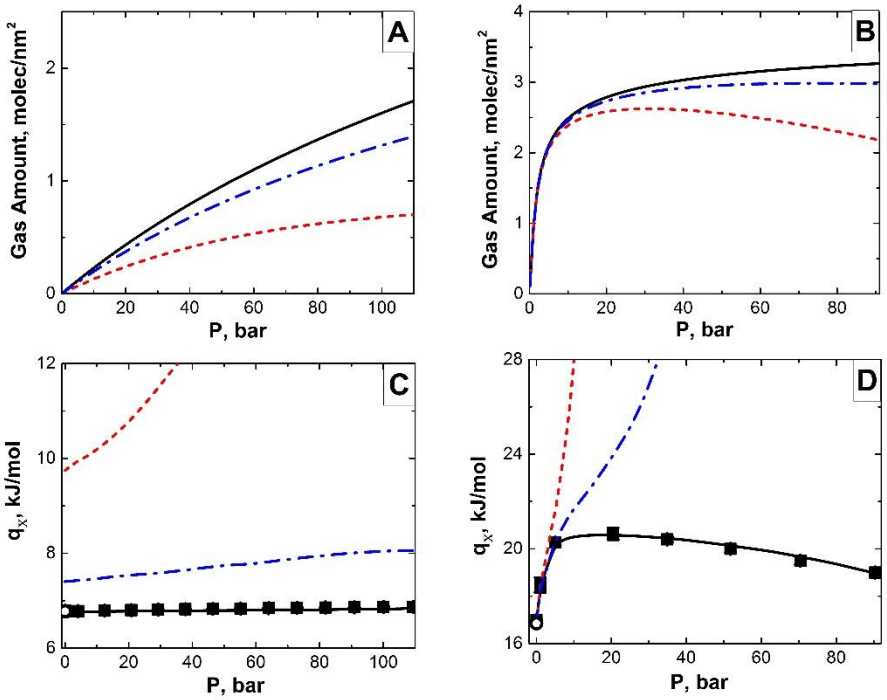

Figure 4-3. Effects of the reduced surface energy (ε_{sf}^*) and pore width (0.9 nm, 1.8 nm and 3.6 nm) on the isosteric heat for Kr adsorption in model slit pores at 298 K. Lines and symbols follow the same meanings as those in Fig. 2.

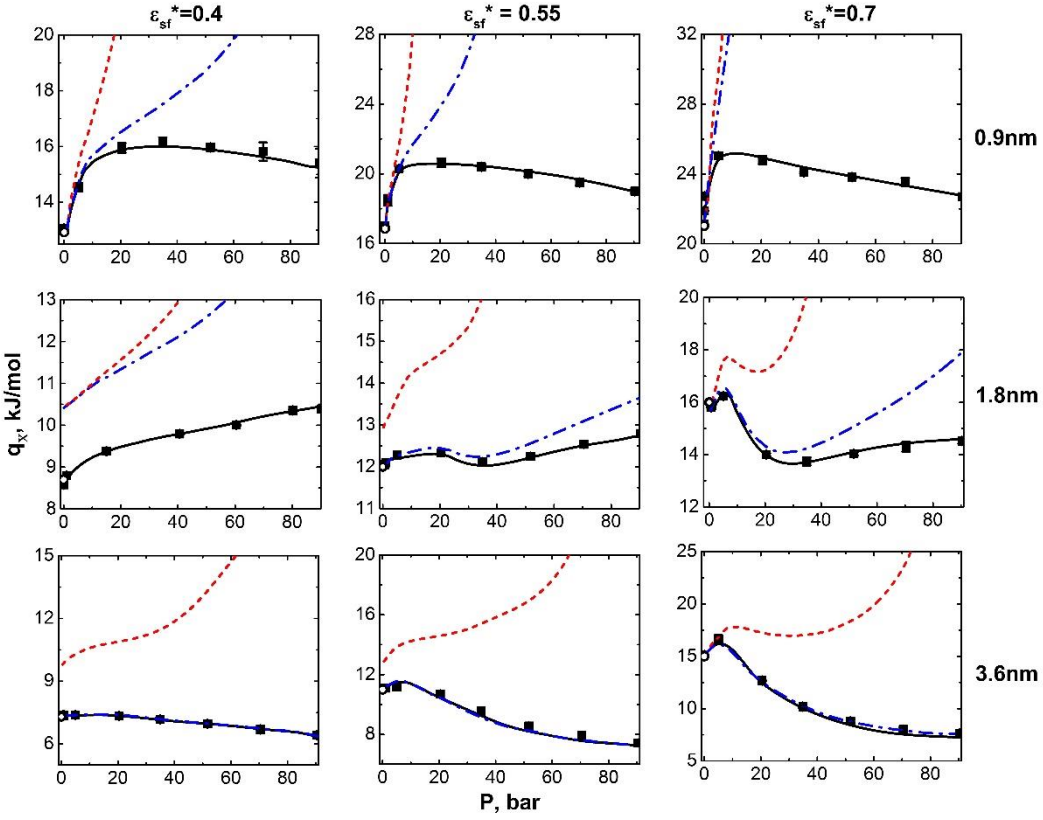

Figure 4-4. (A) Dependence of the total and excess isosteric heat of adsorption on the pore size. The red and blue circles represent the differential heat of adsorption at 0.01 bar and 20 bar bulk pressure, respectively. The solid and dashed red lines are predicted from Eqs.(62) and (63), respectively. The blue line is the total isosteric heat at 20 bar. (B) The total (solid lines) and excess (dashed lines) adsorption amounts at 0.01 bar and 20 bar. In both cases, T=298 K and the surface energy is ε_{sf}^{*}=0.55.

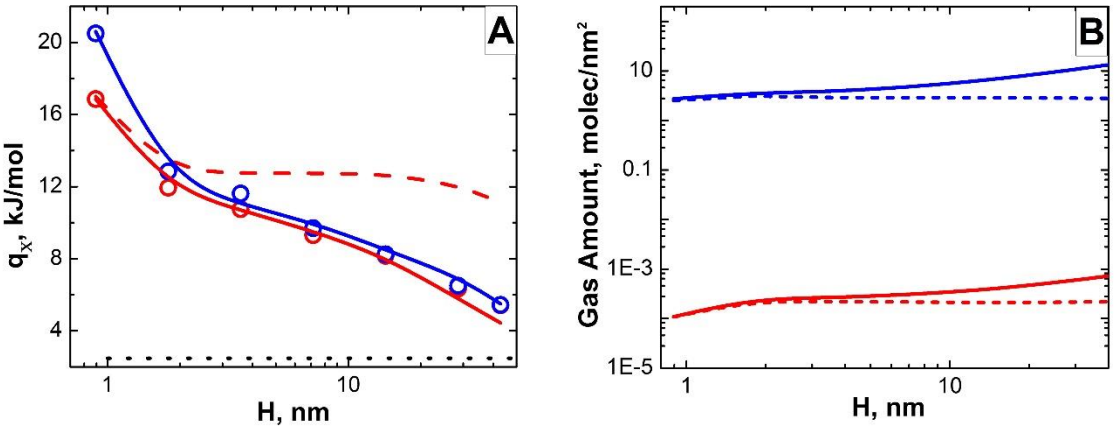

Figure 4-5. Isosteric heat for (A) CH_4 adsorption in silicate MFI at 298 K and (B) H_2 in Cu(hfipbb)(H_2hfipbb)$_{0.5}$ at 243 K. The insets show the three-dimensional structures of the corresponding porous materials. Lines and symbols follow the same meanings as those in Figs. 2 and 3.

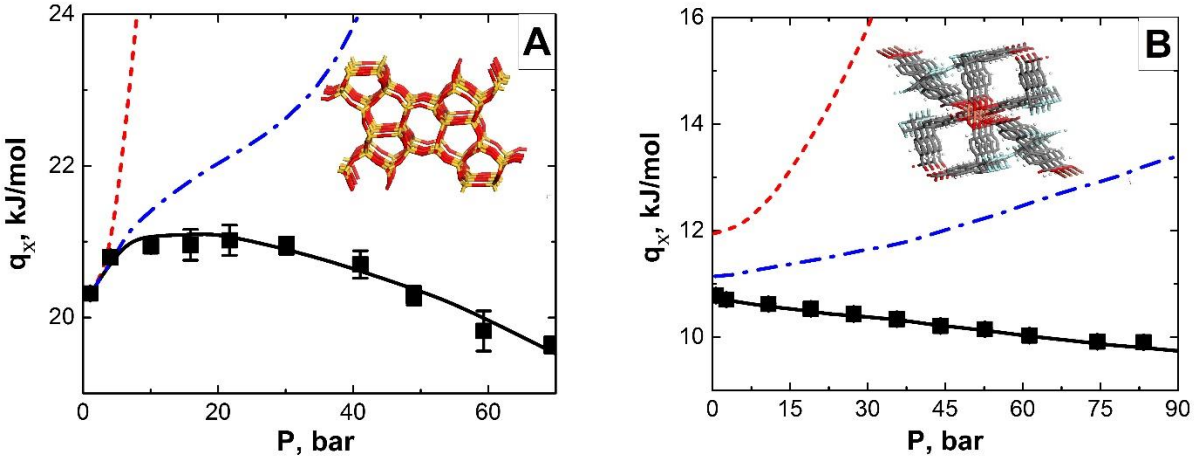

Support Information

This supplementary material details the Grand Canonical Monte Carlo (GCMC) simulations employed in this work and the ensemble fluctuation method for calculation of the isosteric heat of adsorption.

Molecular Models and Simulation Methods

We used the united atom model for all gas molecules and the rigid molecular model for the nanoporous materials, and the Lennard-Jones (LJ) potential is used to describe all atomic pair interaction energies for realistic materials:

$$u_{ij}(\mathbf{r}) = 4\varepsilon_{ij}\left[\left(\frac{\sigma_{ij}}{r}\right)^{12} - \left(\frac{\sigma_{ij}}{r}\right)^{6}\right] \tag{S.64}$$

where the cross parameters are given by Lorentz-Berthelot combination rule

$$\varepsilon_{ij} = \sqrt{\varepsilon_i \varepsilon_j} \qquad \sigma_{ij} = \frac{\sigma_i + \sigma_j}{2} \tag{S.65}$$

The carbon slit pore model is represented by the Steele Wall 10-4-3 potential:

$$V_{sf}(z) = 2\pi\rho_s\varepsilon_{sf}\sigma_{sf}^2\Delta\left[\frac{2}{5}\left(\frac{\sigma_{sf}}{z}\right)^{10} - \left(\frac{\sigma_{sf}}{z}\right)^{4} - \frac{\sigma_{sf}^4}{3\Delta(0.61\Delta + z)^3}\right] \tag{S.66}$$

where $\rho_s = 114 nm^{-3}$ is the graphite carbon number density and $\Delta = 0.335 nm$ is the graphite interlayer spacing, and σ_{sf} and ε_{sf} are size and energy cross parameters of the wall-fluid Lennard-Jones potential. For a slit pore with width H, the fluid molecule will interact with two graphite slabs, thus the full external potential is written as:

$$\varphi_{ext}(z) = V_{sf}(z) + V_{sf}(\mathrm{H} - z) \tag{S.67}$$

The LJ parameters for example MOF Cu(hfipbb)(H_2hfipbb)$_{0.5}$ is from the universal force field (UFF)[38], while parameters of MFI is from previous computational studies [160,161]. The structures for both realistic materials are from experimental determined crystalline information files (CIFs)[121,152].

Adsorption isotherms and of gas molecules in both model adsorbent and realistic materials were predicted using the conventional GCMC simulation method. The MC simulations were performed on 2x2x2 unit cells of adsorbents under 3D periodic boundary conditions. The van der Waals (VDW) interactions were evaluated using 12.9 Å cutoff in shifted potential style. Each GCMC simulation run includes 10^6 moves for equilibration and $5x10^6$ moves for data collection. MC moves included insertions, deletions, and translations of the gas molecules. Chemical potentials used in the simulations were calculated using the MBWR equation of state. The data of each simulation trajectory was divided into 10000 blocks in order to perform the ensemble fluctuation calculation for isosteric heat of adorption. MC simulations were carried out using the Towhee program[120].

Ensemble Fluctuation

Isosteric heats of adsorption are predicted by ensemble fluctuation during the GCMC simulations, which is the standard way to obtain the isosteric heat directly with simulation[147], when the isotherms are collected at the same time. The ensemble fluctuation method is essentially the equivalent way to determine the isosteric heat of adsorption directly from the differential change of internal energy of the entire cell in simulation[124,162],

$$q_{st} = H_b - \left(\frac{\partial U}{\partial N}\right)_{T,V} = H_b - \frac{f(U,N)}{f(\mathrm{N},\mathrm{N})} \qquad \text{(S.68)}$$

where fluctuation of X and Y is $f(\mathrm{X},\mathrm{Y}) = \langle XY \rangle - \langle X \rangle \langle Y \rangle$.

To relate the isosteric heat of adsorption with isotherms, we apply Gibbs-Duhem Equation, we apply Eq.(6),

$$\left(\frac{\partial U}{\partial N}\right)_{T,V} = h_0 + k_B \left(\frac{\partial \ln f}{\partial T}\right)_{N,V}$$

As a result, the isosteric heat of adsorption obtained by ensemble fluctuation method is consistent with Eq.(7) as shown below,

$$q_{st} = \Delta H_b - RT^2 \left(\frac{\partial \ln f}{\partial T}\right)_{N,V}$$

Appendix

Derivation of Eq.(10) and Eq.(11) are showing below:

In Henry's law region, the total gas amount is proportional to the pressure, and Henry's constant is defined as:

$$H^{\mathrm{X}} \equiv \lim_{P \to 0} \frac{N^{\mathrm{X}}}{P} \tag{S.69}$$

X refers to total or excess adsorption, respectively. And we consider total gas amount first. The gas-gas interaction is neglected in Henry's region, so the gas amount can be expresses as

$$N^{tot} = \int \rho_b \exp[-\beta\varphi(\mathbf{r})]\, d\mathbf{r} \tag{S.70}$$

Since bulk phase is ideal gas, Eq.(7) will be reduced to the following equation:

$$q_t = R\left[\frac{\partial \ln H}{\partial(1/\mathrm{T})}\right]_{V,\mathrm{N}^{tot}} \tag{S.71}$$

Combining Eq.(S.7) and Eq.(S.8), we have Eq.(11)

$$q_t = RT - \frac{R\int \varphi(\mathbf{r}) \exp[-\beta\varphi(\mathbf{r})]\, d\mathbf{r}}{k_B \int \exp[-\beta\varphi(\mathbf{r})]\, d\mathbf{r}} = RT - N_{AV} \left\langle u_{ext} \right\rangle$$

Eq.(12) is similarly derived with a definition of $N^{ex} = \int \rho_b \{\exp[-\beta\varphi(\mathbf{r})] - 1\} d\mathbf{r}$, so

$$q_{ex} = RT - \frac{R\int \varphi(\mathbf{r}) \exp[-\beta\varphi(\mathbf{r})]\, d\mathbf{r}}{k_B \int \{\exp[-\beta\varphi(\mathbf{r})] - 1\} d\mathbf{r}}$$

Figure S4-1. Gas-gas interaction energy (red line with circles) and gas-solid interaction energy (blue line with square) with increasing loading for Kr adsorption in slit pore of 0.9nm, 1.8nm and 3.6nm from (A) to (C) at 298K, and we choose ε_{sf}^{*}=0.7 as an example to explain the different trends of isosteric heat of adsorption for different pore width on Fig.2.

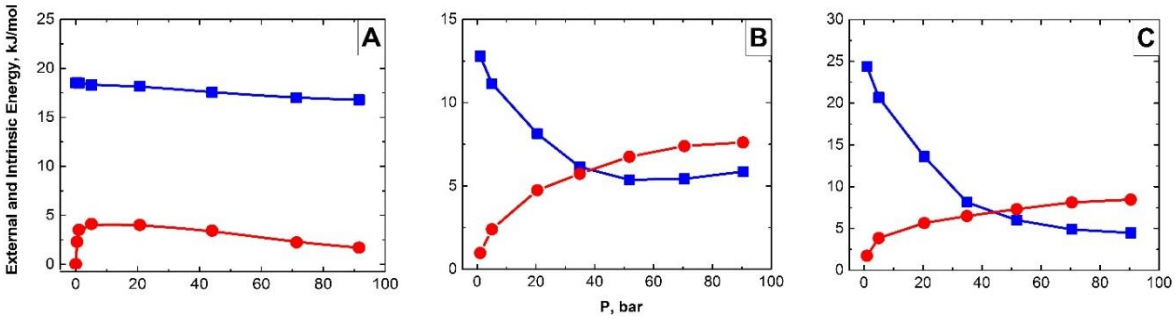

Table S4-1. Size and Potential Parameters for He, N_2, Kr, CH_4, H_2 and Steele Wall, and the four different values of ε_{ss} correspond to $\varepsilon_{sf}^{*} = \varepsilon_{sf} / \varepsilon_{ff, N2}$=0.3, 0.4, 0.55 and 0.7.

Gas	**σ_{ff}, Å**	**ε_{ff}/k_B, K**
He	2.602	10.41
N_2	3.572	93.98
Kr	3.636	166.4
CH_4	3.73	148
H_2	2.958	36.7
Steele Wall	**σ_{ss}, Å**	**ε_{ss}/k_B, K**
	3.4	8.5, 15, 28, 46

References

1. Myers AL. Thermodynamics of adsorption in porous materials. *AIChE Journal*. 2002;48(1):145-160.

2. Bhatia SK, Myers AL. Optimum Conditions for Adsorptive Storage. *Langmuir*. 2006/02/01 2006;22(4):1688-1700.

3. Lee S-J, Bae Y-S. Can Metal–Organic Frameworks Attain New DOE Targets for On-Board Methane Storage by Increasing Methane Heat of Adsorption? *The Journal of Physical Chemistry C.* 2014/08/28 2014;118(34):19833-19841.

4. Amrouche H, Creton B, Siperstein F, Nieto-Draghi C. Prediction of thermodynamic properties of adsorbed gases in zeolitic imidazolate frameworks. *RSC Advances.* 2012;2(14):6028-6035.

5. Sircar S. Basic Research Needs for Design of Adsorptive Gas Separation Processes. *Industrial & Engineering Chemistry Research.* 2006/08/01 2006;45(16):5435-5448.

6. Hartzog DG, Sircar S. Sensitivity of PSA process performance to input variables. *Adsorption.*1(2):133-151.

7. Vuong T, Monson PA. Monte Carlo Simulation Studies of Heats of Adsorption in Heterogeneous Solids. *Langmuir.* 1996/01/01 1996;12(22):5425-5432.

8. Myers AL, Monson PA. Physical adsorption of gases: the case for absolute adsorption as the basis for thermodynamic analysis. *Adsorption.* 2014;20(4):591-622.

9. Whittaker PB, Wang X, Zimmermann W, Regenauer-Lieb K, Chua HT. Predicting the Integral Heat of Adsorption for Gas Physisorption on Microporous and Mesoporous Adsorbents. *The Journal of Physical Chemistry C.* 2014/04/24 2014;118(16):8350-8358.

10. Chakraborty A, Saha BB, Koyama S, Ng KC. On the thermodynamic modeling of the isosteric heat of adsorption and comparison with experiments. *Applied Physics Letters.* 2006;89(17):171901.

11. Shen D, Bülow M, Siperstein F, Engelhard M, Myers AL. Comparison of Experimental Techniques for Measuring Isosteric Heat of Adsorption. *Adsorption.*6(4):275-286.

12. Zimmermann W, Keller JU. A new calorimeter for simultaneous measurement of isotherms and heats of adsorption. *Thermochimica Acta.* 2003;405(1):31-41.

13. Siperstein F, Gorte RJ, Myers AL. A New Calorimeter for Simultaneous Measurements of Loading and Heats of Adsorption from Gaseous Mixtures. *Langmuir.* 1999/02/01 1999;15(4):1570-1576.

14. Pinto ML, Pires J, Carvalho AP, de Carvalho MB. On the Difficulties of Predicting the Adsorption of Volatile Organic Compounds at Low Pressures in Microporous Solid: The

Example of Ethyl Benzene. *The Journal of Physical Chemistry B.* 2006/01/01 2006;110(1):250-257.

15. Langmuir I. THE ADSORPTION OF GASES ON PLANE SURFACES OF GLASS, MICA AND PLATINUM. *Journal of the American Chemical Society*. 1918/09/01 1918;40(9):1361-1403.

16. Mathias PM, Kumar R, Moyer JD, et al. Correlation of Multicomponent Gas Adsorption by the Dual-Site Langmuir Model. Application to Nitrogen/Oxygen Adsorption on 5A-Zeolite. *Industrial & Engineering Chemistry Research.* 1996/01/01 1996;35(7):2477-2483.

17. Bimbo N, Ting VP, Hruzewicz-Kolodziejczyk A, Mays TJ. Analysis of hydrogen storage in nanoporous materials for low carbon energy applications. *Faraday Discussions.* 2011;151(0):59-74.

18. Bimbo N, Sharpe JE, Ting VP, Noguera-Díaz A, Mays TJ. Isosteric enthalpies for hydrogen adsorbed on nanoporous materials at high pressures. *Adsorption.* 2013;20(2):373-384.

19. Whittaker PB, Wang X, Regenauer-Lieb K, Chua HT. Predicting isosteric heats for gas adsorption. *Physical Chemistry Chemical Physics.* 2013;15(2):473-482.

20. Czepirski L, JagieŁŁo J. Virial-type thermal equation of gas—solid adsorption. *Chemical Engineering Science.* 1989/01/01 1989;44(4):797-801.

21. Chowdhury P, Mekala S, Dreisbach F, Gumma S. Adsorption of CO, CO2 and CH4 on Cu-BTC and MIL-101 metal organic frameworks: Effect of open metal sites and adsorbate polarity. *Microporous and Mesoporous Materials.* 2012;152:246-252.

22. Mishra P, Mekala S, Dreisbach F, Mandal B, Gumma S. Adsorption of CO2, CO, CH4 and N2 on a zinc based metal organic framework. *Separation and Purification Technology*. 2012;94:124-130.

23. Mason JA, Veenstra M, Long JR. Evaluating metal-organic frameworks for natural gas storage. *Chemical Science.* 2014;5(1):32-51.

24. Salem MMK, Braeuer P, Szombathely Mv, et al. Thermodynamics of High-Pressure Adsorption of Argon, Nitrogen, and Methane on Microporous Adsorbents. *Langmuir*. 1998/06/01 1998;14(12):3376-3389.

25. Gumma S, Talu O. Net Adsorption: A Thermodynamic Framework for Supercritical Gas Adsorption and Storage in Porous Solids. *Langmuir*. 2010/11/16 2010;26(22):17013-17023.

26. Pan H, Ritter JA, Balbuena PB. Examination of the Approximations Used in Determining the Isosteric Heat of Adsorption from the Clausius−Clapeyron Equation. *Langmuir*. 1998/10/01 1998;14(21):6323-6327.

27. Myers AL, Monson PA. Adsorption in Porous Materials at High Pressure: Theory and Experiment. *Langmuir*. 2002/12/01 2002;18(26):10261-10273.

28. Hill TL. Theory of physical adsorption. *Adv. Catal.* 1952;4(21):1.

29. Furukawa H, Miller MA, Yaghi OM. Independent verification of the saturation hydrogen uptake in MOF-177 and establishment of a benchmark for hydrogen adsorption in metal-organic frameworks. *Journal of Materials Chemistry*. 2007;17(30):3197-3204.

30. Malbrunot P, Vidal D, Vermesse J, Chahine R, Bose TK. Adsorbent helium density measurement and its effect on adsorption isotherms at high pressure. *Langmuir*. Feb 5 1997;13(3):539-544.

31. Malbrunot P, Vidal D, Vermesse J, Chahine R, Bose TK. Adsorption Measurements of Argon, Neon, Krypton, Nitrogen, and Methane on Activated Carbon up to 650mpa. *Langmuir*. Feb 1992;8(2):577-580.

32. Dunne JA, Rao M, Sircar S, Gorte RJ, Myers AL. Calorimetric Heats of Adsorption and Adsorption Isotherms. 2. O2, N2, Ar, CO2, CH4, C2H6, and SF6 on NaX, H-ZSM-5, and Na-ZSM-5 Zeolites. *Langmuir*. 1996/01/01 1996;12(24):5896-5904.

33. Wu D, Navrotsky A. Probing the energetics of organic–nanoparticle interactions of ethanol on calcite. *Proceedings of the National Academy of Sciences*. April 28, 2015 2015;112(17):5314-5318.

34. Nicholson DP, N, G. *Computer Simulation and the Statistical Mechanics of Adsorption*. London: Academic Press; 1982.

35. Sircar S. Gibbsian Surface Excess for Gas AdsorptionRevisited. *Industrial & Engineering Chemistry Research*. 1999/10/01 1999;38(10):3670-3682.

36. Talu O, Myers AL. Molecular simulation of adsorption: Gibbs dividing surface and comparison with experiment. *AIChE Journal*. 2001;47(5):1160-1168.

37. Bolis V. Fundamentals in Adsorption at the Solid-Gas Interface. Concepts and Thermodynamics. *Springer Ser Mater S*. 2013;154:3-50.

38. Balbuena PB, Gubbins KE. Theoretical interpretation of adsorption behavior of simple fluids in slit pores. *Langmuir*. 1993/07/01 1993;9(7):1801-1814.

39. Lastoskie C, Gubbins KE, Quirke N. Pore size heterogeneity and the carbon slit pore: a density functional theory model. *Langmuir*. 1993/10/01 1993;9(10):2693-2702.

40. Baerlocher CM, L. B. Database of Zeolite Structures. 2001; http://www.iza-structure.org/databases/.

41. Lee J, Li J, Jagiello J. Gas sorption properties of microporous metal organic frameworks. *Journal of Solid State Chemistry*. 2005;178(8):2527-2532.

42. Pan L, Sander MB, Huang X, et al. Microporous Metal Organic Materials: Promising Candidates as Sorbents for Hydrogen Storage. *Journal of the American Chemical Society.* 2004/02/01 2004;126(5):1308-1309.

43. Steele WA. The interaction of rare gas atoms with graphitized carbon black. *The Journal of Physical Chemistry.* 1978/04/01 1978;82(7):817-821.

44. Li J-R, Sculley J, Zhou H-C. Metal–Organic Frameworks for Separations. *Chemical Reviews.* 2012/02/08 2012;112(2):869-932.

45. Martin MG, Siepmann JI. Transferable Potentials for Phase Equilibria. 1. United-Atom Description of n-Alkanes. *The Journal of Physical Chemistry B.* 1998/04/01 1998;102(14):2569-2577.

46. Buch V, Devlin JP. Preferential adsorption of ortho‐H2 with respect to para‐H2 on the amorphous ice surface. *The Journal of Chemical Physics.* 1993;98(5):4195-4206.

47. Martin MG. MCCCS Towhee: a tool for Monte Carlo molecular simulation. *Molecular Simulation.* 2013/12/01 2013;39(14-15):1212-1222.

48. Fowler RH, Guggenheim EA. *Statistical thermodynamics; a version of statistical mechanics for students of physics and chemistry*. New York Cambridge, Eng.,: The Macmillan Company; The University Press; 1939.

49. de Boer JH. *The dynamical character of adsorption*. 2nd ed. Oxford,: Clarendon P.; 1968.

50. Dunne JA, Mariwala R, Rao M, Sircar S, Gorte RJ, Myers AL. Calorimetric Heats of Adsorption and Adsorption Isotherms. 1. O2, N2, Ar, CO2, CH4, C2H6, and SF6 on Silicalite. *Langmuir.* 1996/01/01 1996;12(24):5888-5895.

51. Hulvey Z, Lawler KV, Qiao Z, et al. Noble Gas Adsorption in Copper Trimesate, HKUST-1: An Experimental and Computational Study. *The Journal of Physical Chemistry C.* 2013/10/03 2013;117(39):20116-20126.

52. Rappe AK, Casewit CJ, Colwell KS, Goddard WA, Skiff WM. UFF, a full periodic table force field for molecular mechanics and molecular dynamics simulations. *Journal of the American Chemical Society.* 1992/12/01 1992;114(25):10024-10035.

53. García-Pérez E, Parra JB, Ania CO, et al. A computational study of CO2, N2, and CH4 adsorption in zeolites. *Adsorption.* 2007;13(5):469-476.

54. Liu B, Smit B. Comparative Molecular Simulation Study of CO2/N2 and CH4/N2 Separation in Zeolites and Metal−Organic Frameworks. *Langmuir.* 2009/05/19 2009;25(10):5918-5926.

55. He Y, Seaton NA. Monte Carlo Simulation and Pore-Size Distribution Analysis of the Isosteric Heat of Adsorption of Methane in Activated Carbon. *Langmuir.* 2005/08/01 2005;21(18):8297-8301.

Chapter 5. Study of Differential Heat of Adsorption by Classical Density Functional Theory

Abstract

In order to gain further understanding of thermal effects related to gas adsorption in different porous materials, we formulate a theoretical procedure to predict the isosteric heat and calculate the differential heat of adsorption using the classical density functional theory (DFT). Compared with the ensemble fluctuation method conventionally used for differential heat calculations, DFT is able to predict the heat of adsorption together with adsorption calculations with no increase in the computational cost. The superior computational efficiency opens up new opportunities to calibrate empirical force fields with both adsorption isotherms and calorimetry data from experiments. Importantly, the classical DFT is directly applicable to high-pressure conditions relevant to gas storage and to gas separation involving pressure swing adsorption processes where calorimetry data are sparse.

5.1. Introduction

Heat of adsorption is one of the most fundamental thermodynamic quantities to describe surface phenomena[31]. It is directly related to adsorbate-adsorbent interactions that are essential for assessment and screening of porous materials useful for gas storage and separation [32-34] and for thermal managements of industrial processes including various forms of pressure swing adsorption (PSA) [35,36].

In this work, we apply the rigorous thermodynamic procedure for heat analysis that is free of inconsistency yet convenient for practical applications with classical density functional theory. The thermodynamic relations between grand potential and internal energy is used to demonstrate how to calculate the differential heat self-consistently in model slit pores and crystalline porous materials. By avoiding problematic division between the bulk and adsorbed phases or semi-empirical estimation of the pore volume, the new theoretical procedure enables a faithful description of heat effects important for diverse applications of gas adsorption processes. In addition, DFT represents a powerful tool for studying gas adsorption compared with standard GCMC simulations; it is able to predict the isotherm and isosteric heat self-consistently.

5.2. Theory and Methods

Consider the heat effect for gas adsorption based on the working conditions of a calorimeter shown schematically in Fig. 1. According to the first law of thermodynamics for the open system, the differential heat for injecting dn mole of gas into the adsorption chamber (calorimeter cell) with a fixed volume V is

$$đQ = dU_T - H_b dn \tag{72}$$

where dU_T is the change in the internal energy of the entire chamber, and H_b is the molar enthalpy of the bulk gas at the reservoir temperature T and pressure P.

The *differential heat of adsorption*, designated as q_d, reflects the difference between the molar enthalpy of the gas in the bulk phase, H_b, and the differential internal energy, $(\partial U / \partial N)_{T,V}$

$$q_d = -\frac{\cancel{d}Q}{dn} = H_b - \left(\frac{\partial U_T}{\partial n} \right)_{T,V} \tag{73}$$

The negative sign here refers to the differential heat measured by the calorimeter, which is opposite to the system energy change.

We may compare Eq.(73) with the differential energy of adsorption, which is given by

$$\Delta \bar{U} = \left(\frac{\partial U_T}{\partial n} \right)_{T,V} - U_b \tag{74}$$

for the adsorption of a one-component gas. The difference between the differential heat and the absolute value of the differential energy of adsorption amounts to the reversible work of compression for addition of the gas molecules

$$q_d + \Delta \bar{U} = PV = ZRT \tag{75}$$

where Z stands for the compressibility factor of the bulk gas.

The total internal energy inside the calorimeter cell U_T can be separated into an intrinsic part U_{in}, and an external part U_{ext}, both are extensive properties proportional to the total number of gas molecules N.

$$U_T = U_{in} + U_{ext} = N(u_{in} + u_{ext}) \tag{76}$$

The intrinsic energy accounts for the kinetic energy and the potential energy of gas molecules free of the gas-absorbent interactions, and the latter is included in the external energy

$$U_{ext} = \int d\mathbf{r}\rho(\mathbf{r})\varphi(\mathbf{r}) \tag{77}$$

where $\rho(\mathbf{r})$ stands for the density profile of gas molecules inside the cell, and $\varphi(\mathbf{r})$ is the potential energy for a gas molecule due to the presence of the absorbent. It should be noted that the integration in Eq.(77) extends to the entire space (i.e., the calorimeter cell with macroscopic volume V). In this work, we do not distinguish gas molecules in the bulk or the adsorbed phase. While such distinction is possible in the framework of Gibbsian thermodynamics, unnecessary confusion may arise in practical applications. At fixed T and P for the bulk gas, the per molecule intrinsic internal energy and the external energy, u_{in} and u_{ext}, are constants.

Statistical Mechanics Derivations

To calculate the heat of adsorption rigorously, we calculate the total internal energy from the statistic-mechanical equations. For gas adsorption at given T and P in the bulk, we use the grand canonical ensemble for the adsorption chamber

$$\Omega = -k_B T \ln \Xi \tag{78}$$

where the grand partition function is

$$\Xi = \sum_{\nu} \exp\left[\beta\left(\mu N_\nu - E_\nu\right)\right] \tag{79}$$

In Eq.(79), N_ν and E_ν stands for the number of gas molecules and the total system energy at microstate ν , respectively. The total internal energy includes three contributions: the kinetic energy of ideal gas molecules, the gas-gas interaction potential, and the gas-absorbent external energy. It is related to the grand potential by

$$U = \left[\frac{\partial \beta\Omega}{\partial \beta}\right]_{\mu,\mathrm{V}} + \mu N = \Omega + \beta\left[\frac{\partial \Omega}{\partial \beta}\right]_{\mu,\mathrm{V}} + \mu N \,. \tag{80}$$

It can be shown that, for a monatomic ideal gas, Eq.(80) yields an internal energy density the same as that given by Eq.(77).

Ideal-gas limit

We may illustrate the above procedure with the adsorption of a monatomic ideal gas. In this case, the intrinsic internal energy per molecule is

$$u_{in} = 3k_B T / 2 \tag{81}$$

and the external energy per molecule is

$$u_{ext} = \int d\mathbf{r}\rho(\mathbf{r})\varphi(\mathbf{r}) / \int d\mathbf{r}\rho(\mathbf{r}) \tag{82}$$

The density profile of ideal-gas molecules is given by the Boltzmann equation

$$\rho(\mathbf{r}) = \rho_0 \exp[-\beta\varphi(\mathbf{r})] \tag{83}$$

where ρ_0 is the bulk gas density at T and P , and $\beta = 1/(k_B T)$.

Alternatively, the internal energy per molecule may be expressed in terms of the single molecule canonical partition function ξ

$$u = -\left(\frac{\partial \ln \xi}{\partial \beta}\right)_V \tag{84}$$

where $\xi = \Lambda^{-3}\int d\mathbf{r}\exp[-\beta\varphi(\mathbf{r})]$, and Λ is the thermal wave length of the gas molecule.

From Eq.(73), we can find differential heat from the adsorption of an ideal gas

$$q_d^0 = H_0 - N_{AV}u = RT - N_{AV}u_{ext} \tag{85}$$

where N_{AV} is the Avogadro constant, and $R = N_{AV}k_B$ is the gas constant. For a monatomic ideal gas (reference state), the molar enthalpy is $H_0 = 5RT/2$.

To connect Eq.(85) with the Clapeyron equation conventionally used in the adsorption literature, we note that the reduced chemical potential of a monatomic ideal gas $\beta\mu^{IG} = \ln(\beta P\Lambda^3)$ is related to the single molecular canonical partition function

$$\beta\mu^{IG} = \left(\frac{\partial\beta F^{IG}}{\partial N}\right)_{T,V} = -\ln\xi \tag{86}$$

The Gibbs-Duhem equation is given by

$$\left(\frac{\partial\beta\mu^{IG}}{\partial\beta}\right)_{N,V} = \beta^{-1} + \left(\frac{\partial\ln P\Lambda^3}{\partial\beta}\right)_{N,V} = \left(\frac{\partial\ln\Lambda^3}{\partial\beta}\right)_{N,V} - \left(\frac{\partial\ln\xi\Lambda^3}{\partial\beta}\right)_{N,V} \tag{87}$$

It can be shown that the last term in Eq.(87) corresponds to the external energy per molecule, i.e.

$$u_{ext} = -\left(\frac{\partial\ln\xi\Lambda^3}{\partial\beta}\right)_{N,V} \tag{88}$$

Rearrangement of Eq.(87) yields

$$-\left(\frac{\partial\ln P}{\partial\beta}\right)_{N,V} = k_BT - u_{ext} \tag{89}$$

At ideal gas limit, this equation will be reduced to the conventional Clausius-Clapeyron Equation, which is most widely used to calculate isosteric heat of adsorption from isotherms at different temperature[8].

$$q_d^0 = -N_{AV}\left(\frac{\partial \ln P}{\partial \beta}\right)_{N,V} = RT^2\left(\frac{\partial \ln P}{\partial T}\right)_{N,V} \tag{90}$$

It can been proven from the single molecular canonical partition function that Eq.(90) is closely related to the external energy per molecule at the ideal gas limit for monatomic gas molecules:

$$-\left(\frac{\partial \ln P}{\partial \beta}\right)_{N,V} = k_B T - u_{ext} \tag{91}$$

And then we show the thermodynamic consistency between Eq.(90) and Eq.(73) is only valid under the ideal gas limit:

$$q_d^0 = H_0 - N_{AV}u = RT - N_{AV}u_{ext} \tag{92}$$

DFT method

In the framework of the classical density functional theory (DFT), the grand potential is given by

$$\Omega = F[\rho(\mathbf{r})] + \int d\mathbf{r}\rho(\mathbf{r})[\varphi(\mathbf{r}) - \mu]. \tag{93}$$

where $F[\rho(\mathbf{r})]$ stands for the intrinsic Helmholtz energy. Following the conventional definition, the Helmholtz energy is

$$A \equiv F[\rho(\mathbf{r})] + \int d\mathbf{r}\rho(\mathbf{r})\varphi(\mathbf{r}) \tag{94}$$

where the intrinsic Helmholtz energy is

$$\beta F = \int d\mathbf{r}\rho(\mathbf{r})\{\ln[\rho(\mathbf{r})\Lambda^3]-1\} + \beta F^{ex}[\rho(\mathbf{r})]. \tag{95}$$

The density profile is given by the Euler-Lagrange equation

$$\begin{aligned}\rho(\mathbf{r}) &= \rho_0 \exp[-\beta\varphi(\mathbf{r}) - \beta\Delta\mu^{ex}(\mathbf{r})] \\ &= \frac{1}{\Lambda^3}\exp[-\beta\varphi(\mathbf{r}) - \beta\mu^{ex}(\mathbf{r}) + \beta\mu]\end{aligned}. \tag{96}$$

where $\mu^{ex}(\mathbf{r}) = \delta F / \delta\rho(\mathbf{r})$. Substituting Eqs.(95) and (96) into (93), we may obtain a simplified expression for the grand potential

$$\beta\Omega = -\int d\mathbf{r}\rho(\mathbf{r})[\beta\mu^{ex}(\mathbf{r})+1] + \beta F^{ex}[\rho(\mathbf{r})]. \tag{97}$$

In the absence of intermolecular interactions, Eq.(97) reduces to the grand potential of a monatomic ideal gas as expected. With the density profile solved from Eq.(96) , we evaluate the grand potential from Eq.(97) and subsequently the internal energy from Eq.(80) numerically.

For a one-component system, we have

$$\left(\frac{\partial U_T}{\partial n}\right)_{T,V} = \frac{U}{N} = \frac{1}{N}\left[\frac{\partial\beta\Omega}{\partial\beta}\right]_{\mu,\mathrm{V}} + \mu. \tag{98}$$

As a result, the differential heat is

$$q_d = H_b - N_A\mu - \frac{1}{n}\left[\frac{\partial\beta\Omega}{\partial\beta}\right]_{\mu,\mathrm{V}} = TS_b - \frac{1}{n}\left[\frac{\partial\beta\Omega}{\partial\beta}\right]_{\mu,\mathrm{V}} \tag{99}$$

where S_b is the molar entropy of the bulk gas. For a monatomic gas, the bulk molar entropy includes an ideal gas term given by the Sackur–Tetrode equation and an excess that can be calculated from an equation of state:

$$S_b = -R\ln(\rho_b\Lambda^3) + 5/2 + S^{ex} \tag{100}$$

The differential heat is a thermodynamic quantity independent of the gas molecular mass. However, Eq.(99) suggests otherwise because the thermal wavelength is related to the molecular mass. The dilemma can be resolved by considering that ρ_0 is temperature (or β) dependent when the partial derivative $\partial\beta\Omega/\partial\beta$ is evaluated at a fixed chemical potential. To show this explicitly, we may write the grand potential in terms of an ideal part and an excess:

$$\Omega = \Omega^{id} + \Omega^{ex} \tag{101}$$

where

$$\beta\Omega^{id} = -\int d\mathbf{r}\rho(\mathbf{r}) = -\frac{1}{\Lambda^3}\int d\mathbf{r}\exp[-\beta\varphi(\mathbf{r}) - \beta\mu^{ex}(\mathbf{r}) + \beta\mu] \tag{102}$$

$$\Omega^{ex} = F^{ex}[\rho(\mathbf{r})] - \int d\mathbf{r}\rho(\mathbf{r})\mu^{ex}(\mathbf{r}) \tag{103}$$

It can be shown that the ideal part leads to an internal energy per molecule

$$U^{id}/N = \frac{1}{N}\left(\frac{\partial\beta\Omega^{id}}{\partial\beta}\right)_{V,\mu} + \mu = \frac{3k_BT}{2} + \frac{\int d\mathbf{r}[\varphi(\mathbf{r}) + \partial\beta\mu^{ex}(\mathbf{r})/\partial\beta]\exp[-\beta\varphi(\mathbf{r}) - \beta\mu^{ex}(\mathbf{r})]}{\int d\mathbf{r}\exp[-\beta\varphi(\mathbf{r}) - \beta\mu^{ex}(\mathbf{r})]}$$

(104)

Apparently, Eq.(104) is independent of the molecular mass. Because the ideal contribution includes a temperature derivative at each position, it is not as convenient as direct evaluation of $\partial\beta N/\partial\beta$ numerically. So in the following results and discussion, we applied Eq.(99) for differential heat calculations from DFT method.

Ensemble Fluctuation method

Differential heat of adsorption can also be predicted by ensemble fluctuation during the GCMC simulations, which is the standard way to obtain the differential heat directly

with simulation[147], and the isotherms are collected at the same time. The ensemble fluctuation method is essentially the equivalent way to determine the heat of adsorption directly from the differential change of internal energy of the entire cell in simulation[124,162],

$$q_d = H_b - \left(\frac{\partial U}{\partial N}\right)_{T,V} = H_b - \frac{f(U_N, N)}{f(\mathrm{N}, \mathrm{N})} \tag{105}$$

where fluctuation of X and Y is $f(\mathrm{X}, \mathrm{Y}) = \langle XY \rangle - \langle X \rangle \langle Y \rangle$.

The details of the derivation follows the statistical mechanic concept we have shown in previous section. The total internal energy includes the kinetic part U_k (ideal gas contribution) and the configurational part U_c:

$$U = U_k + U_c \tag{106}$$

The configuration part can be expressed as:

$$U_c = \frac{1}{\Xi} \sum_{N \geq 0} \int \cdots \int \frac{U_N \exp\left[-\beta\left(U_N - \mu N\right)\right]}{N! \Lambda^{3N}} d\mathbf{r}^{3N} \tag{107}$$

where U_N is the potential energy, and kinetic part is only related with temperature, so we have

$$\left[\frac{\partial U}{\partial \beta\mu}\right]_{T,V} = \left[\frac{\partial U_c}{\partial \beta\mu}\right]_{T,V} \tag{108}$$

$$\begin{aligned} \left[\frac{\partial U_c}{\partial(\beta\mu)}\right]_{T,V} &= \frac{1}{\mathrm{X}} \sum_{N \geq 0} \int \cdots \int \frac{U_N \mathrm{N} \exp\left[-\beta\left(U_N - \mu N\right)\right]}{N! \Lambda^{3N}} d\mathbf{r}^{3N} \\ &- \frac{1}{\mathrm{X}^2}\left(\frac{\partial \mathrm{X}}{\partial(\beta\mu)}\right) \sum_{N \geq 0} \int \cdots \int \frac{U_N \exp\left[-\beta\left(U_N - \mu N\right)\right]}{N! \Lambda^{3N}} d\mathbf{r}^{3N} \end{aligned} \tag{109}$$

After rearrangement of Eq.(109), it can be expressed as:

$$\left[\frac{\partial U_c}{\partial(\beta\mu)}\right]_{T,V} = \langle U_N \cdot N\rangle - \langle U_N\rangle\left(\frac{\partial \ln \Xi}{\partial(\beta\mu)}\right)_{T,V} = \langle U_N \cdot N\rangle - \langle U_N\rangle\langle N\rangle \quad (110)$$

And because the second order derivative of grand potential is actually the fluctuation of number of molecules inside the system, so we have

$$\left[\frac{\partial(\beta\mu)}{\partial N}\right]_{T,V} = \frac{1}{\left[\frac{\partial N}{\partial(\beta\mu)}\right]_{T,V}} = \frac{1}{\langle N^2\rangle - \langle N\rangle^2} \quad (111)$$

Then after decomposing the internal energy to two parts,

$$\left(\frac{\partial U}{\partial N}\right)_{T,\mathrm{V}} = \left(\frac{\partial U}{\partial \beta\mu}\right)_{T,V}\left(\frac{\partial \beta\mu}{\partial N}\right)_{T,V} \quad (112)$$

We can write the final form as

$$\left(\frac{\partial U}{\partial N}\right)_{T,V} = \frac{f(U_N, N)}{f(\mathrm{N}, \mathrm{N})} \quad (113)$$

5.3. Results and Discussions

In previous works[116,163], we have demonstrated that the classical DFT performs well for the adsorption isotherm over a broad range of pressure. In DFT calculations, we use the MBWR equation of state to relate the gas pressure and chemical potential in the bulk, and the modified fundamental measure theory to account for the repulsive interactions between gas molecules in formulating the excess Helmholtz energy functional. Among different versions of DFT methods, Weighted Density Approximation (WDA) version works generally better for gas adsorption in supercritical conditions, which are mostly interested in gas storage and separation. So in this work, we also used the WDA to account for the excess Helmholtz energy originated from intermolecular

attractions. The Lennard-Jones (LJ) potential is used for gas-gas interactions for all the calculations. All the LJ parameters used in this work are summarized in Table 1. The details for GCMC simulation and the slit pore model are the same as described in the supporting information of previous chapter.

We first calibrate the DFT predictions with results from standard GCMC simulations inside model slit pore system. While such calibration has been reported extensively for adsorption isotherms, we are unaware of previous applications of DFT for predicting isosteric heat for gas adsorption in supercritical region. Figure 2 shows, as an illustrative example, the differential heat of adsorption of a LJ fluid (Krypton) in a slit pore predicted from DFT in comparison to GCMC results at 298K in the entire pressure region. Here the reduced pore width is 1.5nm ($H/\sigma = 4$ for Kr), and we also include the results from the conventional Clapeyron equation Eq.(90). We can see that the Clapeyron equation only works for ideal gas region where the pressure is low and intermolecular interactions are negligible between gas molecules as we explained rigorously in previous section. It overestimated the heat from the intermediate pressure region even for the model slit pore system with simple geometry. While DFT predicts the differential heat of adsorption consistently with ensemble fluctuation method from GCMC in the entire pressure range as shown on both panels of Figure 2.

Next, we consider several examples for heat effect in there dimensional nanoporous materials. Here we show Ar and CH_4 adsorption in silica zeolite with mordenite framework inverted (MFI) structure [121] and CH_4 adsorption in metal organic framework CuBTC[40]. The structures of the materials considered in this work are all rigid

and from experimentally determined Crystalline Information File (CIF). For silicate MFI, we applied the zeolite force field widely used in the computational works, which has been calibrated with gas adsorption isotherm especially for zeolites[161], and for CuBTC, we applied the generic force field UFF[38]. Differential heat of adsorption calculated from DFT with Eq.(99) is compared with both GCMC ensemble fluctuation method and the available calorimetry data as shown in Figure 3,4 and 5, which are all in the low pressure region (around 1 bar). Considering the experimental uncertainty ±1.1 kj/mol as explained in the experimental paper for calorimetry measurement[145,158,159], both the theoretical results agree quite well with calorimetry data, which further validate our thermodynamic procedure. Besides that, it indicates that successful application of both empirical force field used in the computational work since in the low pressure region, the adsorbate-adsorbate interactions are negligible and adsorbent-adsorbate interaction dominates as we shown in deriving Eq.(92). For all the three cases shown here, we can see that in the low pressure limit, due to negligible adsorbate-adsorbate interaction and the structural symmetry for all crystalline materials, the most favorable adsorption sites are actually equivalent for gas molecules to bind, so the initial differential heat is almost constant with increasing pressure in this region. This effect is even more obvious for smaller and relatively weaker gas molecules like Ar as shown in Figure 3.

In Figure 6, we also show the differential heat calculated in the non-ideal gas region for CH_4 adsorption in CuBTC as an example. The DFT results calculated by numerical evaluation of the differentiation of equilibrium grand potential at different temperature agrees well with GCMC simulation in the entire pressure region considered.

We can see that when pressure further increase from the ideal gas region, the differential heat of adsorption will decrease, which means that after all the favorable adsorption sites are occupied, the adsorbate-adsorbent interaction will decrease and while the adsorbate-adsorbate interaction increases. It worth noting that by applying the classical density functional theory, the equilibrium grand potential is obtained during the isotherm prediction without any extra computational cost, so the prediction of differential heat of adsorption is much more efficient compared with conventional Monte Carlo simulation as we indicated in previous publications for material screening with classical DFT[116,163].

5.4. Conclusions

In this work, we formulate a theoretical procedure for analyzing the isosteric heat and calculate the differential heat of adsorption with the grand potential of the inhomogeneous system obtained at different thermal conditions by applying the classical density functional theory. Compared with the differential heat calculated from the ensemble fluctuation method with GCMC, the heat of adsorption can be predicted in a both efficient and accurate manner. In addition, we have shown that the Clausius-Clapeyron equation is valid only in the ideal gas limit. By analyzing gas adsorption and heat effect in both low pressure limit and non-ideal gas region, we demonstrate that the classical DFT represents a powerful tool for studying gas adsorption. The new thermodynamic framework is able to predict the isotherm and isosteric heat self-consistently.

Figure 5-1. Schematic set up for gas adsorption isotherm and heat measurement in the calorimter cell.

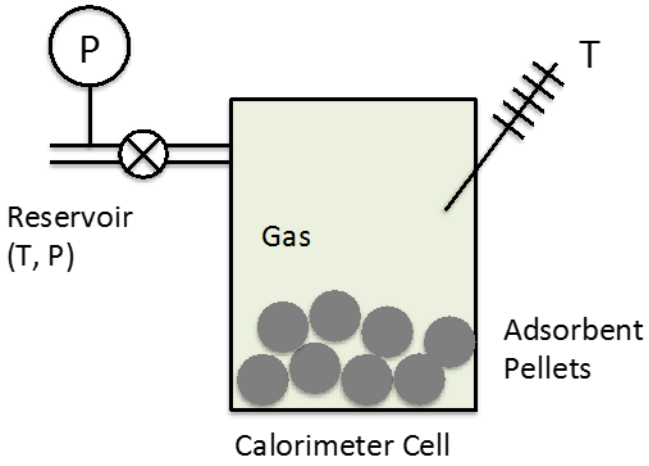

Figure 5-2. Isosteric heat for Kr adsorption by a slit pore at 298 K in the Henry's law region (A) and non-ideal region (B). In both cases, the pore width is 1.5 nm, and the reduced surface energy is $\varepsilon_{sf}^{*} \equiv \varepsilon_{sf} / \varepsilon_{ff}$ =0.55, where ε_{ff} stands for the LJ energy parameter for Kr. The solid and dashed lines represent the isosteric heat from Eq.(99) and Eq.(90), respectively. Black squares are calculated from the ensemble fluctuation method using GCMC simulation, and the error bars are within the square.

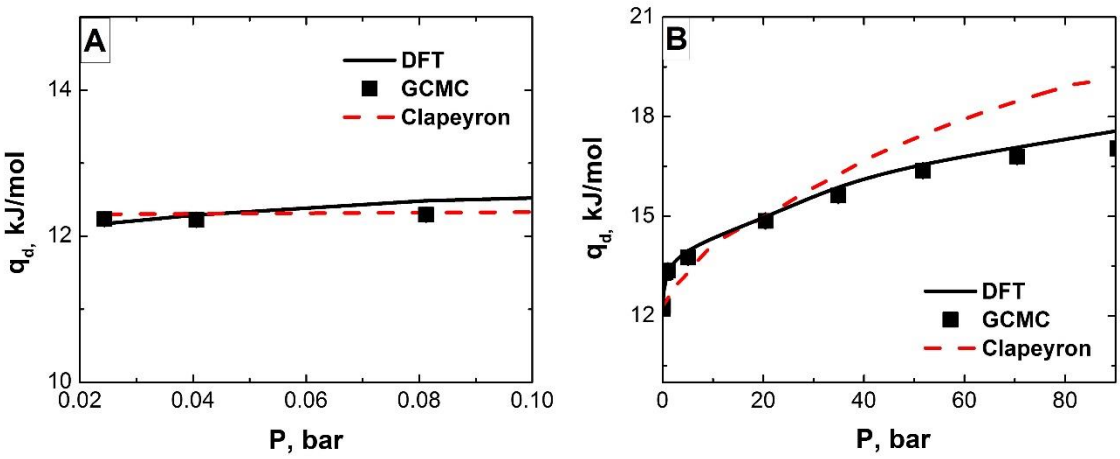

Figure 5-3. Adsorption isotherm (A) and corresponding differential heat of adsorption (B) for Ar in silicate MFI at 306 K. As shown in Figure 5-2, the solid lines are from DFT calculations, the open spuares are from Monte Carlo simulation, and the black solid circles represent the experimetal results from reference[158].

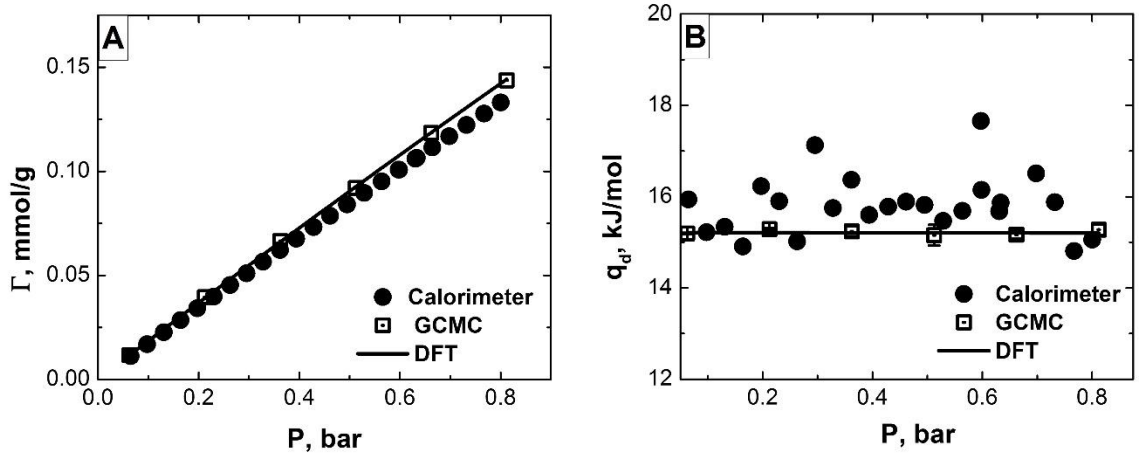

Figure 5-4. Adsorption isotherm (A) and corresponding differential heat of adsorption (B) for CH_4 adsorption in silicate MFI at 296 K. Lines and symbols follow the same meanings as those in Figure 5-3. The experimetal results are from reference[145].

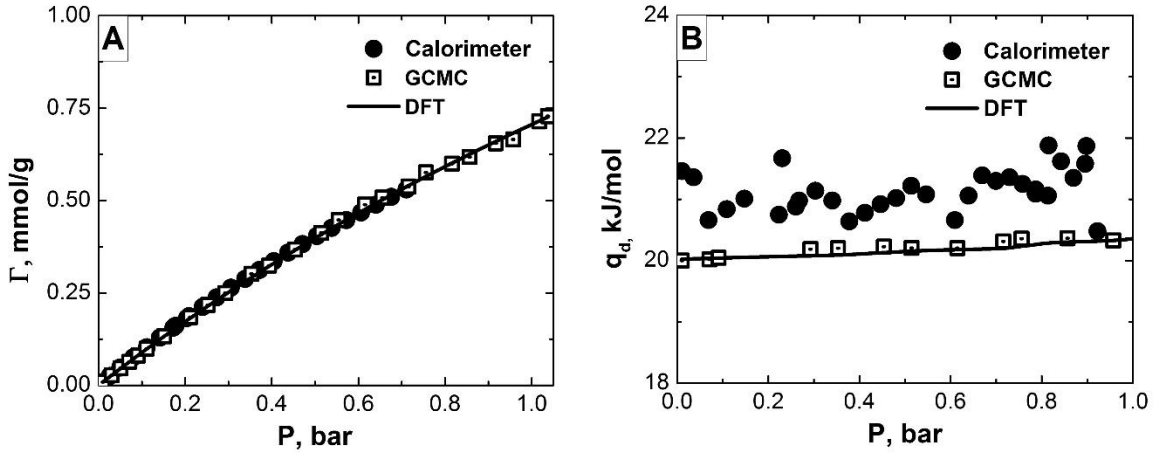

Figure 5-5. Adsorption isotherm (A) and corresponding differential heat of adsorption (B) for CH_4 adsorption in silicate CuBTC at 298 K. Lines and symbols follow the same meanings as those in Figure 5-3 and 5-4. The experimetal results from reference[164].

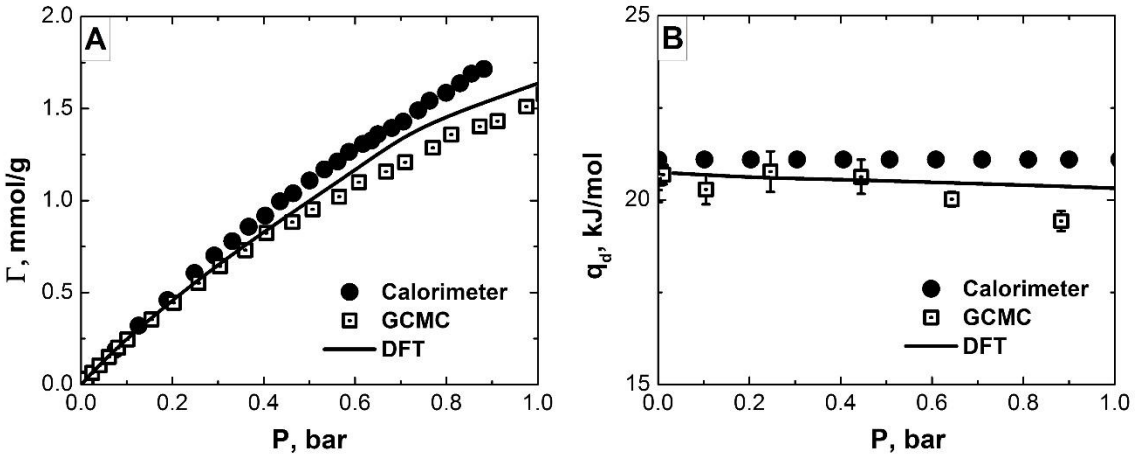

Figure 5-6. Adsorption isotherm (A) and corresponding differential heat of adsorpt (B) for CH_4 adsorption in silicate CuBTC at 298 K. Lines and symbols follow the same meanings as those in Figure 5-3 and 5-4. The experimetal results are from reference[164].

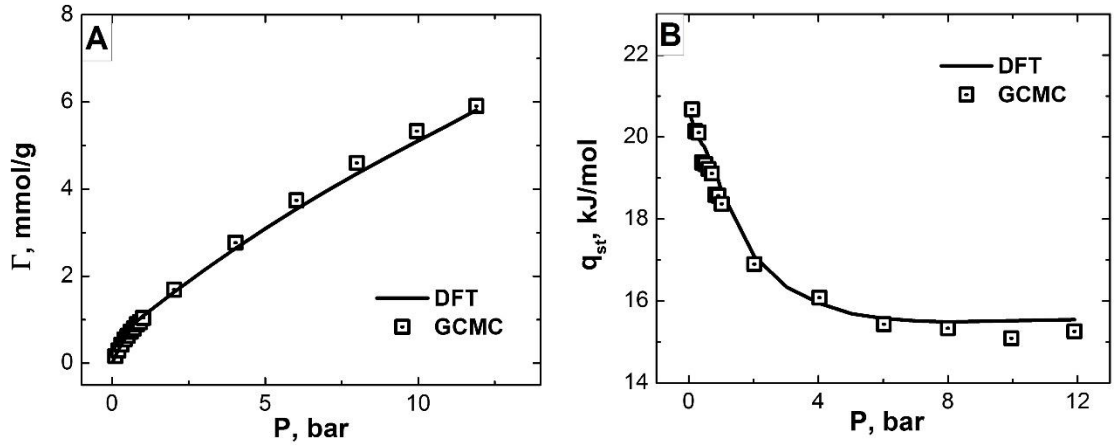

Table 5-1. Size and energy parameters for Kr, Ar, CH_4 gases and for the Steele wall.

Gas	**σ_{ff} , Å**	**ε_{ff}/k_B, K**
Kr	3.636	166.4
Ar	3.405	119.8
CH_4	3.73	148
Steele Wall	**σ_{ss} , Å**	**ε_{ss}/k_B, K**
	3.4	28

References

1. Myers AL. Thermodynamics of adsorption in porous materials. *AIChE Journal.* 2002;48(1):145-160.

2. Bhatia SK, Myers AL. Optimum Conditions for Adsorptive Storage. *Langmuir.* 2006/02/01 2006;22(4):1688-1700.

3. Lee S-J, Bae Y-S. Can Metal–Organic Frameworks Attain New DOE Targets for On-Board Methane Storage by Increasing Methane Heat of Adsorption? *The Journal of Physical Chemistry C.* 2014/08/28 2014;118(34):19833-19841.

4. Amrouche H, Creton B, Siperstein F, Nieto-Draghi C. Prediction of thermodynamic properties of adsorbed gases in zeolitic imidazolate frameworks. *RSC Advances.* 2012;2(14):6028-6035.

5. Sircar S. Basic Research Needs for Design of Adsorptive Gas Separation Processes. *Industrial & Engineering Chemistry Research.* 2006/08/01 2006;45(16):5435-5448.

6. Hartzog DG, Sircar S. Sensitivity of PSA process performance to input variables. *Adsorption.*1(2):133-151.

7. Mason JA, Veenstra M, Long JR. Evaluating metal-organic frameworks for natural gas storage. *Chemical Science.* 2014;5(1):32-51.

8. Nicholson DP, N, G. *Computer Simulation and the Statistical Mechanics of Adsorption*. London: Academic Press; 1982.

9. Vuong T, Monson PA. Monte Carlo Simulation Studies of Heats of Adsorption in Heterogeneous Solids. *Langmuir.* 1996/01/01 1996;12(22):5425-5432.

10. He Y, Seaton NA. Monte Carlo Simulation and Pore-Size Distribution Analysis of the Isosteric Heat of Adsorption of Methane in Activated Carbon. *Langmuir.* 2005/08/01 2005;21(18):8297-8301.

11. Fu J, Tian Y, Wu J. Classical density functional theory for methane adsorption in metal-organic framework materials. *AIChE Journal.* 2015;61(9):3012-3021.

12. Fu J, Liu Y, Tian Y, Wu J. Density Functional Methods for Fast Screening of Metal–Organic Frameworks for Hydrogen Storage. *The Journal of Physical Chemistry C.* 2015/03/12 2015;119(10):5374-5385.

13. Baerlocher CM, L. B. Database of Zeolite Structures. 2001; http://www.iza-structure.org/databases/.

14. Chui SS-Y, Lo SM-F, Charmant JPH, Orpen AG, Williams ID. A Chemically Functionalizable Nanoporous Material [Cu₃(TMA)₂(H₂O)₃]_n. *Science.* 1999;283(5405):1148-1150.

15. Liu B, Smit B. Comparative Molecular Simulation Study of CO2/N2 and CH4/N2 Separation in Zeolites and Metal−Organic Frameworks. *Langmuir.* 2009/05/19 2009;25(10):5918-5926.

16. Rappe AK, Casewit CJ, Colwell KS, Goddard WA, Skiff WM. UFF, a full periodic table force field for molecular mechanics and molecular dynamics simulations. *Journal of the American Chemical Society.* 1992/12/01 1992;114(25):10024-10035.

17. Dunne JA, Rao M, Sircar S, Gorte RJ, Myers AL. Calorimetric Heats of Adsorption and Adsorption Isotherms. 2. O2, N2, Ar, CO2, CH4, C2H6, and SF6 on NaX, H-ZSM-5, and Na-ZSM-5 Zeolites. *Langmuir.* 1996/01/01 1996;12(24):5896-5904.

18. Dunne JA, Mariwala R, Rao M, Sircar S, Gorte RJ, Myers AL. Calorimetric Heats of Adsorption and Adsorption Isotherms. 1. O2, N2, Ar, CO2, CH4, C2H6, and SF6 on Silicalite. *Langmuir.* 1996/01/01 1996;12(24):5888-5895.

19. Hulvey Z, Lawler KV, Qiao Z, et al. Noble Gas Adsorption in Copper Trimesate, HKUST-1: An Experimental and Computational Study. *The Journal of Physical Chemistry C.* 2013/10/03 2013;117(39):20116-20126.

20. Wu D, Guo X, Sun H, Navrotsky A. Thermodynamics of Methane Adsorption on Copper HKUST-1 at Low Pressure. *The Journal of Physical Chemistry Letters.* 2015/07/02 2015;6(13):2439-2443.

Chapter 6. Modeling Gas Diffusivity in Porous Materials: Transition-State Theory, String Method, and Excess Entropy Scaling

Abstract

We provide an efficient computational procedure for rapid and more accurate prediction of the self-diffusivity of gas molecules in nanoporous materials by integrating the string method and the transitional-state theory (TST) for inter-cage hopping at low pressure and the excess entropy scaling law for gas diffusion at high pressure. The theoretical predictions have been calibrated with results from molecular dynamics (MD) simulations for the diffusion coefficients of methane and hydrogen gases in several representative metal organic framework (MOF) materials with a rigid pore configuration. Combined with the classical density functional theory (DFT) for predicting the excess entropy, the new theoretical procedure enables a rapid prediction of adsorption isotherms, isosteric heat and transport coefficients important for the computational design and screening of nanostructured materials for gas storage and separation

6.1. Introduction

Molecular transport in nanoporous materials plays a crucial role in emerging nanotechnologies for gas storage and separation[1-3]. While the literature is vast for diffusion in porous materials, direct measurement of gas diffusion in nanopores was possible only during the past few decades[4]. Although practical applications are often concerned with the phenomenological transport or the Fickian diffusion coefficient, the self-diffusivity of gas molecules in nanoporous materials has been widely studied from both experimental and theoretical means[2,5,6]. Because self-diffusivity is closely connected with the transport diffusion coefficients and can be directly measured from PFG-NMR experiment[7,8], it provides a useful benchmark for calibration of theoretical developments to study various transport processes[3,9-11].

Theoretical predictions of self-diffusivity are mostly based on molecular dynamics (MD) simulations. The self-diffusion coefficients can be obtained by analyzing the trajectories of gas molecules according to Einstein's equation[12,13]. While the computational procedure is rather straightforward, one of the major difficulties with standard MD simulations is that the gas diffusion coefficient in nanoporous materials is extremely small ($\sim 10^{-12} m^2 / s$), which is often beyond the time scale accessible to typical simulations[14,15]. Among various indict methods, the transitional-state theory (TST) is often used to predict the kinetic coefficients of infrequent events such as gas hopping among various cages of nanoporous materials[15-19]. In principle, TST is able to account for the flexibility of both the pore structure and gas molecules. Whereas in general such flexibility may play a major role

in dynamic processes[20], it has been shown that its influence is relatively insignificant on the diffusivity of small gas molecules in nanostructured materials[14].

In this work, we use a simplified version of TST to predict the self-diffusivity of small gas molecules (such as H_2 and CH_4) in the nanoporous materials at infinite dilution. The dynamic correction[18,21] is not included in our calculations because we are mainly concerned with hydrogen and methane storage and separation. To estimate the diffusion barrier[7], we need to define a diffusion pathway that connects different low energy states. Conventional methods are extremely time consuming, especially when the materials involves multiple pores with three-dimensional complexity. Because the diffusion pathway is defined around the saddle point of the potential energy surface, such difficulty can be greatly alleviated with the aid of the string method[22]. We have tested the new procedure for H_2 and CH_4 diffusion in several metal organic framework (MOF) materials. The string method defines the diffusion pathway along the energy gradient. By contrast, a conventional method is based on the grid searching and the cluster analysis[18,21]. At conditions beyond the infinite dilution limit, we can calculate the self-diffusivity using the excess entropy scaling method[10]. Toward that end, we combine the diffusivity result from TST prediction and the excess entropy predicted by the classical density functional theory (DFT). We demonstrate that the new procedure for self-diffusivity calculation can improve the computational efficiency by at least one order of magnitude.

6.2. Theoretical Methods

String Method

In this work, TST is applied only to diffusion of a spherical gas molecule in a rigid porous material at the infinite dilution. As a result, the free energy landscape reduces to the potential energy, which corresponds to the external energy for the gas molecule due to interacting with the framework,

$$V^{\text{ext}}(\mathbf{r}) = \sum_{i \in \text{MOF}} u_{if}(\mathbf{r} - \mathbf{r}_i) \tag{114}$$

For convenience, the external energy is mapped into the 3-D space by considering only the Lennard-Jones (LJ) interactions:

$$u_{ij}(r) = 4\varepsilon_{ij}\left[\left(\frac{\sigma_{ij}}{r}\right)^{12} - \left(\frac{\sigma_{ij}}{r}\right)^{6}\right] \tag{115}$$

For all MOF materials considered in this work, the framework structures are from experimental Crystal Information Files (CIFs)[23,24] and assumed to be rigid. The UFF force field is used for all framework atoms[25], and the LJ parameters are the same as those used in our previous publications[26,27].

To implement the string method, we define a minimum energy pathway, $p(s)$, ($0 \le s \le 1$) (where s is the normalized reaction coordinate on the path), to connect the initial state and the final state that are identified from the minimum external potential energy.. The diffusion path is generally defined along one axis that passes through the transition state. The saddle point on the energy surface corresponds to the void center

linking neighboring cages (i.e., initial and final states). The diffusion path is defined such that the tangent τ along the path is parallel to the energy gradient,

$$\nabla V^{ext} - (\tau \cdot \nabla V^{ext})\ \tau = 0 \tag{116}$$

where

$$\tau(\mathbf{r}) = \frac{dp(s)}{ds} \Big/ \left(\frac{dp(s)}{ds} * \frac{dp(s)}{ds} \right)^{1/2} \tag{117}$$

is the normalized tangent along the path and * donates the inner product defined as $f * g = \int f(\mathbf{r})\, g(\mathbf{r})\, d\mathbf{r}$. The above equation is then solved by a modified steepest descent algorithm,

$$\frac{d\mathbf{r}}{dt} = -\left[\nabla V - (\tau \cdot \nabla V)\tau \right] + k\tau \tag{118}$$

where k is the Lagrange multipliers, and t is a fictitious time for evolving the equations on the energy landscape.

Transitional-state Theory

We use a simplified version of TST method to estimate the self-diffusivity at infinite dilution condition[18]:

$$D_s = \frac{1}{2} k \lambda^2 \tag{119}$$

where λ is the length of the corresponding diffusion pathway, and k is hopping rate over the rate-limiting barrier ΔE as indicated in Fig.1b) with red arrows:

$$k = \nu \exp(-\Delta \mathrm{E}/\ \mathrm{RT}) \tag{120}$$

where v is the pre-exponential factor which is assumed to be 10^{12} for MOFs. The simplified TST method is justified because, for most cases, the rate-limiting energy barrier is sufficiently high compared with other barriers in the diffusion pathway.

The rate-limiting barrier is not always straightforward to identify for materials with arbitrary pore structures (as shown in Fig.2b). In this case, we need to apply the more general TST method and calculate the self-diffusivity with the following equation[7,28,29] for the hopping rate:

$$k = \sqrt{\frac{k_B T}{2\pi m}} \frac{\exp\left[-\mathrm{V}^{ext}\left(x_{sd}\right)/\mathrm{RT}\right]}{\int_x \exp\left[-\mathrm{V}^{ext}\left(x_{sd}\right)/\mathrm{RT}\right] dx} \tag{121}$$

where the integral is performed through the two energy minimum states, and x_{sd} is the saddle point.

Excess Entropy Scaling Method

As discussed in Chapter 2, the equilibrium density profile $\rho(\mathbf{r})$ can be calculated from the classical DFT calculations. From the density profile, we can calculate the adsorption amount based on the number of gas molecules in the MOF material and the system volume:

$$\Gamma = \frac{k_B T_0}{P_0 V} \int \rho(\mathbf{r}) \mathrm{d}\mathbf{r} \tag{122}$$

where $P_0 = 1\,\mathrm{atm}$ and $T_0 = 25\,^{\circ}\mathrm{C}$ stand for the standard state (STP). As usual, the adsorption amount is expressed as the volume of gas adsorbed at the standard-state condition in unit volume of material.

Given the equilibrium density profile, we can also calculate the excess entropy from thermodynamic relation:

$$S^{ex} = -\left(\frac{dF^{ex}}{dT}\right)_{r(\mathbf{r})} \tag{123}$$

The self-diffusivity is obtained by a combination of the excess entropy scaling rule:

$$\ln D_S = \left(1 - \frac{\lambda}{v_{free}}\right)\ln D_0 + \frac{\lambda}{v_{free}}\ln D_E \tag{124}$$

where λ is the weighting factor to determine the contribution of gas-surface interaction and gas-gas interaction, v_{free} is the fraction of free volume that are accessible to gas molecules, D_0 is the diffusivity at infinite dilution limit, which can be obtained either from MD simulation as previously published in our group[10] or from TST as in this work, and D_E is the contribution from gas-gas interactions as discussed in Chapter 2.

6.3. Results and Discussions

Figure 1a) shows the diffusion pathway for H_2 in MOF-5 at 298K. Because of the small size H_2 gas molecule, the pathway is not complicated and the resulting diffusion barrier is relatively low. As shown in Figure 1b), the energy parallel is about 3.5 kJ/mol. While for a larger gas molecule such as CH_4 diffusion in the same material, Figure 2a) indicates that the diffusion pathway is quite complicated with zigzag type of curves due to the higher confinement with respect to the larger molecule. As a result, the energy barriers shown on Figure 2b) are much higher than those in 2a). For this case, we cannot simply

determine the rate-limiting barrier. To apply Eq.(120) for calculating the hopping rate, we need to calculate the overall diffusion barrier using Eq.(121).

Figure 3 summarize all the results from this work combing TST with the string method to calculate the self-diffusivity of either CH_4 or H_2 in several MOF materials. We can see excellent agreement of the theoretical results with MD simulation data[10,29]. By contrast, previous application of TST compares poorly with the simulation results.

Finally, in Figures 4 and 5, we compare the self-diffusivity of both gases for the entire pressure range predicted with the new procedure introduced in this work with pure MD simulation and with a previous method by combining MD with entropy scaling from DFT[10]. We can see that the new results are all within the error bar of simulation, and consistent with previous calculations for the entire pressure range. The computational time required for TST combined with string method to generate the diffusivity at infinite dilution limit is within 10 mins, while the MD simulation requires more than an hour. By replacing MD data at infinite dilution with TST method for D_k, we can further improve the calculation efficiency of self-diffusivity by applying Eq.(124).

6.4. Conclusions

The string method allows us to directly calculate the diffusion pathway along the energy gradient, which is proved to be both efficient and accurate for determining the minimum energy pathway and the corresponding energy barrier. We have shown the great potential of string method in combination with TST to calculate self-diffusivity, which overcomes one of the major drawbacks with the conventional implement of TST method. Due to the huge number of existing structures of nanoporous materials and the underlying

potential for their versatile applications in gas storage and separation, it is urgent to develop efficient computation methods to predict and compare the diffusive and separating properties of different porous materials. Toward that end, the theoretical procedures introduced in this work will help identify the best performing materials and their structure-properties relationships to guide rational design and synthesis of novel materials.

Figure 6-1. a) Diffusion pathway of H_2 in MOF-5 at 298K; b) The corresponding diffusion energy barrier predicted by string method as indicated with the red arrow. The black stars represent the atoms belonging to the framework, and the blue line is the calculated diffusion pathway.

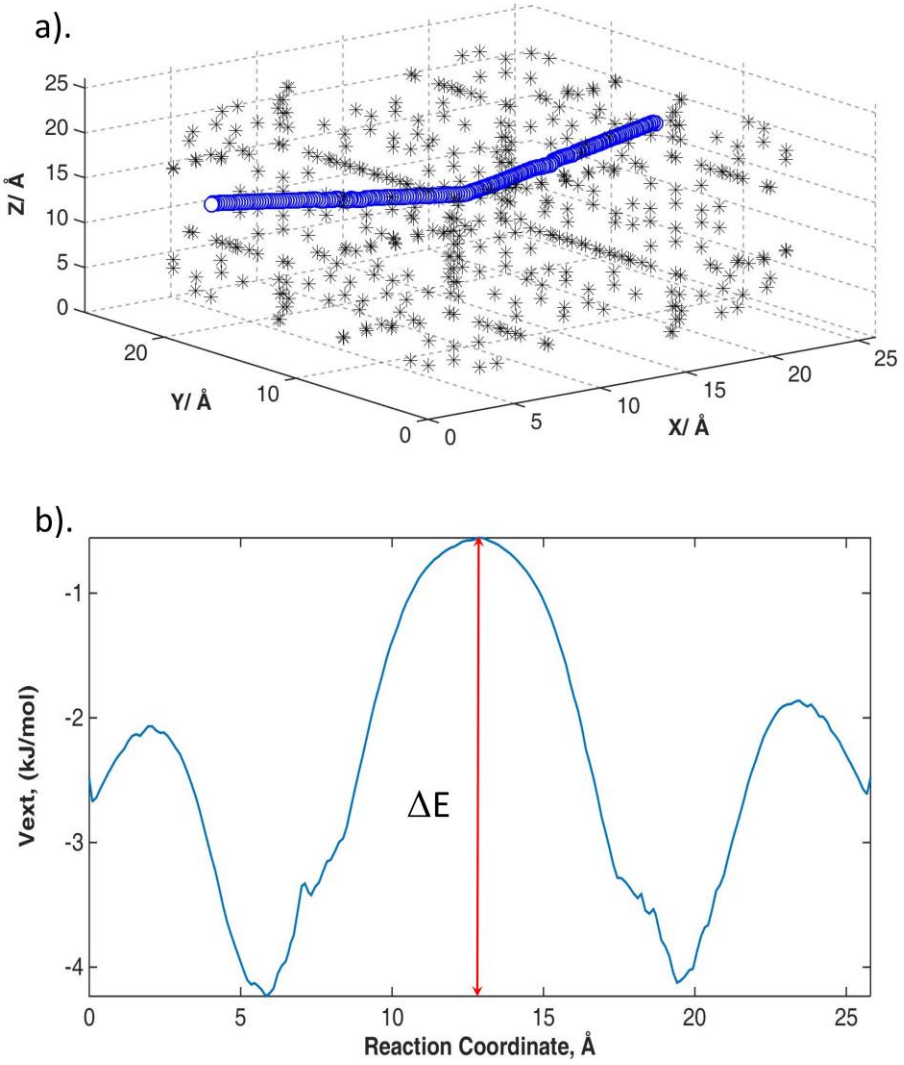

Figure 6-2. a) Diffusion pathway of CH_4 in MOF-5 at 298K; b) The corresponding diffusion energy barrier predicted by string method. The black stars represent the atoms belonging to the framework, and the blue line is the calculated diffusion pathway.

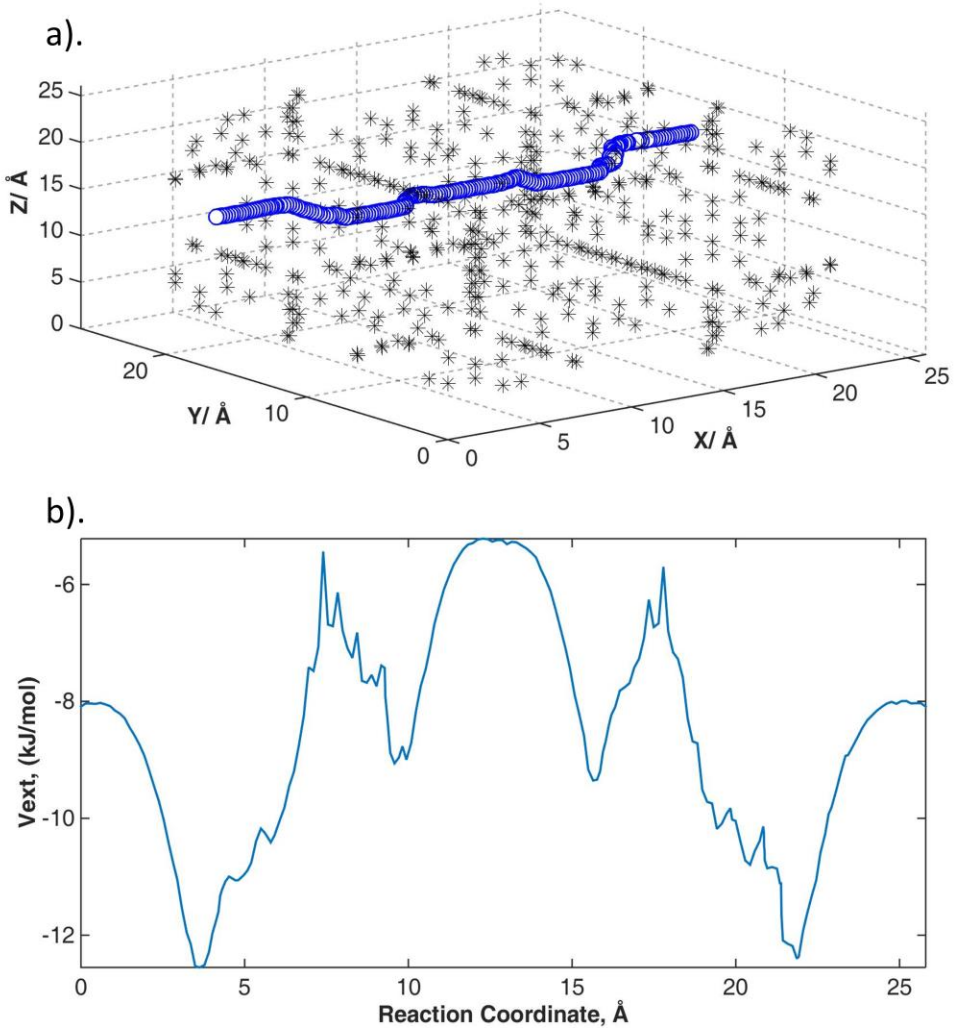

Figure 6-3. The overall comparison of TST predicted self-diffusivities of CH_4 and H_2 diffusion in CuBTC and four IRMOFs with MD results[27,165]. Black squares are results from this work, and the red circles are from previous calculations from reference[166]. The gas molecule is H_2 without specific label.

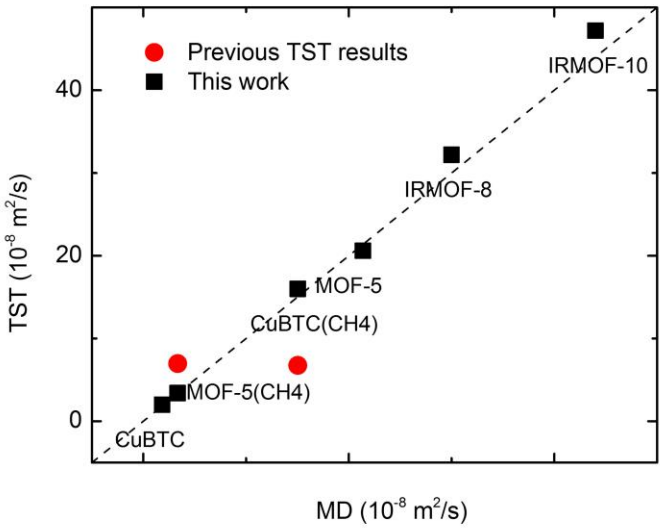

Figure 6-4. Comparison of the calculted self-diffusivity of CH_4 in MOF-5 from the new procedure with MD simulation and previous method by combining MD with entropy scaling from DFT[27].

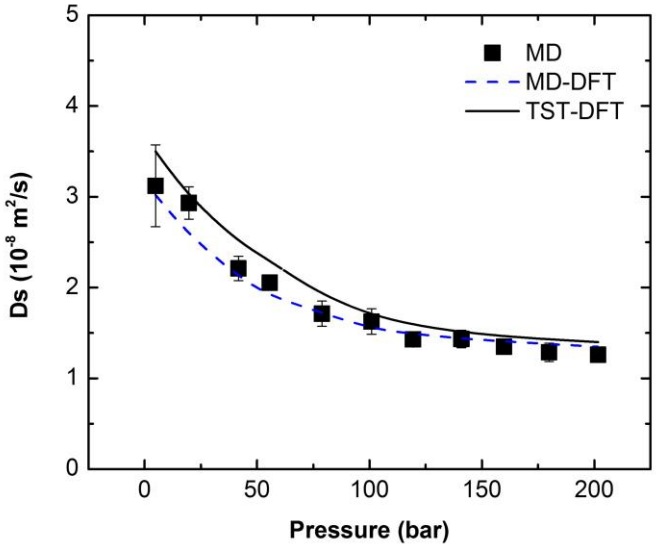

Figure 6-5. Comparison of the calculted self-diffusivity of H_2 in MOF-5 from the new procedure with MD simulation and previous method by combining MD with entropy scaling from DFT[27].

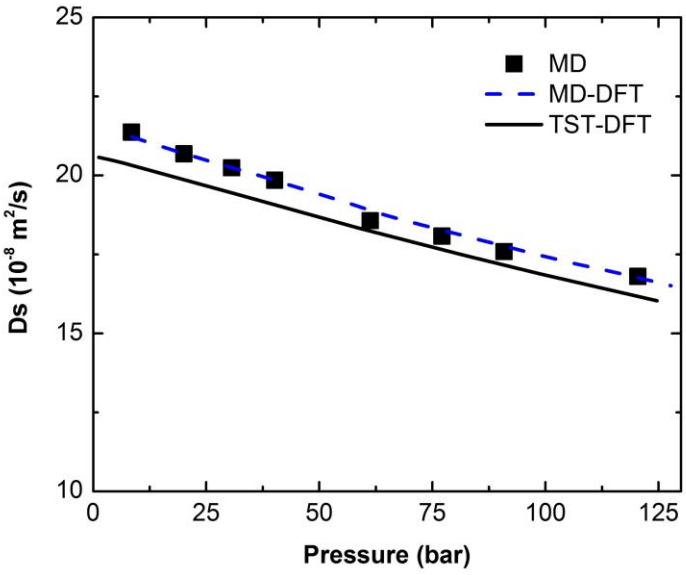

References

1. Bhatia SK, Bonilla MR, Nicholson D. Molecular transport in nanopores: a theoretical perspective. *Physical Chemistry Chemical Physics.* 2011;13(34):15350-15383.

2. Krishna R. Diffusion in porous crystalline materials. *Chemical Society Reviews.* 2012;41(8):3099-3118.

3. Krishna R. Describing the Diffusion of Guest Molecules Inside Porous Structures. *The Journal of Physical Chemistry C.* 2009/11/19 2009;113(46):19756-19781.

4. Karger J, Ruthven DM. Diffusion in nanoporous materials: fundamental principles, insights and challenges. *New Journal of Chemistry.* 2016;40(5):4027-4048.

5. Keskin S, Liu J, Johnson JK, Sholl DS. Atomically detailed models of gas mixture diffusion through CuBTC membranes. *Microporous and Mesoporous Materials.* 2009;125(1–2):101-106.

6. Chmelik C, Kärger J. The predictive power of classical transition state theory revealed in diffusion studies with MOF ZIF-8. *Microporous and Mesoporous Materials.* 2016;225:128-132.

7. Smit B, Maesen TLM. Molecular Simulations of Zeolites: Adsorption, Diffusion, and Shape Selectivity. *Chemical Reviews.* 2008/10/08 2008;108(10):4125-4184.

8. Kärger J, Ruthven DM, Theodorou DN. Diffusion Measurement by Monitoring Molecular Displacement. *Diffusion in Nanoporous Materials*: Wiley-VCH Verlag GmbH & Co. KGaA; 2012:347-394.

9. Watanabe T, Keskin S, Nair S, Sholl DS. Computational identification of a metal organic framework for high selectivity membrane-based CO2/CH4 separations: Cu(hfipbb)(H2hfipbb)0.5. *Physical Chemistry Chemical Physics.* 2009;11(48):11389-11394.

10. Liu Y, Fu J, Wu J. Excess-Entropy Scaling for Gas Diffusivity in Nanoporous Materials. *Langmuir.* 2013/10/22 2013;29(42):12997-13002.

11. Vaz RV, Magalhães AL, Fernandes DLA, Silva CM. Universal correlation of self-diffusion coefficients of model and real fluids based on residual entropy scaling law. *Chemical Engineering Science.* 2012;79:153-162.

12. Kärger J, Ruthven DM, Theodorou DN. Molecular Dynamics Simulations. *Diffusion in Nanoporous Materials*: Wiley-VCH Verlag GmbH & Co. KGaA; 2012:227-273.

13. Skoulidas AI, Sholl DS. Molecular Dynamics Simulations of Self-Diffusivities, Corrected Diffusivities, and Transport Diffusivities of Light Gases in Four Silica Zeolites To Assess Influences of Pore Shape and Connectivity. *The Journal of Physical Chemistry A.* 2003/11/01 2003;107(47):10132-10141.

14. June RL, Bell AT, Theodorou DN. Transition-state studies of xenon and sulfur hexafluoride diffusion in silicalite. *The Journal of Physical Chemistry.* 1991/10/01 1991;95(22):8866-8878.

15. Dubbeldam D, Beerdsen E, Vlugt TJH, Smit B. Molecular simulation of loading-dependent diffusion in nanoporous materials using extended dynamically corrected transition state theory. *The Journal of Chemical Physics.* 2005;122(22):224712.

16. Auerbach SM. Theory and simulation of jump dynamics, diffusion and phase equilibrium in nanopores. *International Reviews in Physical Chemistry.* 2000/04/01 2000;19(2):155-198.

17. Beerdsen E, Dubbeldam D, Smit B. Molecular Understanding of Diffusion in Confinement. *Physical Review Letters.* 2005;95(16):164505.

18. Haldoupis E, Nair S, Sholl DS. Efficient Calculation of Diffusion Limitations in Metal Organic Framework Materials: A Tool for Identifying Materials for Kinetic Separations. *Journal of the American Chemical Society.* 2010/06/02 2010;132(21):7528-7539.

19. Kärger J, Ruthven DM, Theodorou DN. Infrequent Event Techniques for Simulating Diffusion in Microporous Solids. *Diffusion in Nanoporous Materials*: Wiley-VCH Verlag GmbH & Co. KGaA; 2012:275-301.

20. Kolokathis PD, Káli G, Jobic H, Theodorou DN. Diffusion of Aromatics in Silicalite-1: Experimental and Theoretical Evidence of Entropic Barriers. *The Journal of Physical Chemistry C.* 2016/09/29 2016;120(38):21410-21426.

21. Haldoupis E, Nair S, Sholl DS. Pore size analysis of >250 000 hypothetical zeolites. *Physical Chemistry Chemical Physics.* 2011;13(11):5053-5060.

22. Nucleation in Polymers and Soft Matter. *Annual Review of Physical Chemistry.* 2014;65(1):449-475.

23. Chui SS-Y, Lo SM-F, Charmant JPH, Orpen AG, Williams ID. A Chemically Functionalizable Nanoporous Material [Cu₃(TMA)₂(H₂O)₃]_n. *Science.* 1999;283(5405):1148-1150.

24. Eddaoudi M, Kim J, Rosi N, et al. Systematic Design of Pore Size and Functionality in Isoreticular MOFs and Their Application in Methane Storage. *Science.* 2002;295(5554):469-472.

25. Rappe AK, Casewit CJ, Colwell KS, Goddard WA, Skiff WM. UFF, a full periodic table force field for molecular mechanics and molecular dynamics simulations. *Journal of the American Chemical Society.* 1992/12/01 1992;114(25):10024-10035.

26. Fu J, Tian Y, Wu J. Classical density functional theory for methane adsorption in metal-organic framework materials. *AIChE Journal.* 2015;61(9):3012-3021.

27. Fu J, Liu Y, Tian Y, Wu J. Density Functional Methods for Fast Screening of Metal–Organic Frameworks for Hydrogen Storage. *The Journal of Physical Chemistry C.* 2015/03/12 2015;119(10):5374-5385.

28. Camp JS, Sholl DS. Transition State Theory Methods To Measure Diffusion in Flexible Nanoporous Materials: Application to a Porous Organic Cage Crystal. *The Journal of Physical Chemistry C.* 2016/01/21 2016;120(2):1110-1120.

29. Liu B, Yang Q, Xue C, Zhong C, Smit B. Molecular simulation of hydrogen diffusion in interpenetrated metal-organic frameworks. *Physical Chemistry Chemical Physics.* 2008;10(22):3244-3249.

Chapter 7. Conclusions

In this thesis, we have calibrated four versions of classical DFT methods for high-throughput screening of MOFs for gas storage. The theoretical predictions are validated with extensive simulation data for both total gas uptake and the delivery capacity. Best materials for methane storage and best version of DFT method for material screening have been identified. The high computational efficiency renders classical DFT a suitable choice for high-throughput calculations.

Chapter 3 is denoted to clarifying controversial issues regarding the heat effect. We have shown that the differential heat of adsorption, which is fully consistent with directly measured heat from experimental calorimetry, can be derived rigorously only from the entire cell analysis by considering the total gas amount. In addition, we found that the isosteric heat of adsorption depends on system size and composition.

Chapter 4 intends to resolve the debate on whether BET surface area is consistent with geometrical surface area for different classes of porous materials. We have shown that the BET area is not necessarily correlated with geometrical surface area by performing standard BET method a large library of 1200 MOFs with diverse structures and interactions with gas molecules.

Chapter 5 is dedicated to the development of more computational efficient procedure to calculate gas self-diffusivity in nanoporous materials. An efficient calculation of transport properties is crucial for future work related with gas separation. We have demonstrated that, by combining the string method, the classical transitional-state Theory, and the excess entropy scaling method, and the classical DFT calculations, the new

procedure is extremely computationally efficient without losing accuracy compared with standard molecular dynamic simulations.

This dissertation work helps establish quantitative relationships between the material building blocks and the thermophysical properties of confined fluids. The theoretical developments will speed up the widespread use of computational methods for high-throughput discovery and better utilization of nanoporous materials.